Non-linear electromagnetic imaging : from sparsity-preserving wavelet-based algorithms to deep learning

Yarui Zhang

université PARIS-SACLAY

Non-linear electromagnetic imaging: from sparsity-preserving wavelet-based algorithms to deep learning

Imagerie électromagnétique non linéaire : d'algorithmes basés sur les ondelettes préservant la parcimonie à l'apprentissage en profondeur

Thèse de doctorat de l'université Paris-Saclay

École doctorale n°575 Electrical, Optical, Bio-Physics and Engineering (EOBE)
Spécialité de doctorat : Génie électrique
Graduate School : Sciences de l'ingénierie et des systèmes
Référent : CentraleSupélec

Thèse préparée dans les unités de recherche Laboratoire de Génie Électrique et Électronique de Paris (Université Paris-Saclay, CentraleSupélec, CNRS) et Laboratoire des Signaux et Systèmes (Université Paris-Saclay, CNRS, CentraleSupélec) sous la direction de **Marc LAMBERT**, Chargé de recherche CNRS, le co-encadrement d'**Aurélia FRAYSSE**, Maîtresse de conférences Université Paris Saclay et de **Dominique LESSELIER**, Directeur de recherche CNRS émérite

Thèse soutenue à Paris-Saclay, le 15 décembre 2022, par

Yarui ZHANG

Composition du jury

Membres du jury avec voix délibérative

Laetitia Thirion-Lefevre Professeure, CentraleSupélec	Présidente
Alexandre Baussard Professeur, Université de Technologie de Troyes	Rapporteur & Examinateur
Amélie Litman Professeure, Aix-Marseille Université	Rapporteure & Examinatrice
Sébastien Bourguignon Maître de Conférences, Centrale Nantes	Examinateur

THÈSE DE DOCTORAT
NNT : 2022UPAST167

Acknowledgement

I would like to express my sincere gratitude to my supervisor, Dr. Marc Lambert, Chargé de recherche, Centre National de la Recherche Scientifique (CNRS). He has been an ideal thesis supervisor, offering generously continuous guidance and endless patience to me. I am grateful for my time working with him. His vast wisdom and wealth of experience have inspired me throughout my Ph.D. studies. What he taught me will be useful for my whole career.

I wish to express my appreciation to my co-supervisor Dr. Aurélia Fraysse, Associate Professor at Université Paris-Saclay, for her valuable suggestions on the research directions and her motivating guidance. Her explanation of various techniques lights the way ahead.

I would also like to express my sincere gratitude to my co-supervisor Dr. Dominique Lesselier, Directeur de Recherche Emérite, Centre National de la Recherche Scientifique (CNRS), for his warm support on my study and life during the three years. I have also benefited greatly from his wealth of knowledge, and opportunities he brought. I would like to warmly thank his lovely wife Laurence Lesselier for encouraging me when I was going through difficult times.

I want to extend my gratitude to Prof. Amélie Litman and Prof. Alexandre Baussard for serving as the referees, Dr. Sébastien Bourguignon as the jury member, and Prof. Laetitia Thirion-Lefevre as the charge of the presidency and the jury member. Thanks for their time spent reading my manuscript, and their valuable comments and suggestions that will certainly improve the work.

Warm thanks are given to my colleagues and friends Peipei Ran and Yingying Qin, for their valuable suggestions and assistance regarding my research and life. I would also like to thank my best friends Zhuoer Li and Ruochen Ding, who work in Nice but we share our happiness and our sorrows from a distance, thanks for their company during these years.

Finally, I would like to express my deepest gratitude to my family for their endless love and confidence. Special thanks are given to my cats Chouchou and Bibi for their lighting up my life.

Contents

List of Figures

List of Tables

Résumé en français

Le contexte de recherche

Cette thèse est une contribution aux problèmes de diffraction électromagnétique inverse (dorénavant notés ISP comme *Inverse Scattering Problems*). Les problèmes de diffraction directs consistent à déterminer la distribution des champs qui sont présents dans une zone donnée, à partir des informations sur les ondes incidentes sur cette zone, et sur le ou les diffracteurs en son sein. De manière correspondante, comme de fait l'inverse du problème direct, la résolution des ISP vise à retrouver les caractéristiques d'un ou de diffracteurs inconnus, telles que la géométrie ou la distribution des paramètres physiques, à partir de la connaissance des champs qu'il(ils) diffracte(nt) en présence de sources de rayonnement électromagnétique données (Chen 2018).

L'étude des ISP est une préoccupation constante car ceux-ci sont pertinents sous une forme ou sous une autre dans un large éventail d'applications (Pastorino et Randazzo 2018), telles, et sans exhaustivité, le contrôle non destructif (c'est-à-dire la détection des défauts d'un matériau, d'un composant ou d'un système sans y causer de dommages) (Ida *et al.* 2019 ; Zoughi 2000), l'imagerie médicale (par exemple, la détection des tumeurs du sein (Qin Sep 2021 ; Nikolova 2011)), la télédétection (Varotsos *et al.* 2020 ; Tsang, Kong et Shin 1985), et la caractérisation de matériaux (Alexopoulos *et al.* 2007).

Les problèmes directs de diffraction qui consistent donc à calculer les champs diffractés à partir de la résolution des équations pertinentes qu'ils satisfont sont linéaires et bien posés au sens de Hadamard, par exemple, une solution unique existe et elle dépend continûment des données. Au contraire, les problèmes inverses sont généralement mal posés. En particulier, contrairement aux autres problèmes inverses linéaires, tels la tomodensitométrie (Buzug 2011) ou la déconvolution (Campisi *et al.* 2017), les ISP sont non linéaires en raison des phénomènes de diffraction multiple.

Par conséquent, le défi de la mise en œuvre d'algorithmes fiables et efficaces pour les ISP est double. D'une part, les ISP souffrent d'un caractère mal posé, ce qui se traduit par des solutions qui ne sont pas uniques et sont très sensibles à toute variation de données ou de paramètres. D'autre part, le modèle inverse étant non linéaire, la fonction d'inadéquation aux données correspondante pour l'inversion est susceptible d'être non convexe, ce qui rend l'inversion plus difficile voire inefficace.

Objectif et organisation de la thèse

Cette thèse se concentre sur l'exploration des ISP bidimensionnels *full-wave*, où par *full-wave* on entend qu'aucune approximation de l'interaction électromagnétique n'est effectuée dans le modèle mis en place. D'une part, de nouvelles approches basées sur une méthode populaire d'inversion, dite de la source de contraste (CSI ou *Contrast Source Inversion*), sont proposées, qui combinent alors la technique des ondelettes et la régularisation par la parcimonie. D'autre part, une approche assistée par apprentissage profond est établie basée sur la méthode CSI et les réseaux de neurones convolutifs (*Convolutional Neural Networks*

ou CNN).

Une façon courante de s'attaquer aux ISP consiste à utiliser des approches déterministes, avec certaines informations préalables incorporées dans la fonction de coût à minimiser. La parcimonie est une information a priori largement utilisée à cet effet et la transformée discrète en ondelettes (*Discrete Wavelet Transform* ou DWT) (Mallat 2008) est souvent employée pour atteindre une représentation parcimonieuse de l'inconnu. Dans cette thèse, la première partie porte ainsi sur l'utilisation des ondelettes et la régularisation de la parcimonie dans les ISP, basée sur la méthode CSI mentionnée ci-dessus. Une approche multi-échelle basée sur les ondelettes est d'abord explorée. L'intégration de la parcimonie peut être réalisée en ajoutant des termes de régularisation, qui sont généralement sous la forme de normes vectorielles. Une approche pénalisée par la parcimonie par groupe est donc proposée, en ajoutant une norme mixte à la fonction de coût de la méthode CSI. Ensuite, la seconde partie concerne l'application de techniques d'apprentissage en profondeur pour s'attaquer aux ISP. La combinaison de la méthode itérative traditionnelle et du CNN est réalisée par une approche dite déroulée ou *unrolled*.

La thèse consiste en sept chapitres et est structurée comme suit :

- Le chapitre 1 décrit le contexte du travail et résume la contribution de la thèse. Une introduction générale aux problèmes inverses, aux algorithmes d'inversion pour les ISP et aux difficultés rencontrées est proposée.
- Le chapitre 2 présente la formulation du problème direct. La méthode des moments utilisée pour la modélisation est introduite.
- Le chapitre 3 illustre l'algorithme CSI traditionnel. La décomposition en ondelettes est brièvement introduite, et l'approche CSI basée sur les ondelettes est décrite.
- La transformée en ondelettes complexe à double arborescence est introduite au chapitre 4, et une méthode de solution de source de contraste pénalisée par la parcimonie par groupe est investiguée.
- Au chapitre 5, les détails du réseau de neurones convolutifs (CNN) sont introduits et la méthode déroulée est discutée.
- Au chapitre 6, un réseau de neurones convolutionnels déroulés dit CSI-Net est proposé, combiné avec la méthode CSI. Une comparaison avec l'état de l'art est effectuée. Ensuite, le CSI-Net est étendu au schéma multi-fréquence.
- Le chapitre 7 résume le travail accompli et introduit quelques perspectives.
- La dissémination associée au présent travail est précisée à la fin du manuscrit.

Problème direct de diffraction électromagnétique ($\S 2$)

Dans ce chapitre, le modèle direct est d'abord construit, le modèle inverse pouvant être dérivé de cette construction. Le problème de la diffaction électromagnétique direct consiste à modéliser l'interaction physique entre l'objet supposé bien connu et les données collectées, c'est-à-dire les champs diffractée. Le scénario considéré est un problème de diffraction électromagnétique bidimensionnel (2-D) harmonique dans le temps en polarisation magnétique transverse (TM) et le système de diffraction est configuré comme schématisé en figure 1 où l'objet est situé dans le domaine d'intérêt $\mathcal{D}$, inclu dans un espace libre $\mathcal{C}$, N_s sources et N_r récepteurs étant répartis de manière égale sur un cercle d'observation donné.

Le modèle direct qui implique deux équations intégrales de type source peut être établi comme suit

$$\boldsymbol{E}^{\text{tot}}(\boldsymbol{r}, \boldsymbol{r}_s) = \boldsymbol{E}^{\text{inc}}(\boldsymbol{r}, \boldsymbol{r}_s) + \int_{\mathcal{D}} G(\boldsymbol{r}, \boldsymbol{r}')J(\boldsymbol{r}', \boldsymbol{r}_s)d\boldsymbol{r}', \boldsymbol{r} \in \mathcal{D} \tag{1}$$

et

$$\boldsymbol{E}^{\text{diff}}(\boldsymbol{r}_r, \boldsymbol{r}_s) = \int_{\mathcal{D}} G(\boldsymbol{r}_r, \boldsymbol{r}')J(\boldsymbol{r}', \boldsymbol{r}_s)d\boldsymbol{r}', \boldsymbol{r} \in \mathcal{D}, \tag{2}$$

où $J(\boldsymbol{r}, \boldsymbol{r}_s)$ est la source de contraste $J(\boldsymbol{r}, \boldsymbol{r}_s) = \chi(\boldsymbol{r})\boldsymbol{E}^{\text{tot}}(\boldsymbol{r}, \boldsymbol{r}_s)$. $\boldsymbol{E}^{\text{tot}}$ sont respectivement les champs totaux, $\boldsymbol{E}^{\text{diff}}$ les champs diffractés, et $\boldsymbol{E}^{\text{inc}}$ les champs incidents. G représente la fonction de Green pertinente.

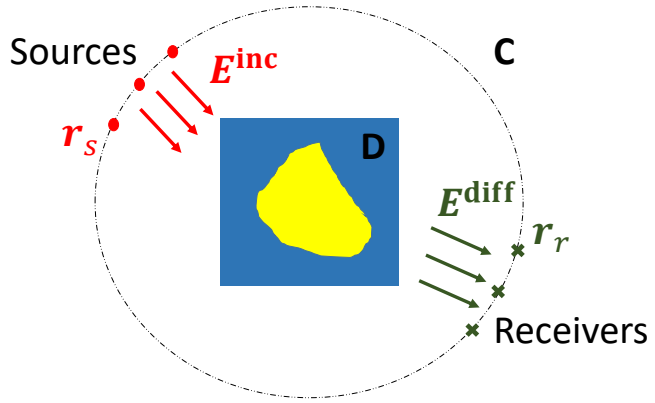

Figure 1 : La configuration du modèle.

Le problème direct consiste donc à calculer les champs diffractés en résolvant les équations ci-dessus, ce qui est un problème bien posé. Le problème inverse correspondant consiste à récupérer les informations physiques du diffracteur, e.g., la fonction de contraste $\chi(\boldsymbol{r})$, à partir des données collectées $\boldsymbol{E}^{\text{diff}}$ et des informations connues $\boldsymbol{E}^{\text{inc}}$ et G.

Ensuite, une méthode de moments (MoM, pour *Method of Moments*) est utilisée afin de transformer les équations intégrales vectorielles continues en équations algébriques scalaires discrètes : $\boldsymbol{E}_i^{\text{tot}} = \boldsymbol{E}_i^{\text{inc}} + \boldsymbol{G}_D\boldsymbol{J}_i$, $\boldsymbol{E}_i^{\text{diff}} = \boldsymbol{G}_S\boldsymbol{J}_i$ et $\boldsymbol{J}_i = \text{diag}(\boldsymbol{\chi})\boldsymbol{E}_i^{\text{tot}}$, où $i = 1, \ldots, N_s$ avec N_s le nombre de sources, $\boldsymbol{G}_D$ et $\boldsymbol{G}_S$ étant les fonctions de Green.

Méthode d'inversion de source de contraste et technique d'ondelettes (§3)

Ce chapitre présente une méthode d'inversion de source de contraste multi-échelle basée sur la transformée discrète en ondelettes (DWT) et la méthode traditionnelle d'inversion de source de contraste (CSI). Cette dernière consiste à minimiser une fonctionnelle de coût de la forme suivante

$$F(\boldsymbol{J}_i, \boldsymbol{\chi}) = \frac{\sum_{i=1}^{N_s} \|\boldsymbol{\xi}_i - \boldsymbol{G}_S\boldsymbol{J}_i\|^2}{\sum_{i=1}^{N_s} \|\boldsymbol{\xi}_i\|^2} + \frac{\sum_{i=1}^{N_s} \|\text{diag}(\boldsymbol{\chi})\boldsymbol{E}_i^{\text{inc}} - \boldsymbol{J}_i + \text{diag}(\boldsymbol{\chi})\boldsymbol{G}_D\boldsymbol{J}_i\|^2}{\sum_{i=1}^{N_s} \|\boldsymbol{\chi}\boldsymbol{E}_i^{\text{inc}}\|^2} \tag{3}$$

$\boldsymbol{\xi}_i$ étant les champs diffractés collectés.

En décomposant la fonction de contraste $\boldsymbol{\chi}$ avec la transformée en ondelettes discrète 2-D (DWT), l'algorithme CSI peut être exécuté dans le domaine des ondelettes. La DWT peut décomposer un signal donné

en différents niveaux et peut produire deux ensembles de coefficients : des coefficients dits d'approximation et des coefficients dits de détail. La méthode proposée traite des coefficients d'approximation. On part de la reconstruction des coefficients d'approximation à l'échelle la plus fine (le niveau maximum de décomposition) jusqu'à l'échelle la plus grossière (le niveau de décomposition est 1).

Dénotons la méthode proposée comme WCSI. Afin de comparer quantitativement les performances de la méthode CSI originale et de la WCSI, nous définissons une erreur de contraste reconstruite normalisée comme étant $\mathrm{Err}(\boldsymbol{\chi}) = \frac{\|\tilde{\boldsymbol{\chi}} - \boldsymbol{\chi}\|_2^2}{\|\boldsymbol{\chi}\|_2^2}$. Les deux méthodes sont testées sur le profil standard appelé « Autriche » sous différentes configurations pour lesquelles le nombre de sources N_s et de récepteurs N_r varient de 6 à 48. Les cartes d'erreur de $\mathrm{Err}(\boldsymbol{\chi})$ en fonction de N_s et N_r obtenues par deux méthodes sont fournies dans la figure 2. Nous pouvons voir sur celle-ci que les deux méthodes peuvent bien reconstruire les obstacles avec suffisamment de capteurs. Cependant, lorsque le nombre de capteurs diminue, WCSI surpasse CSI.

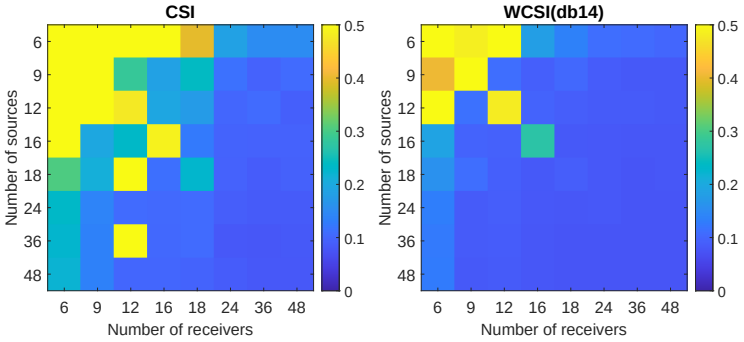

(a) CSI (b) WCSI (db14)

Figure 2 : Erreur de contraste normalisée en fonction de N_s et N_r. (a) CSI et (b) sont pour un CSI basé sur des ondelettes db14. Un bruit gaussien de $20\,\mathrm{dB}$ est ajouté aux champs diffractés.

Méthode d'inversion de source de contraste et parcimonie par groupe (§4)

Une caractéristique centrale de DWT est qu'il peut fournir une représentation clairsemée pour un signal donné. Comme mentionné dans le chapitre précédent, les coefficients d'ondelettes peuvent être divisés en deux : coefficients d'approximation et coefficients de détail. Les coefficients d'approximation qui représentent les composantes basses fréquences concentrent l'essentiel de l'énergie du signal. Les coefficients de détail qui contiennent des composantes hautes fréquences sont parcimonieux. De plus, la transformée en ondelettes produit naturellement une structure d'arbre quaternaire dépendante.

Dans ce chapitre, une méthode CSI pénalisée par la parcimonie par groupe est proposée sur la base de cette propriété importante des coefficients de détail des ondelettes. Cette dépendance a tendance à se propager à différentes échelles. Par conséquent, les coefficients d'ondelettes à ces différentes échelles peuvent être considérés comme statistiquement dépendants. En d'autres termes, les coefficients d'ondelettes peuvent être divisés en différents sous-groupes. Combinés à la parcimonie des coefficients de détail, les coefficients d'ondelettes peuvent être considérés comme parcimonieux de groupe (ou parcimonieux de structure). Au lieu de la méthode DWT, la transformée en ondelettes complexe à double arborescence

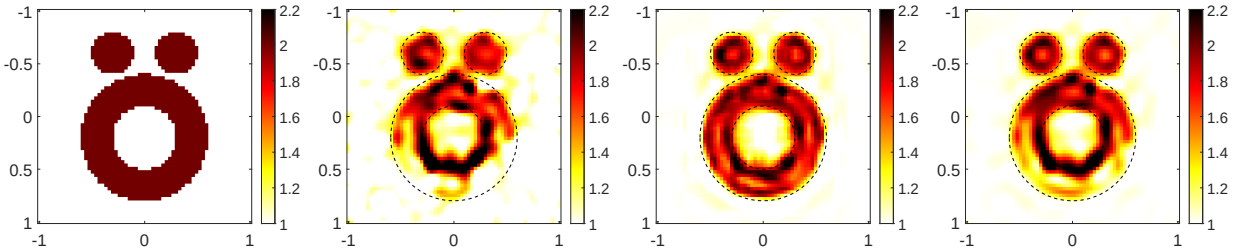

(a) Ground truth (b) CSI (c) GS-CSI (d) CSI+ℓ_1 norm

Figure 3 : (a) : Vérité terrain. Permittivité reconstruite par (b) CSI, (c) GS-CSI avec le premier arrangement de groupement, et (d) CSI ℓ_1-pénalisée. $N_s \times N_r = 16 \times 24$. Un bruit gaussien de $20\,\mathrm{dB}$ est ajouté aux champs diffractés.

(DT-$\mathbb{C}$WT) est utilisée car elle peut renforcer la dépendance entre les coefficients d'ondelettes.

D'un point de vue mathématique, pénaliser un problème d'optimisation peut être vu comme ajouter des termes de régularisation à la fonction de coût. La norme ℓ_1 est largement utilisée pour ajouter de la parcimonie comme information a priori aux problèmes d'optimisation. Cependant, avec la norme ℓ_1, chaque élément des entrées est considéré comme indépendant des autres. Pour prendre en compte l'information structurelle des coefficients d'ondelettes, la norme mixte $\ell_{2,1}$ qui favorise la parcimonie de groupe d'un signal donné est utilisée.

Trois arrangements de groupements sont proposés pour diviser les coefficients d'ondelettes en sous-groupes qui se chevauchent. La stratégie de réplication est utilisée dans le but de découpler les coefficients qui se chevauchent, de sorte que le problème d'optimisation pénalisé par la norme $\ell_{2,1}$ peut être résolu par la méthode de descente de gradient proximal avec un opérateur proximal dit de forme fermée. Des simulations exhaustives sont réalisées pour évaluer les performances de l'approche proposée. La figure 3 illustre les résultats obtenus par CSI, CSI pénalisé par la parcimonie par groupe (noté GS-CSI) et CSI pénalisé par la norme ℓ_1 pour préciser et de fait confirmer l'avantage de la méthode proposée.

Bases du réseau de neurones convolutifs (CNN) (§5)

L'apprentissage profond est un ensemble de méthodes d'apprentissage qui modélisent des données avec des architectures de réseau complexes et des transformations non linéaires. Au cours de la dernière décennie, plusieurs types de réseaux de neurones ont été développés. Les perceptrons multicouches, composés de plusieurs couches de perceptrons, sont les plus anciens et les plus simples. Les réseaux de neurones récurrents (*Recurrent Neural Networks* ou RNN) sont généralement utilisés pour traiter des données séquentielles telles que du texte ou des signaux de séries temporelles. Parmi ces différentes structures de réseau, le CNN est conçu pour traiter des données quadrillées, telles que des images.

CNN est généralement composé de trois types de couches. Ce sont des couches convolutionnelles, de mise en commun et entièrement connectées. Une architecture CNN peut être formée en empilant ces couches. Les couches de convolution et de regroupement sont utilisées pour l'extraction de caractéristiques, tandis que la couche entièrement connectée fournit les caractéristiques extraites dans la sortie finale. Dans ce chapitre, les couches de base et la technique de formation de CNN sont introduites, sur la base desquelles notre réseau peut être construit.

Ensuite, la méthode déroulée est présentée, méthode qui peut combiner efficacement les méthodes d'apprentissage et les méthodes traditionnelles, permettant de concevoir des modèles de réseaux pro-

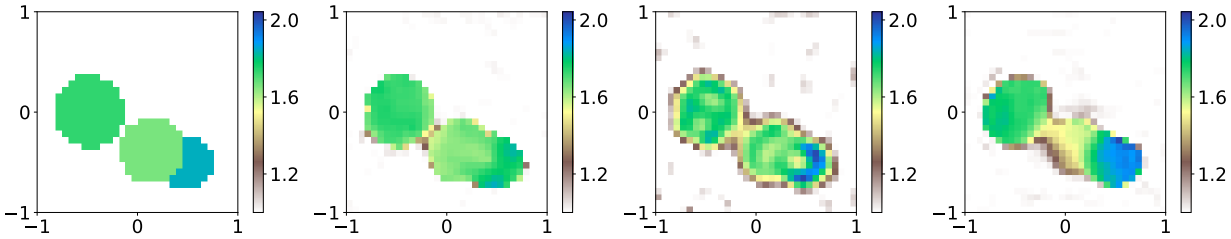

(a) Ground truth (b) CSI-Net (c) CSI (d) U-net

Figure 4 : (a) : Vérité terrain. Permittivité reconstruite par (b) CSI-Net, (c) CSI et (d) U-net. Un bruit gaussien de $20\,\mathrm{dB}$ est ajouté aux champs diffractés.

fonds plus robustes et plus interprétables.

Réseaux de neurones convolutionnels déroulés pour résoudre les ISPs (§6)

Les avantages de l'application d'outils d'apprentissage profond pour résoudre les ISP sont doubles. D'une part, elle permet une reconstruction en temps réel alors que les méthodes itératives traditionnelles nécessitent un temps de calcul qui peut être significatif. D'autre part, en tirant bénéfice des informations contenues dans des données à grande échelle, les outils d'apprentissage profond peuvent parfois résoudre des ISP fortement non linéaires pour lesquels les méthodes traditionnelles échouent.

L'intégration des connaissances physiques dans la méthode basée sur l'apprentissage est d'une grande importance. Dans ce chapitre, un schéma d'apprentissage profond déroulé pour résoudre les ISP non linéaires *full wave* est présenté. Une structure itérative de réseau de neurones combinant la méthode CSI et le réseau résiduel (*Residual neural Network* ou ResNet) est conçue, qui s'inspire de la méthode déroulée.

L'ensemble du réseau (dénommé ici CSI-Net) possède une architecture de blocs récurrente qui contient une série de sous-blocs. Chaque sous-bloc du réseau contient deux modules : *Module CSI* et *Module CNN*. Le *Module CSI* est construit sur la base de la méthode CSI et le *Module CNN* est empilé par blocs résiduels. Le nombre de sous-blocs dans l'ensemble du réseau et le nombre d'itérations CSI à l'intérieur de chaque sous-bloc sont prédéfinis et déterminent la complexité de la structure du réseau. De plus, chaque sous-bloc a une sortie distincte en raison de l'architecture récurrente du modèle. Pour former de manière égale chaque sous-bloc, une fonction de perte combinée construite avec l'erreur quadratique moyenne normalisée (*Mean Square Error* ou MSE) est conçue.

Le modèle proposé est entraîné avec les différentes bases de données. Le modèle entraîné est testé sur différents ensembles de données et des comparaisons sont effectuées entre CSI-Net, CSI et U-net (une structure de réseau largement utilisée pour traiter les ISP). La figure 4 montre un exemple d'obstacle reconstruit. Il s'agit d'une situation difficile car les diffracteurs sont proches les uns des autres et deux diffracteurs se chevauchent. Des artefacts apparaissent dans les résultats obtenus par CSI et la frontière des objets reconstruits obtenus par U-net n'est pas exacte. CSI-Net combine les avantages des deux côtés et en conséquence surpasse ici les deux méthodes.

Pour finir, le CSI-Net est également étendu au schéma multi-fréquence puisque son architecture récurrente est naturellement adaptée à la technique classique du saut de fréquence.

Conclusions et perspectives (§7)

Conclusions Les méthodes proposées peuvent être principalement classées en deux types : méthodes d'optimisation traditionnelles et méthodes basées sur l'apprentissage. Pour les méthodes traditionnelles, la transformée en ondelettes discrètes et la régularisation parcimonieuse mixte sont combinées avec la méthode CSI, tandis que la méthode basée sur l'apprentissage consiste à combiner CNN et la méthode CSI à travers un schéma déroulé.

Dans la première partie, la méthode CSI est combinée avec la transformée en ondelettes discrète 2-D classique. En transformant la fonction de contraste dans le domaine des ondelettes avec une base d'ondelettes donnée, on peut obtenir des coefficients d'ondelettes de différents niveaux, qui correspondent à différentes résolutions en fréquence. Rappelons que les coefficients d'ondelettes peuvent être divisés en deux parties, d'approximation et de détail. Les coefficients d'approximation contiennent des composantes basses fréquences et sont donc plus robustes au bruit. Une méthode CSI multi-échelle basée sur les ondelettes est proposée, combinant la propriété de multirésolution et les caractéristiques des coefficients d'approximation des ondelettes. Des simulations sont menées sur différentes configurations et avec des bases d'ondelettes variables afin de comparer les performances de CSI et de la méthode proposée.

Puis, pour atténuer le caractère mal posé des ISP, une pénalisation de parcimonie est ajoutée à la fonction coût de la méthode CSI, et une méthode CSI pénalisée par parcimonie par groupe est alors proposée. Au lieu d'employer la norme ℓ_1 largement utilisée pour imposer la contrainte de parcimonie, ici, une norme mixte $\ell_{2,1}$ est utilisée qui impose la parcimonie par groupe. La transformée en ondelettes discrète classique utilisée dans la première méthode est remplacée par la transformée en ondelettes complexe à double arborescence, qui permet de représenter la fonction de contraste de manière parcimonieuse et donne l'information de structure du contraste. Des simulations sont réalisées sur différentes configurations, et des comparaisons sont effectuées pour confirmer l'intérêt de la méthodologie proposée.

Dans la seconde partie, la technique d'apprentissage profond est appliquée pour résoudre les ISP. L'apprentissage profond a obtenu un grand succès dans la gestion des tâches de vision par ordinateur, mais n'a pas eu d'impact profond sur notre communauté. Dans notre travail, CNN est combiné avec la méthode CSI, et une structure de réseau déroulée est conçue. La connaissance du domaine est efficacement intégrée dans le processus d'apprentissage en intégrant des itérations CSI dans la structure du réseau. De plus, du fait de l'architecture itérative du réseau, le modèle proposé peut facilement être étendu au schéma multi-fréquence. Des tests numériques sont effectués pour évaluer les performances du modèle, et la stabilité, la robustesse et la fiabilité de l'approche proposée sont également analysées. Les comparaisons avec la structure U-net largement utilisée et CSI montrent l'avantage de la méthode proposée.

Pour résumer, des méthodes d'optimisation traditionnelles et des méthodes basées sur l'apprentissage pour résoudre les ISP à ondelettes complètes 2-D ont été développées et investiguées. Les méthodes CSI multi-échelles basées sur les ondelettes et les méthodes CSI pénalisées par la parcimonie par groupe montrent leurs avantages lorsqu'il s'agit de résoudre des problèmes dont les données collectées sont insuffisantes. Quant à la méthode basée sur l'apprentissage, elle permet une reconstruction en temps réel et elle bénéficie des informations contenues dans des données à grande échelle. En combinant alors CSI et CNN, la fiabilité du modèle est améliorée, cette fiabilité restant un vrai sujet de préoccupation pour les méthodes basées sur l'apprentissage.

Perspectives Dans cette thèse, plusieurs méthodes, y compris les approches d'optimisation traditionnelles et les approches d'apprentissage, ont donc été étudiées. Cependant, d'autres explorations apparaissent d'un grand intérêt.

Premièrement, pour la méthode basée sur les ondelettes multi-échelles, les critères d'arrêt peuvent être améliorés pour réduire la charge de calcul. Des recherches supplémentaires peuvent aussi être menées pour déduire quelle fonction de base d'ondelettes serait la plus appropriée à des domaines d'application spécifiques.

Dans la méthode CSI pénalisée par la parcimonie par groupe, au lieu d'utiliser des arrangements de groupe prédéfinis, le modèle d'arbre de Markov caché (*Hidden Markov Tree* ou HMT) peut être utilisé pour détecter dynamiquement le support des ondelettes lors des itérations (Deka *et al.* 2018). De plus, cette méthode se concentre sur les informations structurelles contenues dans les coefficients de détail des ondelettes. Les images avec plus d'informations détaillées devraient donc bénéficier davantage de cette approche. Par conséquent, il est logique d'appliquer cette approche à d'autres modèles contenant plus d'informations détaillées, tels que les modèles de sein en imagerie médicale.

La méthode CSI basée sur les ondelettes multi-échelles et la méthode CSI pénalisée par la parcimonie par groupe se concentrent respectivement sur les coefficients d'approximation des ondelettes et les coefficients détaillés des ondelettes. La combinaison des deux approches présente un grand intérêt.

En ce qui concerne le CSI-Net, la taille de pas de l'algorithme CSI n'est pas un paramètre apprenable. Faire de la taille du pas un paramètre apprenable est une voie à suivre, qui permet de simplifier la structure du réseau. Les informations physiques peuvent être intégrées dans le modèle non seulement via des entrées et des structures de réseau pré-initialisées, mais également via des modifications de la fonction de perte (*loss fnction*). La fonction de perte utilisée dans le travail actuel peut être encore modifiée en ajoutant des termes d'inadéquation aux données obtenus à partir de la connaissance du domaine, comme proposé dans (Liu, Roy *et al.* 2022).

De plus, toutes les méthodes proposées sont encore limitées aux situations 2-D et alors au cas de polarisation TM standard. Plus d'investigations doivent être menées pour les cas pleinement 3-D pour lesquels la modélisation mathématique est plus compliquée, et la non-linéarité et le caractère mal posé deviennent plus sévères. De plus, les méthodes proposées ne sont testées à ce stade que sur des données de simulation. D'autres tests devraient être effectués sur des données expérimentales, au départ en situation contrôlée de laboratoire.

1 Introduction

1.1 Research background

This thesis is a contribution to the electromagnetic inverse scattering problems (ISPs). The direct scattering problems are about determining the distribution of the fields present in a given area, based on information from incident waves and from the scatterer. Correspondingly, as the inverse to the direct problem, solving the ISPs aims at retrieving the characteristics of an unknown scatterer, such as its geometry or the distribution of its physical parameters, from the knowledge of the fields it scatters when it is illuminated by given electromagnetic sources (Chen 2018). Investigating the ISPs is a continuing concern since they are relevant to a wide range of applications (Pastorino and Randazzo 2018), including non-destructive testing (i.e., detecting defects of a material, component or system without causing damage) (Ida *et al.* 2019; Zoughi 2000), medical imaging (e.g., detecting breast tumors (Qin Sep 2021; Nikolova 2011), remote sensing (Varotsos *et al.* 2020; Tsang, Kong, and Shin 1985), and material characterization (Alexopoulos *et al.* 2007).

The direct scattering problems which consist in calculating the scattered fields based on the Maxwell equations are linear and well-posed in Hadamard's sense, e.g.,. a unique solution exists and it depends continuously on its data. On the contrary, inverse problems are generally ill-posed. Especially, different from other linear inverse problems, i.e., computed tomography (Buzug 2011), deconvolution (Campisi *et al.* 2017), the ISPs are non-linear due to multiple scattering. Hence, the challenge of implementing reliable and efficient algorithms for ISPs is twofold. On the one hand, ISPs suffer from ill-posedness, which results in non-unique and highly sensitive solutions. On the other hand, the inversion model being nonlinear, the corresponding data misfit function for inversion is likely to be non-convex, making the inversion more difficult and inefficient.

1.1.1 Overview of inversion techniques

Inverse problems are essentially optimization problems, which aim at minimizing the discrepancy between estimated results and expected ones

$$\boldsymbol{x} = \arg\min_{\boldsymbol{x}} F(\mathcal{O}, \mathcal{K}(\boldsymbol{x})) \tag{1.1}$$

$\mathcal{K}$ is the forward map (linear or nonlinear), $\mathcal{O}$ the measurements. $\boldsymbol{x}$ means the input elements to be optimized, F is the data misfit function which is usually modeled by the $L2$ norm (Euclidean norm). Iterative methods are most often employed to optimize the cost function and find the solution, and they are generally categorized into two types.

The *deterministic* methods consist in minimizing the cost function and searching for the optimal solution step by step according to the search direction and step size which are determined at each iteration. Deterministic methods are basically local optimization methods, which are efficient in finding local minima for non-convex optimization problems. Given an initial guess, the deterministic methods are capable of

searching the local minimum that is closest to the initial point. However, it is difficult for them to find the global optimal solution unless provided with a reasonable initial guess which is close to the global minimum. Moreover, deterministic methods can realize the local linearization of a nonlinear problem at each iterative step. There are some commonly used deterministic methods, e.g., steepest descent method (Curry 1944), conjugate gradient descent method (Dai *et al.* 1999), and Gauss-Newton algorithm (Hartley 1961). The nonlinear inverse problems can be tackled by linear or quasi-linear algorithms with a reasonable initial guess provided. Yet, such methods usually fail when the problem has a strong nonlinearity which increases the non-smoothness of the cost function, and as a result, a more complicated relationship between data and solution.

Another type of iterative optimization methods is called *stochastic* methods, e.g., colony optimization (Pastorino 2007), genetic algorithms (Qing *et al.* 2001), which have been proposed to remedy the drawback of local optimization methods. They have a better capability of finding the global minimum however with no global convergence guarantee, with a low convergence rate due to a larger computational burden compared to deterministic methods. In this thesis, the stochastic methods are not envisaged.

A central feature of inverse problems is ill-posedness. It can be interpreted as the lack of information, so that the solution either does not exist or cannot be uniquely determined. For instance, the ill-posedness of ISPs is caused by the presence of non-radiating currents which do not contribute to the scattered fields. To alleviate the ill-posedness of inverse problems, prior information should be added. From a mathematical point of view, regularization terms should be added to the original cost function, which allows the prior information to be integrated into the inversion process.

$$\boldsymbol{x} = \arg\min_{\boldsymbol{x}} \mathcal{F}(\mathcal{O}, \mathcal{K}(\boldsymbol{x})) + \Lambda \mathcal{G}(\boldsymbol{x}) \tag{1.2}$$

$\mathcal{G}(\cdot)$ is the regularization term, and Λ is the corresponding hyperparameter which is related to the trade-off between the data fitting term and regularization terms. Denote $\boldsymbol{x} = \mathcal{K}^{-1}(\boldsymbol{y})$ with $\mathcal{K}^{-1}$ the inverse operator of $\mathcal{K}$, there are two errors that are produced by the cost function (1.2)

$$e_1 = \tilde{\mathcal{K}}^{-1}(\boldsymbol{y}) - \boldsymbol{x} \tag{1.3}$$

$$e_2 = \tilde{\mathcal{K}}^{-1}(\mathcal{O}) - \tilde{\mathcal{K}}^{-1}(\boldsymbol{y}) \tag{1.4}$$

$\tilde{\mathcal{K}}^{-1}$ is the estimation of the inverse operator. e_1 , which is brought by the regularization term, measures the discrepancy between the estimated inverse operator and the real one. e_2 measures the misfit of observation and estimated data, which is represented by the data fitting term. However, $e_1$and e_2 cannot both reach a small value. Hence, the hyperparameter Λ controls the trade-off.

To quickly summarize, ill-posed inverse problems usually call for additional regularization terms to stabilize the inversion process. Various regularization schemes have been proposed (Engl *et al.* 2000) to insert the prior information or constraints, and a simple example is the positivity constraint. In addition, the Tikhonov regularization (Tikhonov *et al.* 1995) is one of the most commonly used techniques. Note that the regularization terms are also expressed by the ℓ_p norm of a vector/ matrix, which can be defined as

$$\|\boldsymbol{x}\|_p = \left(\sum_i |x_i|^p \right)^{\frac{1}{p}} \tag{1.5}$$

A general expression of the Tikhonov regularization term is $\mathcal{G}(\boldsymbol{x}) = \|\boldsymbol{x}\|_2^2$ which can penalize the entries with large norm. $\|\cdot\|_2$ is the ℓ_2 norm so it is also called ℓ_2 regularization. A major drawback of the Tikhonov regularization is the over-smoothness of the solution, i.e., the loss of non-smooth information. For example, the use of Tikhonov regularization in image reconstruction problems can lead to the loss of detail information in the image. (Rudin *et al.* 1992) introduces the total variation (TV) regularization, which is a well-known technique in noise removal. For a one dimensional digital signal $\boldsymbol{x}$, the TV regularization has the following form: $\mathcal{G}(\boldsymbol{x}) = \sum_i |x_{i+1} - x_i|$. It can reduce noise while keeping the detail information, e.g., the edges present in a 2-D image.

Sparsity (Bach *et al.* 2012) is also a widely used prior information that helps to improve the inversion results. A signal can be considered as *sparse* if most of its elements are zero, or almost zero. The simplest approach to determining whether a signal is sparse or not is to count its non-zero elements, which is exactly the definition of ℓ_0 norm

$$\|\boldsymbol{x}\|_0 = \#\{i = 1, \ldots, N | x_i \neq 0\} \tag{1.6}$$

By adding the ℓ_0 norm (Horn *et al.* 1985) as the regularization term, the number of nonzero elements contained in the data is penalized. Hence, sparsity can be enforced on the data. However, the optimization of a non-convex cost function with ℓ_0 norm is a NP-hard problem (Van Leeuwen 1991), which can be as difficult as trying out all possible non-zero supports of coefficients. A common solution is to replace the ℓ_0 norm with other indirect norms which can also promote the sparsity. A natural approximation of the ℓ_0 norm is the ℓ_1 norm, the solution of which has been verified to be very close to the sparsest solution (Donoho 2006). The optimization of a cost function with ℓ_1 norm embedded is also called the least absolute shrinkage and selection operator (LASSO) (Tibshirani 1996). Furthermore, some mixed norms (Kowalski 2009), e.g. $\ell_{2,1}$, $\ell_{\infty,1}$, can also promote the sparsity while preserving structural information of the signal.

In addition to iterative optimization approaches, deep-learning-based approaches have also been intensively investigated in recent years. Deep learning, mostly convolutional neural networks (CNN), has been widely applied in inverse imaging problems (Lucas *et al.* 2018; Jin *et al.* 2017), such as image denoising (Zhang and Salari 2005), restoration (Zhang, Zuo, *et al.* 2017), and super-resolution (Cui *et al.* 2014). Depending on whether the forward model $\mathcal{F}$ is known or not, different deep learning techniques can be applied. In our work, the forward model is fully known and one has full access to the paired ground truth and measurements. Hence, the simplest way to apply deep learning techniques is to construct a network that maps the measurements to the ground truth. As the forward model is known, some domain knowledge can be further incorporated into the network if provided with a reasonable initialization. Moreover, in addition to applying a single network to map the input to the output, the *unrolled* method (Ongie *et al.* 2020) has been proposed to tackle inverse problems, especially those for which the forward model is fully known. This approach is capable of integrating traditional iterative solvers into the CNN structure, which provides a fertile ground for future study.

The overview of the application of the above techniques in ISPs is provided in the following chapters.

1.1.2 Inverse scattering methods

As previously classified, there are three categories of methods for solving inverse problems: deterministic methods, stochastic methods, and deep-learning-assisted approaches.

For inverse scattering problems (ISPs), there are non-iterative deterministic methods like Rytov (Devaney

1981) and Born (Devaney 1982) approximations, which employ first-order approximations to linearize the problem. This type of methods requires less computational time, but they are mostly used for weak-enough scatterers. They can also be used as the initial point for iterative solvers.

To more rigorously deal with high contrast scatterers, a number of iterative methods with many variants have been developed. In the distorted Born iterative method (DBIM) (Chew and Wang 1990), the scatterer is regarded as a perturbation to the background medium. At each iteration, the incident fields and the Green functions are updated and the scattered fields generated by the perturbation part are minimized. Here, the nonlinear inverse problem is linearized at each iteration. The Contrast Source Inversion method (CSI) (Van den Berg *et al.* 2001) consists in minimizing the cost functional built with source-type integral equations. At each iteration, the contrast source and the contrast are alternatively updated, and the solution of the forward problem is avoided. The subspace-based optimization method (SOM) (Chen 2010) is also a widely used method that treats the source-type integral equations. It consists in determining the main part of the contrast source by spectral analysis, and then obtaining the remaining part by an optimization method. The contrast source is thus divided into two parts: signal subspace and noise subspace. Hence, this method enjoys good robustness against noise. Compared with first-order-approximation-based methods, iterative methods suffer from a higher computational burden yet they have a much wider range of applications.

Stochastic approaches, e.g., colony optimization method (Pastorino 2007) and genetic algorithms (Qing *et al.* 2001), have a better capability to find global optimal solutions, yet they are generally less popular in the community due to a large computational burden.

Deep-learning-assisted approaches for solving ISPs have been much investigated. A simple way to apply deep learning techniques is to directly regress the contrast distribution from the scattered fields, which is the input of the neural network, the output being the contrast. In (Ran, Qin, *et al.* 2021), the CNN is used to diagnose the damaged microstructure and the designed architecture takes the collected data as the input and outputs the contrast distribution.

Nevertheless, learning directly the contrast from the scattered fields requires unnecessary time to learn the known physical process. As a result, the combination of domain knowledge and neural networks has been much exploited. In (Wei *et al.* 2019a) and (Wei *et al.* 2019b), several physical-based learning approaches have been proposed such as the back-propagation scheme (BPS) and the induced current learning method (ICLM), which pre-initialize the input of the neural network based on the domain knowledge. In (Liu, Roy, *et al.* 2022), two physical-guided loss functions are proposed, which on the one hand enhance the noise robustness, and on the other hand, improve the reconstruction accuracy. These methods can reduce the nonlinearity of the relationship between the input and output of the neural network and simplify the learning process.

The neural network can be combined also with traditional optimization approaches. In (Sanghvi, Kalepu, *et al.* 2020), the learning process is followed by a refinement stage, where the SOM is applied in order to refine the result obtained from the previous stage. Apart from the CNN, the Generative Adversarial Network (GAN) (Goodfellow *et al.* 2014) and Recurrent Neural Network (RNN) have been applied also for tackling ISPs (Ran, Chen, *et al.* 2021; Ye *et al.* 2020; Song *et al.* 2021), yet one will not dwell upon those here as out of our scope.

1.2 Objective and outline

As introduced above, a common way to tackle the ISPs is to employ deterministic approaches, with some prior information incorporated in the cost function to minimize. Sparsity is a widely used prior information and the discrete wavelet transform (Mallat 2008) is often employed to reach a sparse representation of the unknown. In this thesis, the first part is about the use of sparsity in ISPs, based on the CSI method mentioned above. A wavelet-based multiscale approach is first explored. As previously mentioned, the integration of sparsity can be realized by adding regularization terms, which are usually of the form of vector norms. A group sparsity penalized approach is hence proposed, by adding a mixed norm to the cost function of CSI method. Then, the second part is about applying deep learning techniques to tackle the ISPs. The combination of traditional iterative methods and CNN is realized by the so-called *unrolled* approach.

The thesis contains eight main chapters in full and is structured as follows:

- Chapter 1 (here) describes the background of the work and summarizes the contribution of this thesis. An overall introduction of inverse problems, inversion algorithms for ISPs, and difficulties faced with is given.
- Chapter 2 presents the formulation of the forward problem. The method of moments that is used for modeling is briefly introduced.
- Chapter 3 illustrates the traditional CSI algorithm. The wavelet decomposition is briefly introduced, and the wavelet-based CSI approach is proposed.
- The dual-tree complex wavelet transform is introduced in Chapter 4, and a group sparsity penalized contrast source solution method is proposed.
- In Chapter 5, the details of the convolutional neural network (CNN) are introduced and the unrolled method is presented.
- In Chapter 6, an unrolled convolutional neural network CSI-Net is proposed, combined with the CSI method. A comparison with the state of the art is proposed. Then, the CSI-Net is extended to the multi-frequency scheme.
- Chapter 7 summarizes the achieved work and provides some perspectives.
- The dissemination associated with the present work is at the end of the manuscript.

2 Forward problem

In this chapter, the forward model is firstly built, from which the inverse model can be derived. The direct electromagnetic scattering problem is about modeling the physical interaction between the object that is supposed to be well-known, and the collected data, i.e., scattered fields.

2.1 Formulation

Consider a two-dimensional non-magnetic homogeneous isotropic object, immersed in a homogeneous medium contained in a given test domain. Assume that the object is infinitely long and uniformly distributed along the axis $\boldsymbol{z}$. The incident fields are uniformly distributed along the axis $\boldsymbol{z}$, and the polarization direction is parallel to the axis. The object is illuminated by time-harmonic electromagnetic waves $\boldsymbol{E}^{\text{inc}}(\boldsymbol{r})$ with time dependency $e^{-i\omega t}$, where ω is the angular frequency. Due to the phenomena of electromagnetic induction and polarization, the object can be regarded as a secondary source that emits secondary fields in the whole space, i.e., the scattered fields $\boldsymbol{E}^{\text{diff}}(\boldsymbol{r})$. $\boldsymbol{r} \in \mathcal{D}$ is a given observation point.

Maxwell's equations describe the properties of electromagnetic fields and the relationships between each component (Tsang, Kong, and Ding 2004). Their formulation in isotropic and homogeneous medium without source or charge reads as

$$\nabla \times \boldsymbol{E}(\boldsymbol{r}) = i\omega\mu \boldsymbol{H}(\boldsymbol{r}) \tag{2.1}$$

$$\nabla \times \boldsymbol{H}(\boldsymbol{r}) = \boldsymbol{J}(\boldsymbol{r}) - i\omega\varepsilon(\boldsymbol{r})\boldsymbol{E}(\boldsymbol{r}) = [\sigma(\boldsymbol{r}) - i\omega\varepsilon(\boldsymbol{r})]\, \boldsymbol{E}(\boldsymbol{r}) \tag{2.2}$$

$$\nabla \cdot \boldsymbol{E} = 0 \tag{2.3}$$

$$\nabla \cdot \boldsymbol{H} = 0 \tag{2.4}$$

where $\boldsymbol{E}$, $\boldsymbol{H}$ and $\boldsymbol{J}$ represent the electric and magnetic field strength, and the electric current density, respectively. $\mu = \mu_0\mu_r$ is the permeability with $\mu_0 = 4\pi \times 10^{-7}$ Henry/meter the permeability in free space, $\mu_r = 1$. $\varepsilon(\boldsymbol{r}) = \varepsilon_0\varepsilon_r$ is the permittivity with $\varepsilon_0 = 8.854 \times 10^{-12}$ Farad/meter the permittivity in free space and ε_r the relative permittivity of the scatterer. $\sigma(\boldsymbol{r})$ is the conductivity (σ = 0 Siemens/meter in free space).

By eliminating $\boldsymbol{H}$ in equations (2.1), (2.2), we have

$$\nabla \times \nabla \times \boldsymbol{E}(\boldsymbol{r}) = \varepsilon_c(\boldsymbol{r}) k_B^2 \boldsymbol{E}(\boldsymbol{r}) \tag{2.5}$$

where $\varepsilon_c(\boldsymbol{r}) = \varepsilon_r(\boldsymbol{r}) + \dfrac{i\sigma(\boldsymbol{r})}{\omega\varepsilon_0}$ is the complex relative permittivity, $k_B^2 = \omega^2\varepsilon_0\mu_0$ is the propagation constant of the embedding medium.

The incident fields $\boldsymbol{E}^{\text{inc}}(\boldsymbol{r})$ satisfy the scalar Helmholtz equation

$$\left(\nabla^2 + k_B^2\right) \boldsymbol{E}(\boldsymbol{r}) = 0 \tag{2.6}$$

and the total fields are the superposition of incident fields and scattered fields

$$\boldsymbol{E}^{\text{tot}}(\boldsymbol{r}) = \boldsymbol{E}^{\text{inc}}(\boldsymbol{r}) + \boldsymbol{E}^{\text{diff}}(\boldsymbol{r}) \tag{2.7}$$

From equations (2.5) and (2.6), we can get

$$\nabla \times \nabla \times \boldsymbol{E}^{\text{diff}}(\boldsymbol{r}) - k_B^2 \boldsymbol{E}^{\text{diff}}(\boldsymbol{r}) = k_B^2[\varepsilon_c(\boldsymbol{r}) - 1]\boldsymbol{E}^{\text{tot}}(\boldsymbol{r}) \tag{2.8}$$

wherein

$$\chi(\boldsymbol{r}) = k_B^2[\varepsilon_c(\boldsymbol{r}) - 1] = k^2(\boldsymbol{r}) - k_B^2 \tag{2.9}$$

is defined as the contrast function. Also, the scattered fields satisfy the Sommerfield radiation condition, so we have

$$\boldsymbol{E}^{\text{diff}}(\boldsymbol{r}) = \int_D G(\boldsymbol{r}, \boldsymbol{r'})\chi(\boldsymbol{r'})\boldsymbol{E}^{\text{tot}}(\boldsymbol{r'})d\boldsymbol{r'} \tag{2.10}$$

where $G(\boldsymbol{r}, \boldsymbol{r'})$ is Green's function, which represents the field at point $\boldsymbol{r}$ produced by a point source at $\boldsymbol{r}'$. Here, it is in 2-D case and given by

$$G(\boldsymbol{r}, \boldsymbol{r}') = \frac{-i}{4} H_0^{(1)}(k_B|\boldsymbol{r} - \boldsymbol{r'}|) = \frac{-i}{4}(J_0(k_B|\boldsymbol{r} - \boldsymbol{r'}|) + iY_0(k_B|\boldsymbol{r} - \boldsymbol{r'}|)) \tag{2.11}$$

where $H_0^{(1)}$ is the zero-order Hankel function of the first kind, J_0 and Y_0 are the zero-order Bessel and Neumann functions, respectively.

In this work, the transverse magnetic (TM) polarization is considered. The object is immersed in a domain of interest (DoI) $\mathcal{D}$ contained in free space $\mathcal{C}$. It is illuminated by TM waves generated by N_s ideal line sources located outside the scatterer at positions $\boldsymbol{r}_s$. For each illumination, the scattered fields are collected by N_r ideal receivers located at position $\boldsymbol{r}_r$ along a circle of observation $\mathcal{S}$, not intersecting the scatterer, and not necessarily jointing with the sources. By considering all those conditions, we now establish the forward model that involves two source-type integral equations.

The first one is called the *state equation*, which describes the interaction between the scatterer and the electromagnetic waves. The second one is the *data equation*, which describes the scattered fields generated by the scatterer. They have the following formulation

$$\boldsymbol{E}^{\text{tot}}(\boldsymbol{r}, \boldsymbol{r}_s) = \boldsymbol{E}^{\text{inc}}(\boldsymbol{r}, \boldsymbol{r}_s) + \int_{\mathcal{D}} G(\boldsymbol{r}, \boldsymbol{r'})J(\boldsymbol{r'}, \boldsymbol{r}_s)d\boldsymbol{r'}, \boldsymbol{r} \in \mathcal{D} \tag{2.12}$$

$$\boldsymbol{E}^{\text{diff}}(\boldsymbol{r}_r, \boldsymbol{r}_s) = \int_{\mathcal{D}} G(\boldsymbol{r}_r, \boldsymbol{r'})J(\boldsymbol{r'}, \boldsymbol{r}_s)d\boldsymbol{r'}, \boldsymbol{r} \in \mathcal{D} \tag{2.13}$$

with $J(\boldsymbol{r}, \boldsymbol{r}_s)$ the contrast source

$$J(\boldsymbol{r}, \boldsymbol{r}_s) = \chi(\boldsymbol{r})\boldsymbol{E}^{\text{tot}}(\boldsymbol{r}, \boldsymbol{r}_s) \tag{2.14}$$

The forward problem consists in calculating the scattered fields by solving the equations (2.12) and (2.13).

The forward model, the physical properties of the scatterer, and the domain knowledge are supposed to be well-known. Hence, it is a well-posed problem. The corresponding inverse problem is to retrieve the physical information of the scatterer, e.g., the contrast function $\chi(\boldsymbol{r})$, from the knowledge of the collected data $\boldsymbol{E}^{\text{diff}}$, and the known information $\boldsymbol{E}^{\text{inc}}(\boldsymbol{r})$ and $G(\boldsymbol{r}, \boldsymbol{r}')$.

2.2 Discretization of the forward model

To derive the discrete form of the equations, the Method of Moments (MoM) (Davidson 2005) is used, which transforms continuous vector integral equations into discrete scalar algebraic equations through two steps: discretization and testing. For simplicity, a pulse-basis point matching is employed for the discretization, and the delta testing functions are adopted for the testing step.

Let L be a linear operator, f is a known function, g is an unknown function, we have

$$Lf = g \tag{2.15}$$

One seeks to determine f knowing L and g, such that

$$\arg\min_{f} |g - Lf| \tag{2.16}$$

Expand f with a series of basis functions $\{u_n | n = 1, 2, \ldots, N\}$, with α_n decomposition coefficients

$$f = \sum_{n=1}^{\infty} \alpha_n u_n \approx \sum_{n=1}^{N} \alpha_n u_n = \tilde{f} \tag{2.17}$$

Combining (2.17) and (2.15), we have

$$g = L \sum_{n=1}^{N} \alpha_n u_n = \sum_{n=1}^{N} \alpha_n L u_n \tag{2.18}$$

In order to minimize the error between $\tilde{f}$ and f, a set of testing functions should be introduced $t_1, t_2, \ldots, t_K$, then the vector inner product is performed

$$\langle t_k, g \rangle_G = \sum_{n=1}^{N} \alpha_n \langle t_k, L u_n \rangle, \forall k = 1, \ldots, K \tag{2.19}$$

where $\langle \cdot \rangle_G$ is the inner product on G such that $\langle t_k, g \rangle_G = \int_G t_k(x) g^*(x) dx$. The equation (2.19) can be rewritten as

$$\boldsymbol{\omega} = \mathcal{L}\boldsymbol{\alpha} \tag{2.20}$$

with

$$\mathcal{L} = \begin{bmatrix} \langle t_1, Lu_1 \rangle & \langle t_1, Lu_2 \rangle & \ldots & \langle t_1, Lu_N \rangle \\ \langle t_2, Lu_1 \rangle & \langle t_2, Lu_2 \rangle & \ldots & \langle t_2, Lu_N \rangle \\ \vdots & \vdots & \ddots & \vdots \\ \langle t_K, Lu_1 \rangle & \langle t_K, Lu_2 \rangle & \ldots & \langle t_K, Lu_N \rangle \end{bmatrix}, \boldsymbol{\alpha} = \begin{bmatrix} \alpha_1 \\ \vdots \\ \alpha_N \end{bmatrix}, \boldsymbol{\omega} = \begin{bmatrix} \langle t_1, g \rangle \\ \vdots \\ \langle t_K, g \rangle \end{bmatrix}, \tag{2.21}$$

Hence, we have $\boldsymbol{\alpha} = \mathcal{L}^{-1}\boldsymbol{\omega}$, and

$$f = \sum_{n=1}^{N} (\mathcal{L}^{-1}\boldsymbol{\omega})_n u_n \tag{2.22}$$

By applying the MoM with pulse basis and point matching method, a discretized version of previous integral equations can be obtained. The DoI $\mathcal{D}$ is discretized into $N = N_x \times N_y$ small squares subunits, and the electric fields and permittivity are assumed to be constant within each unit. Every cell is approximated by a small disk with the same surface and equivalent radius R. The total field, the contrast function, and the contrast sources can be approximated as

$$\boldsymbol{E}^{\text{tot}}(\boldsymbol{r}) = \sum_{i=1}^{N} \boldsymbol{E}_i^{\text{tot}} C_n(\boldsymbol{r}) \tag{2.23}$$

$$\boldsymbol{\chi}(\boldsymbol{r}) = \sum_{i=1}^{N} \boldsymbol{\chi}_i C_n(\boldsymbol{r}) \tag{2.24}$$

$$J(\boldsymbol{r}) = \sum_{i=1}^{N} J_i C_n(\boldsymbol{r}) \tag{2.25}$$

where $C_n(\boldsymbol{r})$ is the basis function

$$C_n(\boldsymbol{r}) = \begin{cases} 0 & \boldsymbol{r} \notin D_i \\ 1 & \boldsymbol{r} \in D_i \end{cases} \tag{2.26}$$

where D_i represents the i-th cell.

As previously mentioned, the test functions are a set of delta functions δ which are located at the center of the subcells. By applying the test functions on the incident fields

$$\boldsymbol{E}^{\text{inc}}(\boldsymbol{r}) = \sum_{i=1}^{N} \boldsymbol{E}_i^{\text{inc}} \delta(\boldsymbol{r_i} - \boldsymbol{r}),\ \delta(\boldsymbol{r_i} - \boldsymbol{r}) = \begin{cases} 1\, \boldsymbol{r} = \boldsymbol{r}_i \\ 0\, \boldsymbol{r} \neq \boldsymbol{r}_i \end{cases} \tag{2.27}$$

where $\boldsymbol{r}_1, \ldots, \boldsymbol{r}_N$ are the centers of the sub cells. Then, decompose the state equation with the basis functions:

$$\boldsymbol{E}^{\text{tot}}(\boldsymbol{r}, \boldsymbol{r_s}) = \boldsymbol{E}^{\text{inc}}(\boldsymbol{r}, \boldsymbol{r}_s) + \sum_{i=1}^{N} \int_{D_i} G(\boldsymbol{r}, \boldsymbol{r}') C_n(\boldsymbol{r}') d\boldsymbol{r}' J_i, \tag{2.28}$$

and one projects the test functions by Eq. (2.27)

$$\begin{aligned} \boldsymbol{E}_j^{\text{tot}} &= \boldsymbol{E}_j^{\text{inc}} + \sum_{i=1}^{N} \int_{D_i} G(\boldsymbol{r}, \boldsymbol{r}') C_n(\boldsymbol{r}') d\boldsymbol{r}' J_i \\ &= \boldsymbol{E}_j^{\text{inc}} + \sum_{i=1}^{N} \int_{D_i} G(\boldsymbol{r}, \boldsymbol{r}') C_n(\boldsymbol{r}') d\boldsymbol{r}' \boldsymbol{\chi}_i \boldsymbol{E}_i^{\text{tot}},\ j = 1, \ldots N \end{aligned} \tag{2.29}$$

Now, we have a linearized system

$$\boldsymbol{E}_j^{\text{inc}} = \sum_{i}^{N} [\delta_{ji} - G_{ij}\chi_i] \boldsymbol{E}_i^{\text{tot}} \text{ with } G_{ij} = \int_{D_i} G(\boldsymbol{r}_j, \boldsymbol{r}') d\boldsymbol{r}' \tag{2.30}$$

the above equation can be rewritten as

$$\begin{bmatrix} E_1^{inc} \\ E_2^{inc} \\ \vdots \\ E_N^{inc} \end{bmatrix} = \begin{bmatrix} 1 - G_{11}\chi_1 & G_{12}\chi_2 & \dots & G_{1N}\chi_N \\ G_{21}\chi_1 & 1 - G_{22}\chi_2 & \dots & G_{2N}\chi_N \\ \vdots & \vdots & \ddots & \vdots \\ G_{N1}\chi_1 & 1 - G_{N2}\chi_2 & \dots & 1 - G_{NN}\chi_N \end{bmatrix} \times \begin{bmatrix} E_1^{tot} \\ E_2^{tot} \\ \vdots \\ E_N^{tot} \end{bmatrix}, \tag{2.31}$$

So, we have

$$\boldsymbol{E}_i^{\text{tot}} = \boldsymbol{E}_i^{\text{inc}} + \boldsymbol{G}_D \boldsymbol{J}_i,\ i = 1, \dots, N_s \tag{2.32}$$

with (Richmond 1965)

$$\boldsymbol{G}_D(\boldsymbol{r}, \boldsymbol{r}') = \begin{cases} \dfrac{ik_B\pi R}{2} J_1(k_B R) \mathrm{H}_0^{(1)}\left(k_B \left|\boldsymbol{r} - \boldsymbol{r}'\right|\right), & \boldsymbol{r} \neq \boldsymbol{r}' \\ \dfrac{ik_B\pi R}{2} \mathrm{H}_1^{(1)}(k_B R) - 1 & \text{otherwise} \end{cases} \tag{2.33}$$

where $R = \sqrt{\dfrac{\Delta_x \Delta_y}{\pi}}$, Δ_x and Δ_y are the length of small cell Δ.
Similarly, we have the observation equation for i_r-th receiver

$$\boldsymbol{E}_{i_r}^{\text{diff}}(\boldsymbol{r}) = \sum_{i=1}^{N} \left[\int_{D_i} G(\boldsymbol{r}, \boldsymbol{r}') \right] \chi_i \boldsymbol{E}_i^{\text{tot}} d\boldsymbol{r}', \tag{2.34}$$

for N_r receivers,

$$\begin{bmatrix} E_1^{\text{diff}} \\ E_2^{\text{diff}} \\ \vdots \\ E_{N_r}^{\text{diff}} \end{bmatrix} = \begin{bmatrix} G_{11} & G_{12} & \dots & G_{1N} \\ G_{21} & G_{22} & \dots & G_{2N} \\ \vdots & \vdots & \ddots & \vdots \\ G_{N_r 1} & G_{N_r 2} & \dots & G_{N_r N} \end{bmatrix} \times \begin{bmatrix} \chi_1 & & & 0 \\ & \chi_2 & & \\ & & \ddots & \\ 0 & & & \chi_N \end{bmatrix} \times \begin{bmatrix} E_1^{\text{tot}} \\ E_2^{\text{tot}} \\ \vdots \\ E_N^{\text{tot}} \end{bmatrix} \tag{2.35}$$

Thus, we have

$$\boldsymbol{E}_i^{\text{diff}} = \boldsymbol{G}_S \boldsymbol{J}_i \tag{2.36}$$

$$\boldsymbol{J}_i = \text{diag}(\boldsymbol{\chi}) \boldsymbol{E}_i^{\text{tot}} \tag{2.37}$$

where $i = 1, \dots, N_s$, and $\boldsymbol{G}_S(\boldsymbol{i}_r, \boldsymbol{r}) = \dfrac{ik_B\pi R}{2} \mathrm{J}_1(k_B R) \mathrm{H}_0^{(1)}(k_B |\boldsymbol{i}_r - \boldsymbol{r}|)$. Equations (2.32), (2.36), (2.37) are the discretized version of the source-type integral equations, which will be used for all the approaches developed in this thesis.

3 Contrast source inversion and wavelet technique

This chapter presents a multi-scale contrast source inversion method, based on the discrete wavelet transform (DWT). First, we present the details of Contrast Source inversion method (CSI). Then, the two-dimensional DWT is introduced based on which a wavelet-based CSI method is developed. Finally, numerical results are displayed.

3.1 Contrast source inversion method

The CSI method is one of the most used methods to tackle the ISPs. It is based on the modified gradient method (Kleinman *et al.* 1992). The cost function to minimize is built on source-type integral equations, which is the linear combination of a set of normalized mismatches. It is composed of two terms, one measures the error in the data equation, and the other measures the error in the object equation. The unknowns in the cost function are the contrast source $\boldsymbol{J}$ and the contrast $\boldsymbol{\chi}$. At each iteration, contrast source and contrast are updated alternatively, and the computation of the forward problem is avoided.

The cost functional stands as

$$F(\boldsymbol{J}_i, \boldsymbol{\chi}) = \frac{\sum_{i=1}^{N_s} \|\boldsymbol{\xi}_i - \boldsymbol{G}_S \boldsymbol{J}_i\|^2}{\sum_{i=1}^{N_s} \|\boldsymbol{\xi}_i\|^2} + \frac{\sum_{i=1}^{N_s} \|\mathrm{diag}(\boldsymbol{\chi}) \boldsymbol{E}_i^{\mathrm{inc}} - \boldsymbol{J}_i + \mathrm{diag}(\boldsymbol{\chi}) \boldsymbol{G}_D \boldsymbol{J}_i\|^2}{\sum_{i=1}^{N_s} \|\mathrm{diag}(\boldsymbol{\chi}) \boldsymbol{E}_i^{\mathrm{inc}}\|^2} \tag{3.1}$$

$\boldsymbol{\xi}_i$ being the measured scattered fields. In the following, $\mathrm{diag}(\boldsymbol{\chi}) \boldsymbol{E}_i^{\mathrm{inc/tot}}$ is written as $\boldsymbol{\chi} \boldsymbol{E}_i^{\mathrm{inc/tot}}$ for simplicity.

The contrast source $\boldsymbol{J}$ and the contrast $\boldsymbol{\chi}$ are alternatively retrieved with a conjugate gradient iterative method. At each iteration, the contrast source $\boldsymbol{J}$ is first updated by minimizing the entire cost functional. Then, the contrast $\boldsymbol{\chi}$ is obtained from the updated $\boldsymbol{J}$, meanwhile minimizing the object error. The minimization at each iteration is linear.

First, $\boldsymbol{J}$ and $\boldsymbol{\chi}$ are initialized by back-propagation as

$$\boldsymbol{J}_i^{\mathrm{bp}} = \frac{\|\boldsymbol{G}_S^* \boldsymbol{\xi}_i\|^2}{\|\boldsymbol{G}_S \boldsymbol{G}_S^* \boldsymbol{\xi}_i\|^2} \boldsymbol{G}_S^* \boldsymbol{\xi}_i \tag{3.2}$$

$$\boldsymbol{\chi}^{\mathrm{bp}} = \frac{\sum_{i=1}^{N_s} \boldsymbol{J}_i^{\mathrm{bp}} \boldsymbol{E}_i^{\mathrm{tot}*}}{\sum_{i=1}^{N_s} \|\boldsymbol{E}_i^{\mathrm{tot}}\|^2}. \tag{3.3}$$

Here, $\boldsymbol{E}_i^{\mathrm{tot}} = \boldsymbol{E}_i^{\mathrm{inc}} + \boldsymbol{G}_D \boldsymbol{J}_i^{\mathrm{bp}}$. $*$ is the conjugate transpose operator. At the k-th iteration, the data equation error $\boldsymbol{\rho}_{i,k}$ and the state equation error $\boldsymbol{r}_{i,k}$ are first determined

$$\boldsymbol{\rho}_{i,k} = \boldsymbol{\xi}_i - \boldsymbol{G}_S \boldsymbol{J}_{i,k-1} \tag{3.4}$$

$$\boldsymbol{r}_{i,k} = \boldsymbol{\chi}_{k-1} \boldsymbol{E}_{i,k-1}^{\mathrm{tot}} - \boldsymbol{J}_{i,k-1}. \tag{3.5}$$

Then, the contrast source $\boldsymbol{J}_{i,k}$ is updated by the conjugate-gradient method as

$$\boldsymbol{J}_{i,k} = \boldsymbol{J}_{i,k-1} + \alpha_k^J \boldsymbol{\nu}_{i,k} \tag{3.6}$$

with $\boldsymbol{\nu}_{i,k}$ the search direction

$$\boldsymbol{\nu}_{i,k} = \boldsymbol{g}_{i,k}^J + \frac{\Re\left\{\sum_i \left\langle \boldsymbol{g}_{i,k}^J, \boldsymbol{g}_{i,k}^J - \boldsymbol{g}_{i,k-1}^J \right\rangle\right\}}{\sum_i \left\langle \boldsymbol{g}_{i,k-1}^J, \boldsymbol{g}_{i,k-1}^J \right\rangle} \boldsymbol{\nu}_{i,k-1} \tag{3.7}$$

where $\boldsymbol{g}_k^J$ is the Fréchet derivative evaluated at $\boldsymbol{J}_{k-1}$ and $\boldsymbol{\chi}_{k-1}$.

$$\boldsymbol{g}_{i,k}^J = -\frac{\boldsymbol{G}_S^* \boldsymbol{\rho}_{i,k}}{\sum_i \|\boldsymbol{\xi}_i\|^2} - \frac{\boldsymbol{r}_{i,k} - \boldsymbol{G}_D^* \boldsymbol{\chi}_{k-1} \boldsymbol{r}_{i,k}}{\sum_i \|\boldsymbol{\chi}_{k-1} \boldsymbol{E}_i^{\text{inc}}\|^2} \tag{3.8}$$

and the step size α_k^J is defined as

$$\alpha_k^J = \frac{-\sum_i \left\langle \boldsymbol{g}_{i,k}^J, \boldsymbol{v}_{i,k} \right\rangle}{\frac{\sum_i \|\boldsymbol{G}_S \boldsymbol{\nu}_{i,k}\|^2}{\sum_i \|\boldsymbol{\xi}_i\|^2} + \frac{\sum_i \|\boldsymbol{\nu}_{i,k} - \boldsymbol{\chi}_{k-1} \boldsymbol{G}_D \boldsymbol{\nu}_{i,k}\|^2}{\sum_i \|\boldsymbol{\chi}_{k-1} \boldsymbol{E}_i^{\text{inc}}\|^2}} \tag{3.9}$$

Then, the total field is updated by

$$\boldsymbol{E}_{i,k}^{\text{tot}} = \boldsymbol{E}_i^{\text{inc}} + \boldsymbol{G}_D \boldsymbol{J}_{i,k} \tag{3.10}$$

The contrast $\boldsymbol{\chi}$ is updated from $\boldsymbol{J}$ by an analytical solution

$$\boldsymbol{\chi}_k = \frac{\sum_{i=1}^{N_s} \boldsymbol{J}_{i,k} \boldsymbol{E}_{i,k}^{\text{tot}*}}{\sum_{i=1}^{N_s} \|\boldsymbol{E}_{i,k}^{\text{tot}}\|^2} \tag{3.11}$$

Note that a positivity constraint is imposed on the contrast via the projection method (Van den Berg *et al.* 2001) by imposing $\varepsilon_r(\boldsymbol{r}) \geq 1$ and $\sigma(\boldsymbol{r}) \geq 0$. The algorithm is sketched in Algorithm 1.

Algorithm 1 CSI

1: Initialize $\boldsymbol{J}$ and $\boldsymbol{\chi}$ by back-propagation
2: **repeat**
3: Calculate the data error $\boldsymbol{\rho}_{i,k}$ and the object error $\boldsymbol{r}_{i,k}$
4: Calculate the gradient $\boldsymbol{g}_{i,k}^J$
5: Calculate the search direction $\boldsymbol{\nu}_{i,k}$
6: Determine the step size α_k^J
7: **Update the contrast sources** $\boldsymbol{J}_{i,k}$
8: Update the total field $\boldsymbol{E}_{i,k}^{\text{tot}}$
9: **Update the contrast** $\boldsymbol{\chi}_k$
10: Enforce positivity constraint on $\boldsymbol{\chi}_k$
11: **until** a stopping criterion is satisfied.

3.2 Review of wavelet transform

The *Fourier Transform* (FT) (Bracewell *et al.* 1986) can transform a time-domain signal into the frequency domain. However, the frequency information can only be retrieved in a vague manner, i.e., the time when each frequency component appears is unknown, which can be explained by the Heisenberg uncertainty principle (Busch *et al.* 2007). The wavelet transform is one of the solutions to overcome this shortcoming of FT, as it can simultaneously yield time and frequency information with different resolutions.

To introduce the *Wavelet transform* (WT), we first define the decomposition of a given signal into the linear combination of a basis as

$$x(t) = \sum_k a_k b_k(t) \tag{3.12}$$

with k an integer that could be finite or infinite, a_k the decomposition coefficients, and $b_k(t)$ the basis. Consider $\tilde{b}_k(t)$ the dual function of $b_k(t)$, then we can find the decomposition coefficients by the orthonormal relation between the dual pairs

$$a_k = \left\langle x(t), \tilde{b}_k(t) \right\rangle = \int x(t)\tilde{b}_k^*(t)dt \tag{3.13}$$

where * is the complex conjugation.

3.2.1 Continuous wavelet transform

The WT was first introduced to provide a novel mathematical tool for seismic wave analysis. The *Continuous wavelet transform* (CWT) has the following formulation:

$$y(s,\tau) = \int x(t)\Psi_{s,\tau}^*(t)dt \tag{3.14}$$

where s is the continuous scaling parameter, and τ is the translation parameter. $\Psi_{s,\tau}(t)$ represents the wavelets, which is a family of functions generated by applying translations and dilations on a "mother wavelet", defined as

$$\Psi_{s,\tau}(t) = \frac{1}{\sqrt{s}}\Psi\left\{\frac{t-\tau}{s}\right\}. \tag{3.15}$$

Equation (3.14) signifies the decomposition of $x(t)$ by the wavelets $\Psi_{s,\tau}(t)$, and the inverse wavelet transform is given by

$$x(t) = \int\int y(s,\tau)\Psi_{s,\tau}(t)d\tau ds. \tag{3.16}$$

Real-world signals can be classified into continuous signals and discrete signals. The CWT can tackle continuous signals such as the recording of a speech signal or a music signal, which can be formulated as functions of time.

3.2.2 Discrete wavelet transform

In practice, the collected signals are discrete signals, which are generally non-continuous and contained within a limited interval. Discrete signals, e.g., digital images, should be tackled by the *Discrete wavelet transform* (DWT). To make the WT discrete, the wavelets should be discretized. They are not time-discrete, but discrete with respect to the translation and scale steps. Define the discretized wavelet function and

scaling function as

$$\Psi_{j,k}(\boldsymbol{r}) = 2^{j/2}\Psi(2^j\boldsymbol{r} - k) \tag{3.17}$$

$$\Phi_{j,k}(\boldsymbol{r}) = 2^{j/2}\Phi(2^j\boldsymbol{r} - k) \tag{3.18}$$

where j is the dilation parameter, and k is the position parameter. The scaling function $\Phi(\boldsymbol{r})$ is used for approximating the signals and the wavelet function $\Psi(\boldsymbol{r})$ is used to retrieve the details. Consider a discrete signal $x(\boldsymbol{r})$, it can be decomposed by

$$x(\boldsymbol{r}) = \sum_k W_\Phi(j_0, k)\Phi_{j_0,k}(\boldsymbol{r}) + \sum_{j=j_0}^{\infty}\sum_k W_\Psi(j,k)\Psi_{j,k}(\boldsymbol{r}) \tag{3.19}$$

and the wavelet coefficients can be obtained by

$$W_\Phi(j_0, k) = \langle x(\boldsymbol{r}), \Phi_{j_0,k}(\boldsymbol{r})\rangle \tag{3.20}$$

$$W_\Psi(j,k) = \langle x(\boldsymbol{r}), \Psi_{j,k}(\boldsymbol{r})\rangle, j \geq j_0 \tag{3.21}$$

$W_\Phi(j_0, k)$ are approximation coefficients and $W_\Psi(j,k)$ are detail coefficients. In practice, the scaling function and wavelet function are known, e.g., Haar, Daubechies, .etc. (Chui 1992).

The Haar wavelet is a very simple wavelet, and it is widely adopted to analyze the discrete signal, its mother wavelet function is

$$\Psi(\boldsymbol{x}) = \begin{cases} 1 & 0 \leq \boldsymbol{x} < \frac{1}{2} \\ -1 & \frac{1}{2} \leq \boldsymbol{x} < 1 \\ 0 & \text{otherwise.} \end{cases} \tag{3.22}$$

and its scaling function can be described as

$$\Phi(\boldsymbol{x}) = \begin{cases} 1 & 0 \leq \boldsymbol{x} < 1 \\ 0 & \text{otherwise.} \end{cases} \tag{3.23}$$

The Daubechies wavelets are a family of orthogonal wavelets dedicated to the DWT, which are characterized by a higher number of vanishing moments A (which is also called *tap*). The length of the Daubechies wavelets is related to their vanishing moments. For a Daubechies wavelet with A vanishing moments, its wavelet filter and scaling filter are both of length $2A$. When $A = 1$, the corresponding Daubechies wavelet is denoted as $D2$ or $dB1$, it is the Haar wavelet.

A two-dimensional (2-D) image can be represented as a matrix of pixels. When applying the two-dimensional DWT to process an image, the pixels are decomposed into wavelet coefficients, which depend on the change rate of the pixel values. The areas where the pixel values rapidly change correspond to the high-frequency wavelet coefficients, whereas the areas that gradually change are transformed into low-frequency components.

As shown in Fig. 3.1, an image $\boldsymbol{X}$ to be decomposed is firstly passed through two filters: low-pass filter and high-pass filter. The coefficients of the low-pass filters for $D2 - 20$ are detailed in Appendix A. The corresponding wavelet coefficients can be derived from the scaling coefficients. The low-pass filter is used to approximate the image, and the other can extract information on edges. Then, the image can

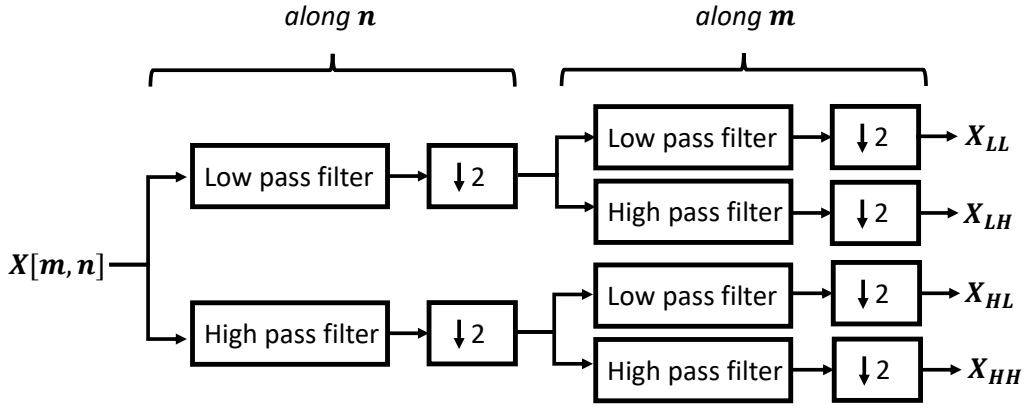

Figure 3.1: Decompose a $m \times n$ image $\boldsymbol{X}$ by 2-D DWT of level 1.

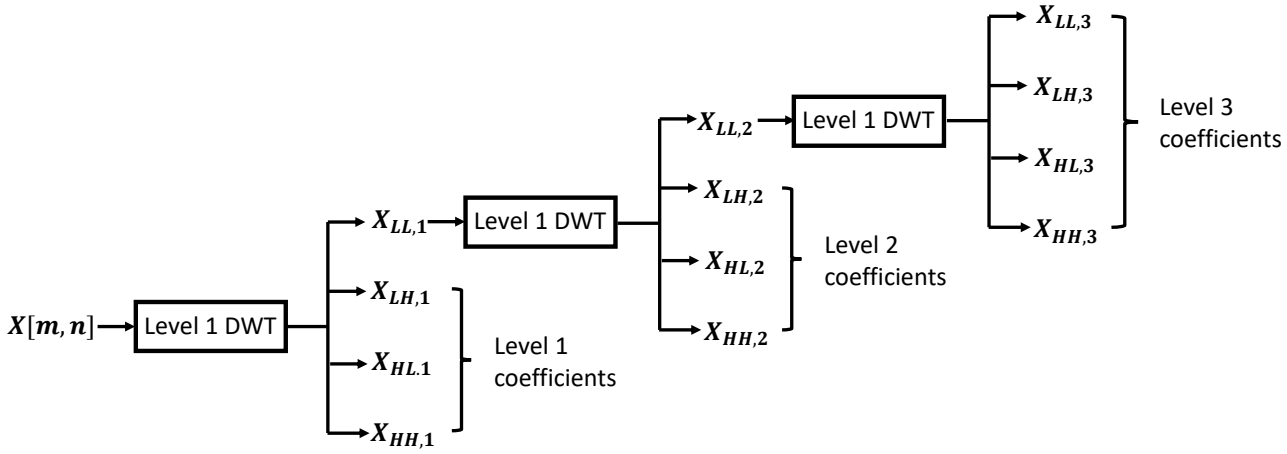

Figure 3.2: Decompose a $m \times n$ image $\boldsymbol{X}$ by 2-D DWT of level 3.

be decomposed into two parts: low-frequency components and high-frequency components. Next, the two sub-images repeat the previous operation, respectively. Finally, we can get 4 sub-images of level 1, corresponding to 4 spatially oriented frequency channels:

- $\boldsymbol{X}_{LL}$: A re-scaled approximation of the original image
- $\boldsymbol{X}_{HL}$: Horizontal details information
- $\boldsymbol{X}_{LH}$: Vertical details information
- $\boldsymbol{X}_{HH}$: Diagonal details information

By repeating the 1-level decomposition on the LL components, we can obtain wavelet coefficients of higher levels, as shown in Fig. 3.2. The frequency resolution is increased with the decomposition level increasing. Figure 3.3 shows the location of wavelet coefficients in the transformed matrix. For the coefficients of level 1 or higher levels, the approximation coefficients are always located within the upper left corner, and the rest are detail coefficients. Note that the side length of the input image must be a multiple of 2^L where L is the decomposition level. The maximum level that can be reached is $L_{\text{max}} = \log_2 \sqrt{N}$ where $\sqrt{N}$ is the side length of the input image.

Figure 3.3: Wavelet coefficients generated by 2-D DWT. Left: 1-level decomposition. Right: 3-level decomposition.

3.3 Multi-scale wavelet based CSI

As mentioned above, applying the 2-D DWT on a given image produces wavelet coefficients of different levels corresponding to different frequency resolutions. Incorporating the DWT into classical inversion methods is attracting much attention due to its multiresolution representation. Our work aims to build up a CSI method in the wavelet domain, combined with the multiresolution property, to see which configuration might outperform the classical CSI approach in the spatial domain.

In (Li, Semerci, *et al.* 2013), the authors have transformed the cost function of CSI into the wavelet domain. First, define the wavelet coefficients of the contrast source $\boldsymbol{J}$ and $\boldsymbol{\chi}$ as

$$\boldsymbol{\gamma} = \mathcal{W}\{\boldsymbol{J}\} \tag{3.24}$$

$$\boldsymbol{\beta} = \mathcal{W}\{\boldsymbol{\chi}\} \tag{3.25}$$

the data equation error $\boldsymbol{\rho}_{i,k}$ and the state equation error $\boldsymbol{r}_{i,k}$ are also transformed into wavelet domain

$$\boldsymbol{\rho}_{i,k}^{\mathcal{W}} = \boldsymbol{\xi}_i - \boldsymbol{G}_S \mathcal{W}^*\{\boldsymbol{\gamma}_{i,k-1}\} \tag{3.26}$$

$$\boldsymbol{r}_{i,k}^{\mathcal{W}} = \mathcal{W}\{\mathcal{W}^*\{\boldsymbol{\beta}_k\}\boldsymbol{E}_i^{\text{inc}}\} + \mathcal{W}\{\mathcal{W}^*\{\boldsymbol{\beta}_k\}\boldsymbol{G}_D\mathcal{W}^*\{\boldsymbol{\gamma}_i\}\} - \boldsymbol{\gamma}_i \tag{3.27}$$

Thus, with all elements defined above, the cost function of CSI can also be transformed into the wavelet domain

$$F^{\mathcal{W}}(\boldsymbol{\gamma}_i, \boldsymbol{\beta}) = \frac{\sum_{i=1}^{N_s} \|\boldsymbol{\rho}_{\boldsymbol{i}}^{\boldsymbol{\mathcal{W}}}\|^2}{\sum_{i=1}^{N_s} \|\boldsymbol{\xi}_i\|^2} + \frac{\|\boldsymbol{r}_i^{\mathcal{W}}\|^2}{\sum_{i=1}^{N_s} \|\mathcal{W}\{\mathcal{W}^*\{\boldsymbol{\beta}\}\boldsymbol{E}_i^{\text{inc}}\}\|^2} \tag{3.28}$$

Compared to the original cost function $F(\boldsymbol{J}_i, \boldsymbol{\beta})$, $F^{\mathcal{W}}(\boldsymbol{\gamma}_i, \boldsymbol{\beta})$ is a function of $\boldsymbol{\gamma}_i$ and $\boldsymbol{\beta}$ instead of $\boldsymbol{J}_i$ and $\boldsymbol{\chi}$.

At each iteration, the contrast source and the contrast are first transformed into the wavelet domain, so we can operate on their wavelet coefficients. Then, the spatial domain coefficients are reconstructed from the modified wavelet coefficients.

As introduced above, on the one hand, the wavelet coefficients include two main parts: approximation coefficients and detail coefficients. Approximation coefficients contain low-frequency components, while the detail coefficients contain high-frequency components which are expected to be more contaminated with noise. Therefore, the approximation coefficients are more robust to noise and they concentrate most of the energies. On the other hand, different decomposition levels L yield decomposition coefficients at

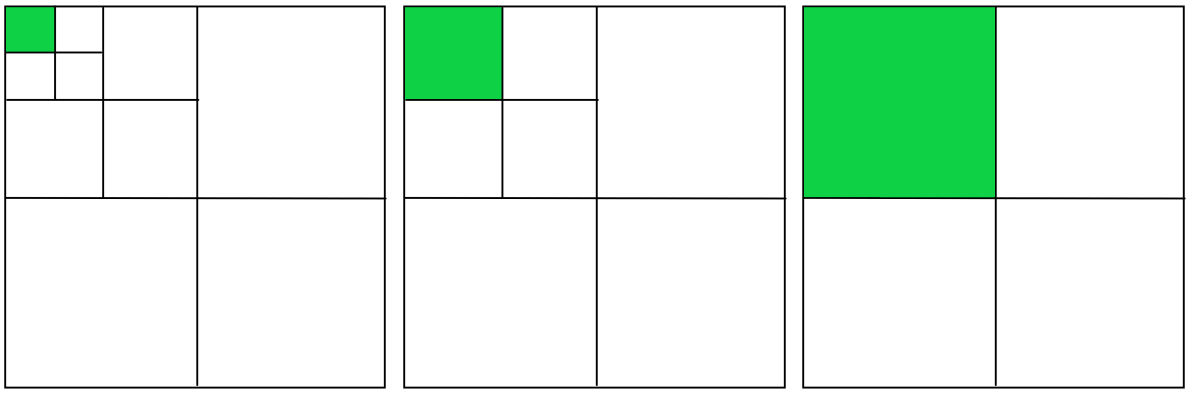

(a) Step 1: $L = 3$ (b) Step 2: $L = 2$ (c) Step 3: $L = 1$

Figure 3.4: Localization of wavelet coefficients employed in the optimization steps.

different scales.

Based on these two properties, a new strategy can be established. Here, only approximation coefficients are concerned. We start from the reconstruction of approximation coefficients at the finest scale (the maximum level of the decomposition L_{max}). Once the reconstruction at the current level L is finished, the result will be used as the initialization for the next step, where the approximation coefficients at scale $L = L - 1$ are updated. This step is repeated until L reaches 1.

Figure 3.4 gives an example of the optimization steps. Suppose that the optimization starts from $L_{\text{max}} = 3$, at this step, only the approximation coefficients LL_3 are updated, as displayed in 3.4(a). This first step provides the inversion with a stable starting point. In the next steps, more approximation coefficients at different scales are involved in the inversion until the decomposition reaches the coarsest scale, as shown in 3.4(c).

Here, only the wavelet coefficients of the contrast $\boldsymbol{\chi}$ are concerned, so we can simplify the equation (3.28) as

$$F^{\mathcal{W}}(\boldsymbol{J}_i, \boldsymbol{\beta}) = \frac{\sum_{i=1}^{N_s} \|\boldsymbol{\rho_i}\|^2}{\sum_{i=1}^{N_s} \|\boldsymbol{\xi}_i\|^2} + \frac{\sum_{i=1}^{N_s} \left\|\mathcal{W}^*\{\boldsymbol{\beta}\}\boldsymbol{E}_i^{\text{inc}} + \mathcal{W}^*\{\boldsymbol{\beta}\}\boldsymbol{G}_D\boldsymbol{J}_i - \boldsymbol{J}_i\right\|^2}{\sum_{i=1}^{N_s} \left\|\mathcal{W}^*\{\boldsymbol{\beta}\}\boldsymbol{E}_i^{\text{inc}}\right\|^2} \tag{3.29}$$

Compared to equation (3.28), the above equation is a function of $\boldsymbol{J}_i$ and $\boldsymbol{\beta}$. At each iteration, only the contrast has to be decomposed, which reduces the computational burden. The algorithm of the WCSI is summarized in Algorithm 2.

3.4 Numerical results

3.4.1 Test with "Austria" profile

In the numerical simulation, the so-called "Austria" profile is used, which contains two disks and one ring, as shown in Fig. 3.5(a). The scatterer is lossless, the relative permittivity $\varepsilon(\boldsymbol{r})$ is 2 for the object, and for the embedding medium, $\varepsilon_b = 1$. The region of interest $\mathcal{D}$ is $l = 2\,\text{m}$ sided. For the direct problem, $\mathcal{D}$ is discretized into 50×50 cells, and for the inverse one, it is discretized into 64×64 pixels. The scattering system is shown in Fig. 3.5(b), the region of interest is contained in free space $\mathcal{C}$. N_s sources and N_r receivers are evenly distributed along an observation circle of radius $r = 3.75\,\text{m}$. The operating frequency is $500\,\text{MHz}$, and the collected data are corrupted by Gaussian noise.

Algorithm 2 Wavelet-based CSI (WCSI)

Initialize $\boldsymbol{J}$ and $\boldsymbol{\chi}$ by back-propagation
Initialize the level of decomposition $L = L_{\text{max}}$
while $L > 0$ **do**
  repeat
    Calculate the data error $\boldsymbol{\rho}_{i,k}$ and the object error $\boldsymbol{r}_{i,k}$.
    Calculate the gradient $\boldsymbol{g}_{i,k}^{J}$
    Calculate the search direction $\boldsymbol{\nu}_{i,k}$
    Determine the step size α_k^J
    Update the contrast sources $\boldsymbol{J}_{i,k}$
    Update the total field $\boldsymbol{E}_{i,k}^{\text{tot}}$
    Update the contrast $\boldsymbol{\beta}_k$ by $\boldsymbol{\beta}_k = \mathcal{W}\left\{\dfrac{\sum_{i=1}^{N_s}\boldsymbol{J}_{i,k}\boldsymbol{E}_{i,k}^{\text{tot}*}}{\sum_{i=1}^{N_s}\left\|\boldsymbol{E}_{i,k}^{\text{tot}}\right\|^2}\right\}$
    Keep only the approximation coefficients
    Reconstruct the spatial-domain contrast by $\boldsymbol{\chi}_k = \mathcal{W}^*\boldsymbol{\beta}_k$
    Enforce positivity constraint on $\boldsymbol{\chi}_k$
  until a stopping criterion is satisfied
  $L = L - 1$
  Set current result as the initialization of the next step
end while

To quantitatively evaluate the quality of reconstruction, we define the normalized reconstructed contrast error as

$$\text{Err}(x) = \frac{\|\tilde{x} - x\|_2^2}{\|x\|_2^2} \quad \{x = \boldsymbol{\chi}, \Re(\boldsymbol{\chi}), \Im(\boldsymbol{\chi})\} \tag{3.30}$$

where x is the parameter to evaluate and $\tilde{x}$ is the reconstruction of x, $\Re(\cdot)$, $\Im(\cdot)$ represents real and imaginary part, respectively.

As the region of interest is discretized into 64×64 pixels, the maximum level of decomposition that can be reached is $L_{\text{max}} = 6$, which means that a single WCSI result is obtained after 6 successive inversions. For CSI, the algorithm stops when the maximum number of iterations is reached. Here, the maximum number

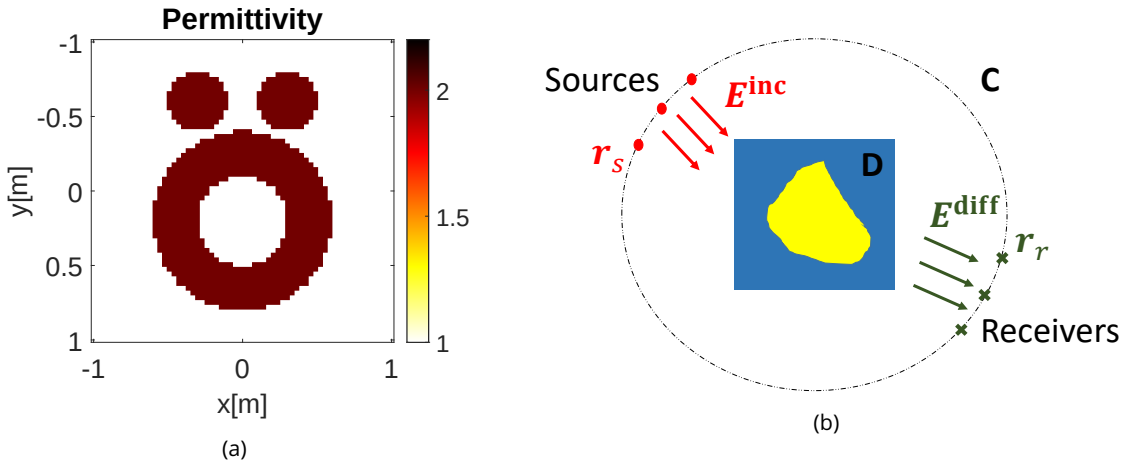

Figure 3.5: Left: Austria model, relative permittivity $\varepsilon(\boldsymbol{r}) = 2$. Right: scattering system.

of iterations is set as 500. For WCSI, 200 iterations are conducted for each inversion.

To compare the reconstruction performance of CSI and WCSI, maps of the normalized contrast error as a function of the number of sources and receivers are given in Fig. 3.6 - 3.7. The number of sources N_s and number of receivers N_r vary from 6 to 48.

Moreover, we compare the reconstruction performance of wavelets with various vanishing moments within the same Daubechies family. Three wavelets are chosen: Haar, db4, and db14.

Fig. 3.6 shows the relative contrast error obtained by CSI and WCSI with three wavelet bases. Here, the Gaussian noise of $20\,\mathrm{dB}$ is added to the scattered fields. From Fig. 3.6, we can observe that both CSI and WCSI with Haar wavelets work well when there is a sufficient number of sensors. However, WCSI achieves better performance as N_s and N_r decrease. The results obtained by WCSI with db4 and db14 wavelets are displayed in Fig. 3.6(c) and Fig. 3.6(d). We can observe that using db4 and db14 wavelets can further improve the reconstruction quality of WCSI. The more the vanishing moments of the wavelet, the higher the order of its filters. With such filters, the energy of the decomposition coefficients becomes more compact and concentrated. Also, the scaling function and wavelet function become smoother, which improves the ability of the wavelet to approximate a signal.

To investigate the robustness of the proposed approach, we further test CSI and WCSI for cases where $10\,\mathrm{dB}$ noise affects the collected data; the results are shown in Fig. 3.7. We can observe from the results that the reconstruction performance of CSI strongly degrades with stronger noises when the number of sensors is reduced. On the contrary, WCSI is more robust to noise, especially with the db4 and db14 wavelets (Fig. 3.7(c) and Fig. 3.7(d)).

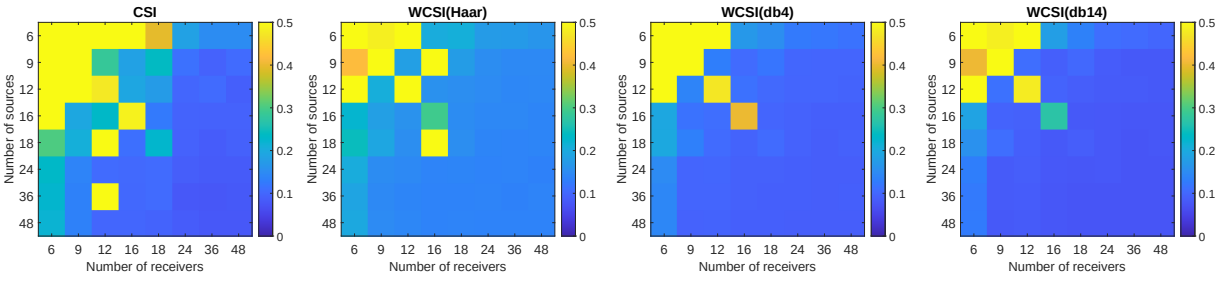

(a) CSI (b) WCSI (Haar) (c) WCSI (dB4) (d) WCSI (db14)

Figure 3.6: Normalized contrast error as a function of N_s and N_r (arbitrary threshold applied at 50%). (a) CSI,(b), (c) and (d) wavelet-based CSI with Haar, db4 and db14 wavelets respectively. Gaussian noise of $20\,\mathrm{dB}$ is added to the scattered fields.

Illustrative results obtained by CSI and WCI applied to cases with different N_s, and N_r are shown in Fig. 3.9 and Fig. 3.10. The relative reconstruction errors are given in Table 3.1. Four combinations of N_s and N_r are considered: $N_s \times N_r = 48 \times 48$, 18×12, 12×9, and 6×18.

In Fig. 3.9, the results are obtained from measurement data affected by a Gaussian noise of $20\,\mathrm{dB}$. The obstacle can be well reconstructed by all methods for the first configuration with enough sensors. As shown in Table 3.1, the relative errors obtained by CSI, WCSI-db4, and WCSI-db14 are less than 10%. Note that the WCSI with Haar wavelet basis has the highest reconstruction error because of the loss of the detail information.

When N_s and N_r decrease, the reconstruction quality of the results obtained by CSI degrades significantly. For the configuration 18×12, CSI cannot obtain meaningful results. For the configuration $N_s \times N_r =$

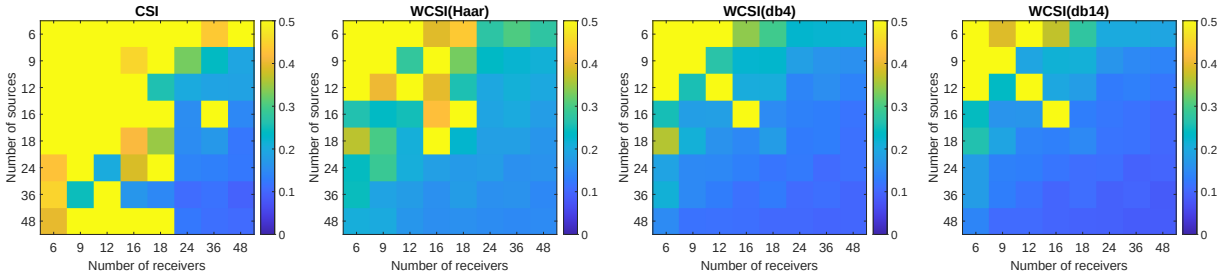

(a) CSI (b) WCSI (Haar) (c) WCSI (dB4) (d) WCSI (db14)

Figure 3.7: Normalized contrast error as a function of N_s and N_r (arbitrary threshold applied at 50%). (a) CSI,(b), (c) and (d) wavelet-based CSI with Haar, db4 and db14 wavelets respectively. Gaussian noise of $10\,\mathrm{dB}$ is added to the scattered fields.

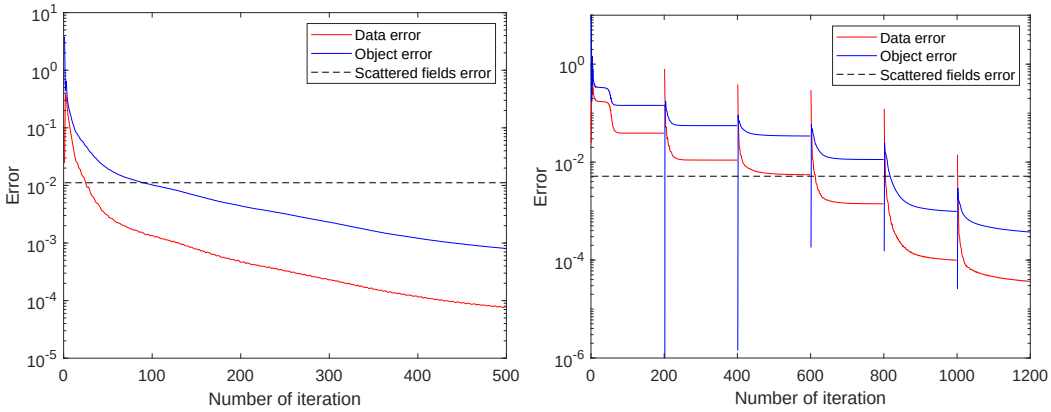

(a) CSI (b) WCSI (db14)

Figure 3.8: Inversion error curves of (a) CSI and (b) WCSI with db14 wavelets. Gaussian noise of $20\,\mathrm{dB}$ is added to the scattered fields.

12×9, the obstacle cannot be well retrieved by CSI; one of the disks and a part of the ring are missing. In comparison, the results obtained by WCI have a much better reconstruction quality. When $N_s \times N_r = 6 \times 18$, the obstacle can be roughly reconstructed by CSI. Still, WCSI performs better than CSI for all three wavelet basis. The db14 basis outperforms the other two bases, as illustrated in Table 3.1.

Fig. 3.8 shows the inversion curves of CSI and WCSI with db14 wavelets where $N_s \times N_r = 6 \times 18$. The data and object error decrease smoothly for CSI. Since WCSI has multiple inversion stages, its error curve decreases again after a period of convergence each time it completes an inversion step. The CPU times for CSI and WCSI are $47.68\,\mathrm{s}$ and $168.18\,\mathrm{s}$, respectively, on an Intel Core i7-6700HQ CPU ($2.60\,\mathrm{GHz}$) with 32 GByte memory. More iterations are required for WCSI, resulting in longer computation time. Further improvement on the stopping criteria of WCSI can reduce the computation burden.

3.4.2 Test with circular dataset

The proposed method is further tested on a synthetically generated circular dataset (Wei *et al.* 2019a). Each sample contains disks of random quantities: number (between 1 and 3), relative permittivity (between 1.5 and 2.5), radius (between $0.15\,\mathrm{m}$ and $0.4\,\mathrm{m}$), and location. The scatterers may overlap and are lossless. The dataset contains 250 samples. The configuration of the scattering system is the same as in the previous section. The number of sensors is of $N_s \times N_r = 6 \times 18$.

Table 3.1: Normalized contrast error with different noise level and different $N_s \times N_r$

Noise (in dB)	$N_s \times N_r$	CSI	WCSI-Haar	WCSI-db4	WCSI-db14
$20\,\mathrm{dB}$	48×48	0.0815	0.1375	0.0891	**0.0766**
	18×12	NA	0.2102	0.1611	**0.1404**
	12×9	0.8040	0.2077	0.1394	**0.1147**
	6×18	0.3951	0.2107	0.1553	**0.1362**
$10\,\mathrm{dB}$	48×48	0.1063	0.1486	0.1011	**0.0874**
	18×12	NA	0.1548	0.1066	**0.0908**
	12×9	1.0863	0.4037	0.2553	**0.2373**
	6×18	0.9818	0.4366	0.2939	**0.2772**

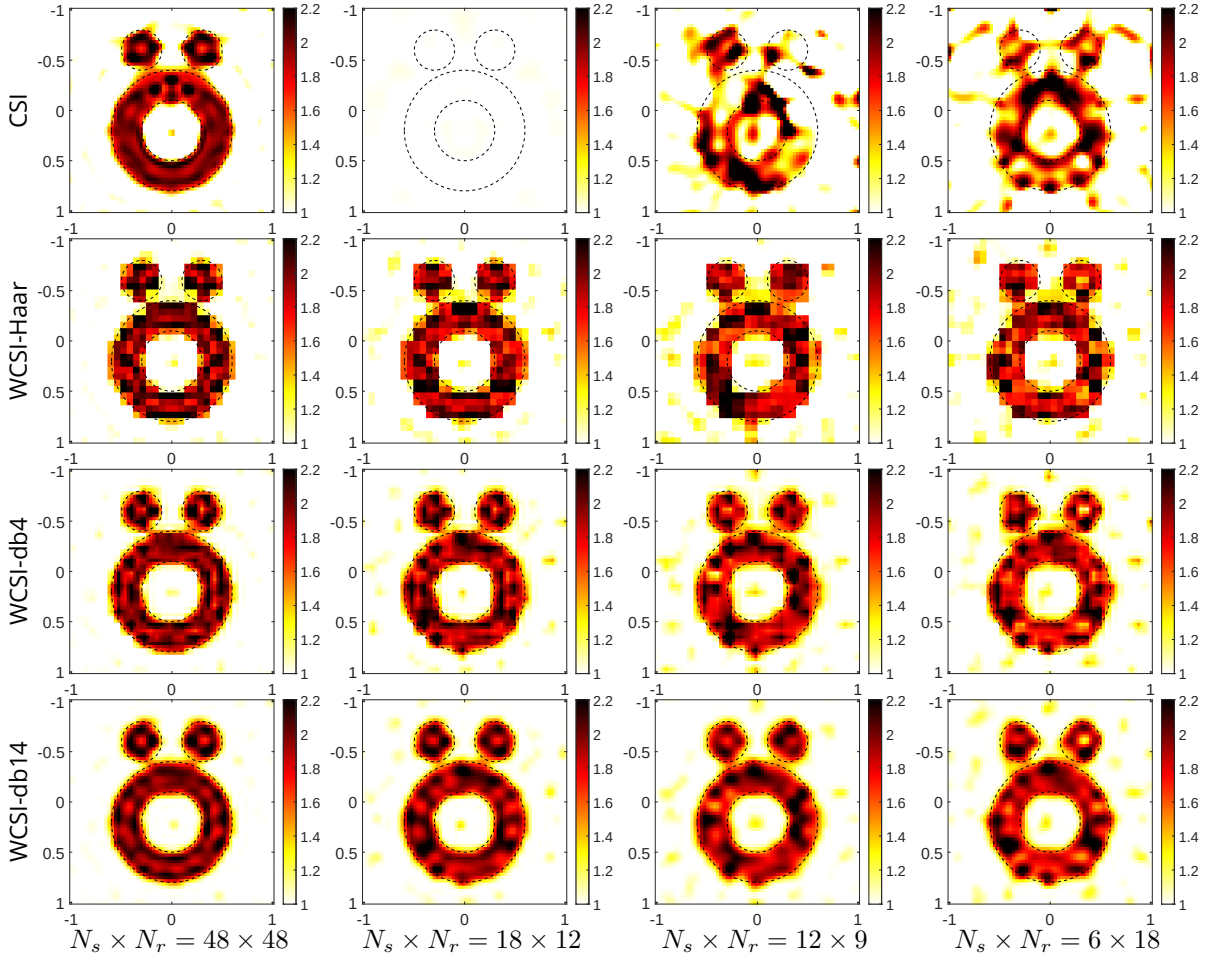

Figure 3.9: Reconstructed $\epsilon(\mathbf{r})$ of "Austria profile" for various combinations of receiver and source numbers. From top to bottom: results of CSI, WCSI with Haar, db4, db14 basis, respectively. Gaussian noise of $20\,\mathrm{dB}$ is added.

CSI and WCSI with db14 basis are tested on 250 samples and the results are given in Fig. 3.11. The mean and variance of Err$(\boldsymbol{\chi})$ obtained by CSI and WCSI-db14 on 250 samples are given in Table 3.2.

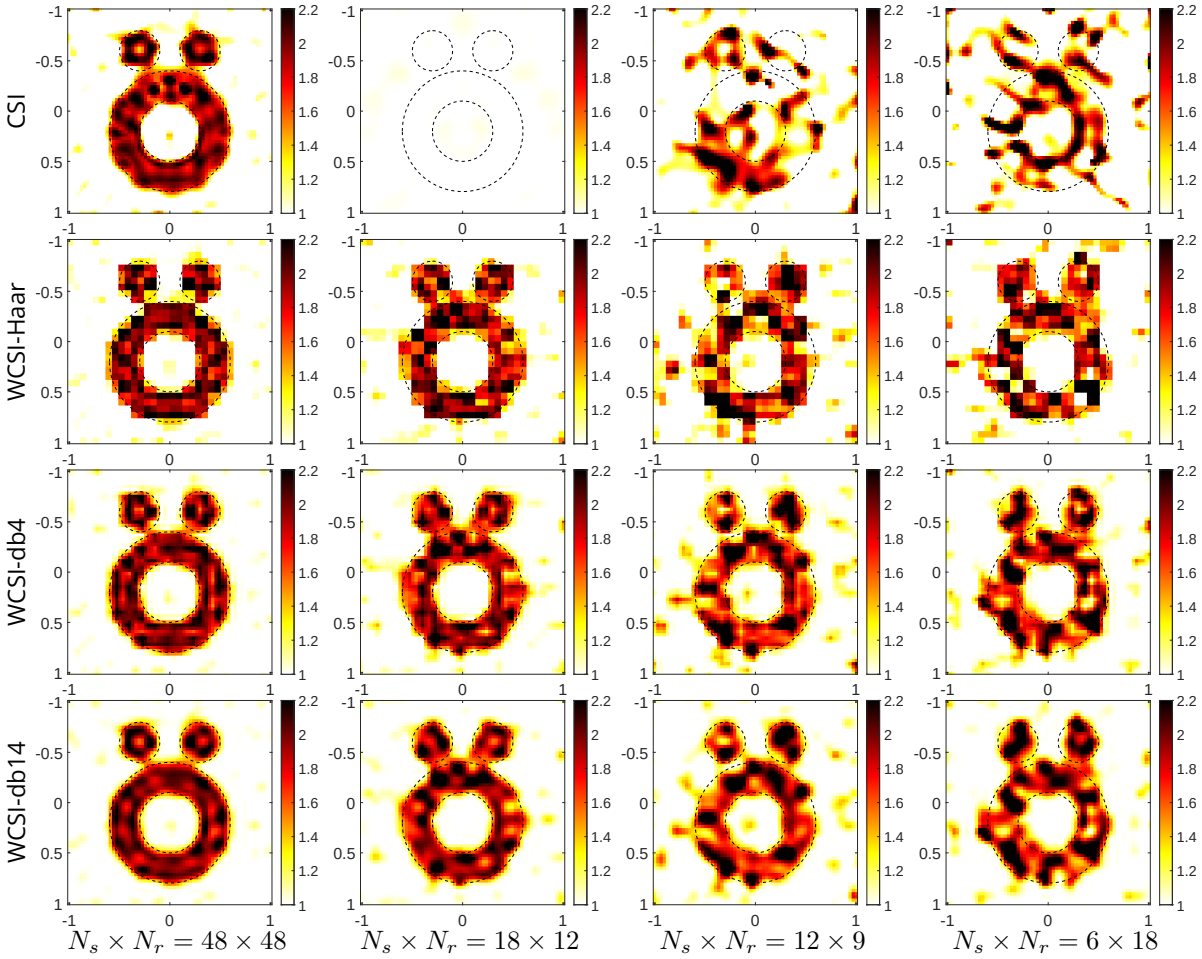

Figure 3.10: Reconstructed $\epsilon(\mathbf{r})$ of "Austria profile" for various combinations of receiver and source numbers. From top to bottom: results of CSI, WCSI with Haar, db4, db14 basis, respectively. Gaussian noise of $10\,\mathrm{dB}$ is added.

3.5 Conclusion

From all the above results, WCSI can improve the quality of reconstruction compared to CSI, especially when the information is reduced. Also, WCSI is more robust than CSI. However, as WCSI has multiple optimization stages corresponding to different decomposition levels, it is more time-consuming than CSI.

Table 3.2: Mean and variance of $\mathrm{Err}(\boldsymbol{\chi})$ on 250 samples.

	CSI	WCSI-db14
Mean	0.5681	**0.1476**
Variance	1.9951	**0.1118**

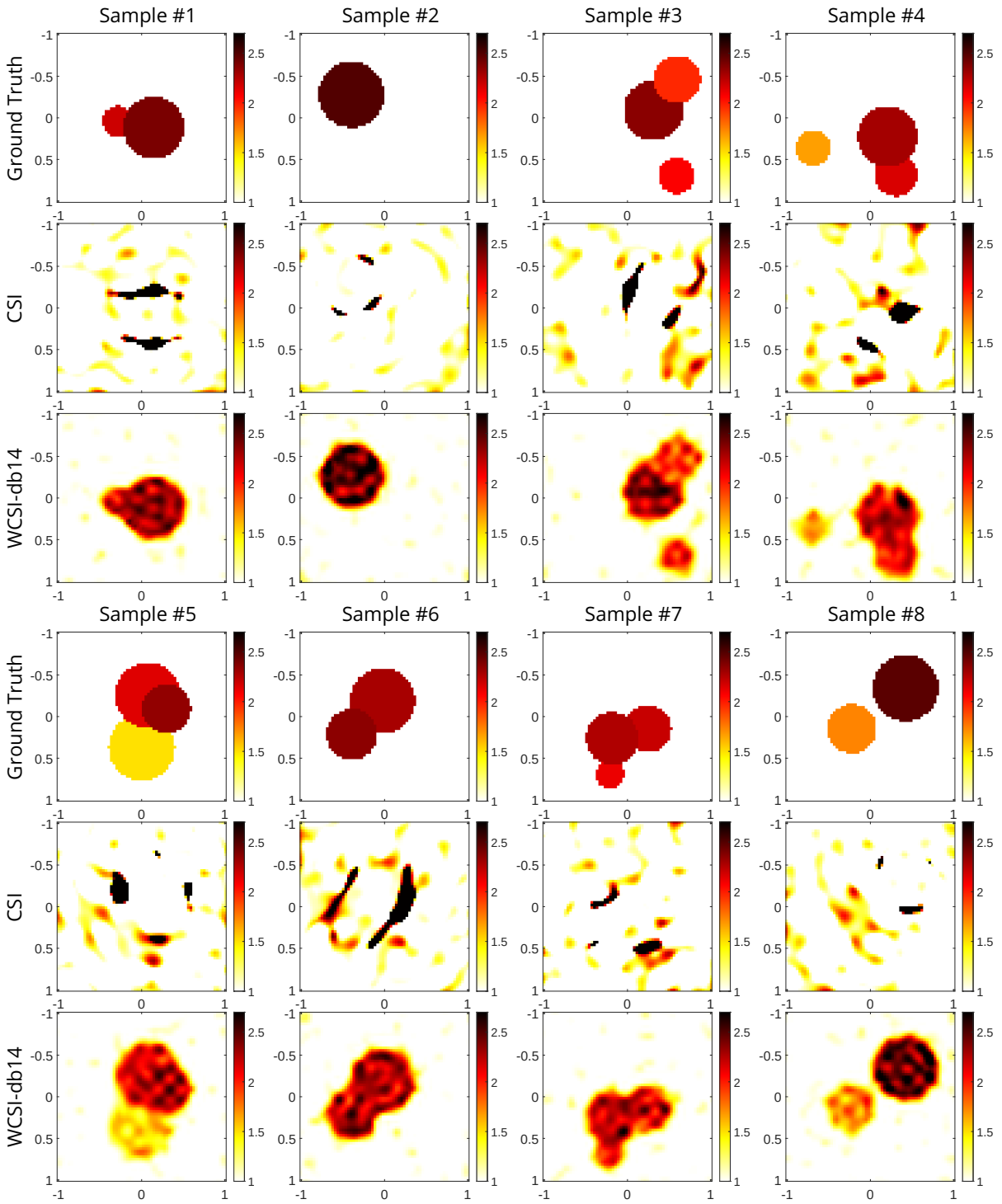

Figure 3.11: Reconstructed $\epsilon(\mathbf{r})$ of 8 samples in circular dataset for $N_s \times N_r = 6 \times 18$. Gaussian noise of $20\,\mathrm{dB}$ is added.

4 Group sparsity penalized Contrast Source Method

One central feature of DWT is that it can provide a sparse representation for a given signal. As mentioned in the previous chapter, the wavelet coefficients can be divided into two main parts: approximation coefficients and detail coefficients. Approximation coefficients which represent the low-frequency components concentrate most of the energy of the signal. Detail coefficients that contain high-frequency components are sparse. In this chapter, a group sparsity penalized CSI method is proposed based on this important property of wavelet detail coefficients.

4.1 Introduction

Due to the strong ill-posedness of ISPs, additional penalty terms are usually needed to regularize the optimization faced. To that intent, various regularization techniques can be applied, such as positivity, total variation (TV), and sparsity, as previously introduced.

Traditional computational methods to tackle ISPs, e.g., CSI and DBIM, have already been combined with various regularization techniques. In (Berg *et al.* 1999), the TV regularization is implemented within the CSI framework as a multiplicative regularization term that leads to a better reconstruction quality and improves robustness to noise. In the DBIM algorithm, Tikhonov regularization (Tikhonov 1963) is employed by default in order to circumvent the instability of the problem. Edge-preserving regularization has also been introduced into ISPs (Lobel *et al.* 1997; Qin *et al.* 2021) to improve the reconstruction quality with respect to noisy corrupted data while preserving the edges of the images. In (Qin *et al.* 2021), Huber regularization is incorporated with the CSI method as a smoothness constraint.

Among different regularization techniques, sparsity is a widely investigated choice.

In (Taşkin *et al.* 2017), the fast iterative shrinkage-thresholding algorithm (FISTA) (Beck *et al.* 2009) is combined with a modified gradient method (MGM) to enforce the sparsity in both non-sparse and sparse domains, where DWT is employed to reach a sparse representation of the unknown.

In (Zaimaga and Lambert 2016), an iterative algorithm incorporating a Tikhonov functional with a sparsity promoting ℓ_1 term is proposed, which enables a sharp reconstruction in the sparse domain.

Iterative shrinkage thresholding algorithm (ISTA) (Beck *et al.* 2009) is implemented within the framework of a boundary integral method in (Desmal *et al.* 2014) to solve the optimization problem with zeroth/first-norm penalty term. The proposed method is proved to be able to yield a sharper and more accurate reconstruction while benefiting from a faster convergence speed.

In (Sanghvi, Bisht, *et al.* 2020), a joint ℓ_1-ℓ_2 norm regularized BIM approach in the wavelet domain is proposed, where appropriate weights adaptively updated at each iteration are allocated to wavelet coefficients at different levels. This scheme enables the performance to be independent of the initial weights. In (Winters *et al.* 2010) and (Azghani, Kosmas, *et al.* 2015), DBIM is incorporated with ℓ_2-ℓ_1 and ℓ_1-ℓ_0 joint norm, respectively, solved by various optimization techniques (Zou *et al.* 2005; Azghani and Marvasti 2013). In

(Bevacqua *et al.* 2017), two sparsity-enhanced approaches within the CSI framework are proposed, the ℓ_1 norm being used as weighted penalty term and constraint. Therein, the stationary wavelet transform (SWT) (Nason *et al.* 1995) is adopted to project the unknown onto a redundant dictionary.

Compressive sensing (CS) based reconstruction algorithms have also been exploited (Oliveri *et al.* 2017; Massa, Rocca, *et al.* 2015). In (Anselmi *et al.* 2015), the commonly used DWT offers a sparse representation of the profile to be reconstructed, then the linearized inverse scattering problem within the first-order Born approximation framework is solved with the Bayesian version CS-based procedure.

The aforementioned state-of-the-art generally uses ℓ_0, ℓ_1, ℓ_2 norms or their combinations to add sparsity constraint to the optimization problem faced with. These vector norms can regularize each element individually regardless of its spatial position and the potential connections between different elements. When the elements are not only sparse but also have potential structure features, the structure information cannot be extracted using these single norms.

Mixed norms (Kowalski 2009) such as $\ell_{2,1}$ or $\ell_{\infty,1}$ are usually employed to impose both sparsity and structural prior information in the optimization problem (Tomassi *et al.* 2015). In (Zaimaga, Fraysse, *et al.* 2017), as the row vectors of the contrast source share a common non-zero support, a two-step sparse recovery process is investigated where the $\ell_{2,1}$ norm is to enforce joint sparsity on the contrast source.

In this chapter, a group sparsity penalized CSI method is proposed, which employs the mixed $\ell_{2,1}$ norm to impose the group sparsity on the contrast in the wavelet domain. Herein, we use the dual-tree complex wavelet transform (DT-$\mathbb{C}$WT) (Selesnick *et al.* 2005) instead of DWT because of a better wavelet tree structure provided by $\mathbb{C}$WT. In the following, we first detail the DT-$\mathbb{C}$WT. Then, the wavelet tree structure (Baraniuk 1999) is introduced, which exists in the wavelet domain, and led by the parent-child relationship (Liu and Moulin 2001) between wavelet coefficients across different scales. Next, the proposed approach is introduced and numerical illustrations are presented.

4.2 Dual-tree Complex Wavelet Transform

The DT-$\mathbb{C}$WT is a relatively recent enhancement of DWT, with some important additional properties. As previously introduced, decomposing a signal $\boldsymbol{X}$ by DWT is to recursively apply the discrete-time low pass and high pass filters, as well as up-sampling and down-sampling operations. DWT has been widely used for signal analysis and reconstruction, which provides a sparse representation of a given signal, and enables multiscale analysis. However, there are four main shortcomings as follows:

1. *Oscillations*: The wavelet transform can provide a sparse representation for a given signal because the wavelets oscillate locally, and large wavelet coefficients are produced when the wavelets overlap a singularity. Otherwise, small wavelet coefficients are produced. However, the wavelet coefficients tend to oscillate in a positive and negative manner around the singularities, which makes the wavelet-based processing more complicated.
2. *Shift variance*: The wavelet coefficients of a given signal are sensitive to translations of the input signal. A small shift of the input signal results in an obvious change in the wavelet domain, i.e., the distribution of energy between DWT coefficients at different scales. This property also complicates the wavelet-domain signal processing.
3. *Aliasing*: Substantial aliasing appears during the decomposition process, and the inverse DWT cancels this aliasing. The time-domain signal can be perfectly reconstructed from its wavelet coeffi-

cients thanks to the specially designed decomposition and reconstruction filter banks. However, any wavelet coefficients processing,, e.g. thresholding, filtering, and quantization, upset the balance between the direct and inverse transforms, resulting in artifacts in the reconstruction.

4. *Lack of directionality*: When employing DWT to decompose a 2-D image, the filters and down-sampling operations are applied separately along row and column directions and four subimages can be obtained: LL, LH, HL and HH. The subbands LH, HL and HH contain detail information in three directions. However, this weakens the detail information in other directions, making it difficult to represent non-horizontal or non-vertical singular features. This drawback greatly complicates the modeling and processing of geometric image features such as ridges and edges.

Inspired by the FT based on complex-valued oscillating sinusoids, the DT-$\mathbb{C}$WT was introduced by Kingsbury in 1998 (Selesnick *et al.* 2005). Unlike the conventional DWT which uses real-valued oscillating wavelets, the DT-$\mathbb{C}$WT uses complex-valued scaling function and wavelet

$$\Phi_c(\boldsymbol{r}) = \Phi_r(\boldsymbol{r}) + j\Phi_i(\boldsymbol{r}) \tag{4.1}$$

$$\Psi_c(\boldsymbol{r}) = \Psi_r(\boldsymbol{r}) + j\Psi_i(\boldsymbol{r}) \tag{4.2}$$

Projecting the signal onto $2^{j/2}\Psi(2^j\boldsymbol{r} - k)$, we can obtain the complex wavelet coefficients

$$W_c(j,k) = W_r(j,k) + jW_i(j,k) \tag{4.3}$$

If $\Psi_r(\boldsymbol{r})$ and $\Psi_i(\boldsymbol{r})$ form a Hilbert transform pair, then $\Psi_c(\boldsymbol{r})$ is an analytic signal. The complex scaling function is defined similarly. The complex wavelet and scaling functions are expected to be as close as possible to analytic in order to perfectly overcome the four DWT shortcomings. The DT-$\mathbb{C}$WT uses a dual-tree structure to obtain the real and imaginary parts of the complex wavelet coefficients. Two real DWTs are employed and each tree corresponds to a DWT. The first DWT gives the real part of the complex coefficients and the second one gives the imaginary part.

Fig. 4.1(a) and 4.1(b) show the analysis and synthesis filter banks of the DT-$\mathbb{C}$WT. $h_0(n)$, $h_1(n)$ denote the low pass/high pass filter pair for the upper filter bank (real branch). $g_0(n)$, $g_1(n)$ denote the low pass/high pass filter pair for the lower filter bank (imaginary branch). The wavelet functions $\Psi_h(\boldsymbol{r})$ and $\Psi_g(\boldsymbol{r})$ associated with the two DWTs satisfy Equation (4.2), and $\Psi_g(\boldsymbol{r})$ is designed to be approximately the Hilbert transform of $\Psi_h(\boldsymbol{r})$ so that the corresponding complex wavelet $\Psi_c(\boldsymbol{r})$ is approximately analytic. The inverse of DT-$\mathbb{C}$WT is also the synthesis of two real DWTs, which correspond to the inverse of the two real DWTs used in the forward transform. $\tilde{g}(n)$ is the inverse of $g(n)$ and $\tilde{h}(n)$ is the inverse of $h(n)$. It should be noted that the implementation of the DT-$\mathbb{C}$WT requires that the filters used in the first stage should be different from the succeeding stages, in order to make the filter banks approximately analytic.

4.2.1 Comparison of 2-D DWT and 2-D DT-$\mathbb{C}$WT

As previously introduced, 2-D DWT can produce three sub-bands which contain detail information: LH, HL and HH, obtained by three wavelets characterized by

$$\Psi_{\mathsf{LH}}(x,y) = \Phi(x)\Psi(y) \tag{4.4}$$

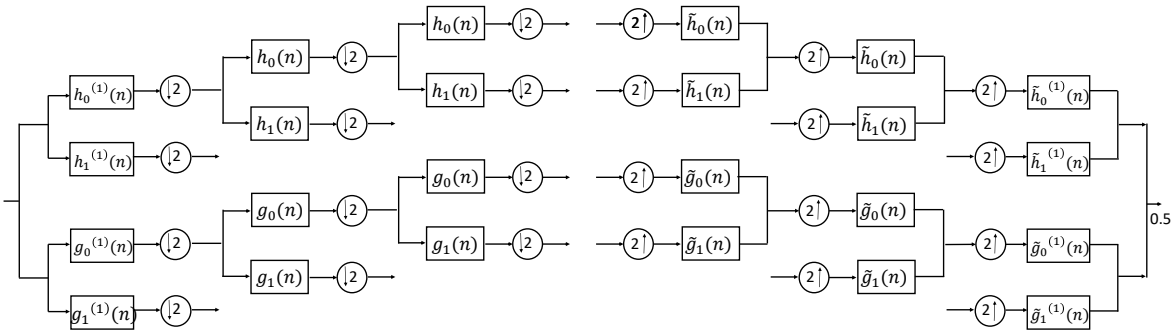

(a) Analysis filter bank (b) Synthesis filter bank

Figure 4.1: 1-D DT-$\mathbb{C}$WT. $h_0^{(1)}(n)$ is the filter used for the first stage, and $h_0(n)$ is for the succeeding stages. The implementation of the DT-$\mathbb{C}$WT requires that the first stage of the filter banks be different from the succeeding stages.

$$\Psi_{\mathsf{HL}}(x,y) = \Psi(x)\Phi(y) \tag{4.5}$$

$$\Psi_{\mathsf{HH}}(x,y) = \Psi(x)\Psi(y) \tag{4.6}$$

The LH wavelet is the product of the scaling function Φ along the x-direction and the wavelet function Ψ along the y-direction. The HL and HH wavelets are similarly defined. Fig. 4.2 shows the three wavelets. We can observe that the LH and HL wavelets are oriented vertically and horizontally. However, a checkerboard artifact appears in the HH wavelet, which is due to the use of real-valued separate filters. This makes the wavelet unable to distinguish $+45^\circ$ and -45° orientations.

Differently from the 2-D DWT, the 2-D DT-$\mathbb{C}$WT produces six sub-bands for both real and imaginary parts. The transformation result is four times more expansive than that of DWT. The six wavelets for the real part are defined in the following way

$$\Psi_i(x,y) = \frac{1}{\sqrt{2}}\left(\Psi_{1,i}(x,y) - \Psi_{2,i}(x,y)\right) \tag{4.7}$$

$$\Psi_{i+3}(x,y) = \frac{1}{\sqrt{2}}(\Psi_{1,i}(x,y) - \Psi_{2,i}(x,y)) \tag{4.8}$$

where $i = 1,2,3$, $\frac{1}{\sqrt{2}}$ is the normalization factor to make the sum/difference operation constitutes an orthonormal operation. The wavelet bases are defined in the same manner as equations (4.4)-(4.6)

$$\Psi_{1,1}(x,y) = \Phi_h(x)\Psi_h(y), \quad \Psi_{2,1}(x,y) = \Phi_g(x)\Psi_g(y) \tag{4.9}$$

$$\Psi_{1,2}(x,y) = \Psi_h(x)\Phi_h(y), \quad \Psi_{2,2}(x,y) = \Psi_g(x)\Phi_g(y) \tag{4.10}$$

$$\Psi_{1,3}(x,y) = \Psi_h(x)\Psi_h(y), \quad \Psi_{2,3}(x,y) = \Psi_g(x)\Psi_g(y) \tag{4.11}$$

Likewise, the six wavelets for the imaginary parts are defined as

$$\Psi_i(x,y) = \frac{1}{\sqrt{2}}\left(\Psi_{3,i}(x,y) - \Psi_{4,i}(x,y)\right) \tag{4.12}$$

$$\Psi_{i+3}(x,y) = \frac{1}{\sqrt{2}}(\Psi_{3,i}(x,y) - \Psi_{4,i}(x,y)) \tag{4.13}$$

where $i = 1, 2, 3$ and the wavelet bases are defined as

$$\Psi_{3,1}(x,y) = \Phi_g(x)\Psi_h(y), \quad \Psi_{4,1}(x,y) = \Phi_h(x)\Psi_g(y) \tag{4.14}$$

$$\Psi_{3,2}(x,y) = \Psi_g(x)\Phi_h(y), \quad \Psi_{4,2}(x,y) = \Psi_h(x)\Phi_g(y) \tag{4.15}$$

$$\Psi_{3,3}(x,y) = \Psi_g(x)\Psi_h(y), \quad \Psi_{4,3}(x,y) = \Psi_h(x)\Psi_g(y) \tag{4.16}$$

With the twelve oriented wavelets defined above for the real part and imaginary part, a set of complex wavelets can be constructed. Fig. 4.3 illustrates the twelve wavelets, the six wavelets displayed on the first (second) row are interpreted as the real (imaginary) part of a set of six complex wavelets.

2-D DT-$\mathbb{C}$WT has good shift invariance and directional selectivity, which are two key advantages over DWT. The good directional selectivity allows capturing more oriented singularities of an image, without the presence of the checkerboard artifact in the diagonal wavelet of DWT. The near-shift invariance also brings a key property for our work, which will be further introduced in the next part. Moreover, although the 2-D DT-$\mathbb{C}$WT produces wavelet coefficients that are four times more expansive than that of DWT, its implementation is still very efficient since only additions and subtractions for respective sub-bands of all DWTs are required.

Fig. 4.4(a) is a spatial profile to be decomposed. Fig. 4.4(b) shows its wavelet coefficients obtained by conventional 2-D DWT with db4 wavelet basis. In Fig. 4.5, wavelet coefficients obtained by 2-D DT-$\mathbb{C}$WT are displayed. Farras filters (Abdelnour *et al.* 2004) are used for the first stage and Kingsbury Q-shift 6-tap filters (Kingsbury 2000) for the following stages. As previously mentioned, the result of DT-$\mathbb{C}$WT is four times more expansive than the result of DWT.

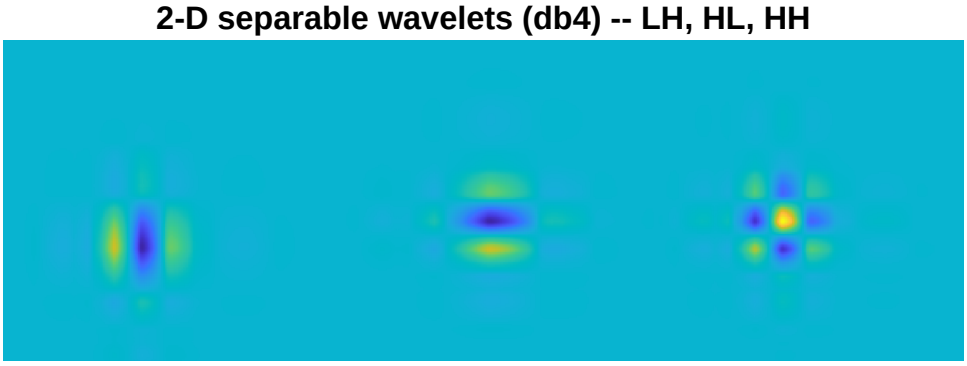

Figure 4.2: db4 wavelets (LH, HL, HH) associated with the 2-D DWT in the space domain. Level of decomposition is 5.

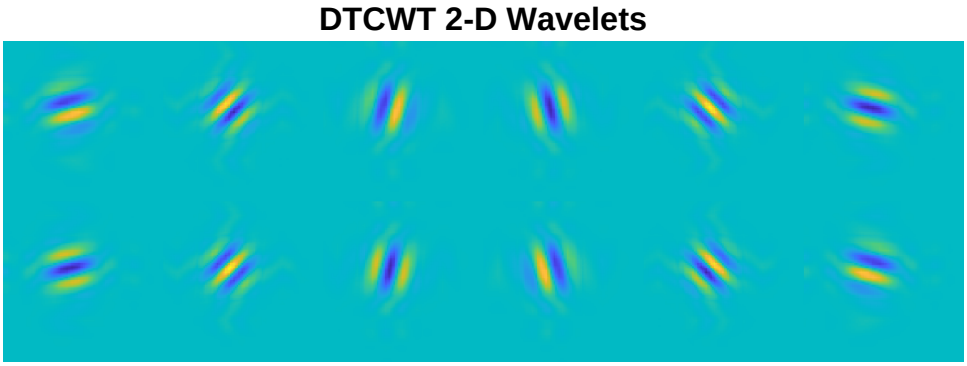

Figure 4.3: Typical wavelets associated with the oriented 2-D DT-$\mathbb{C}$WT in the space domain.

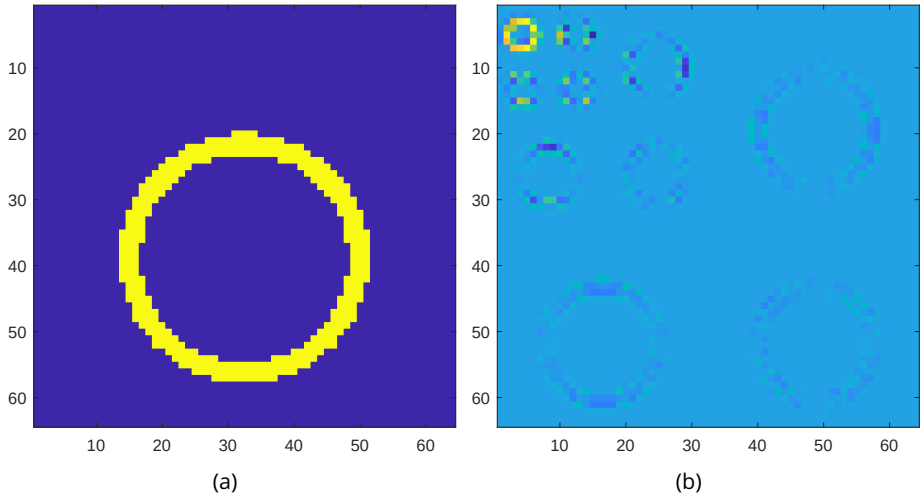

Figure 4.4: (a): A "circle" example in spatial domain. (b): Wavelet coefficients obtained by 2-D DWT using db4 wavelet basis. Decomposition level $L = 3$.

4.2.2 Wavelet quadtree structure

The wavelet transform has several attractive characteristics (Mallat 2008):

- **Edge detection** and **sparsity**: the wavelet transform is an efficient tool to capture singularities of signals, in 2-D cases, the extraction of image features like ridges and edges. As wavelets oscillate locally, only wavelets overlapping a singularity have large wavelet coefficients and all other coefficients are small. This is also the key to the sparsity of wavelet coefficients because the edge is only a small part of the image content.
- **Multiscale analysis**: the wavelet transform allows an image to be analyzed at different resolution scales since the transformation domain has a nested set of scales.

These attractive characteristics can be regarded as the *primary properties*, from which a *secondary property* can be derived:

- **Persistence**: the wavelet transform naturally yields a dependent quadtree structure. This dependency tends to propagate across different scales. Consequently, wavelet coefficients across different scales can be regarded as statistically dependent. If a wavelet coefficient is large/small, the coefficients at the same orientation in the next adjacent scale are likely to be large/small. This is the

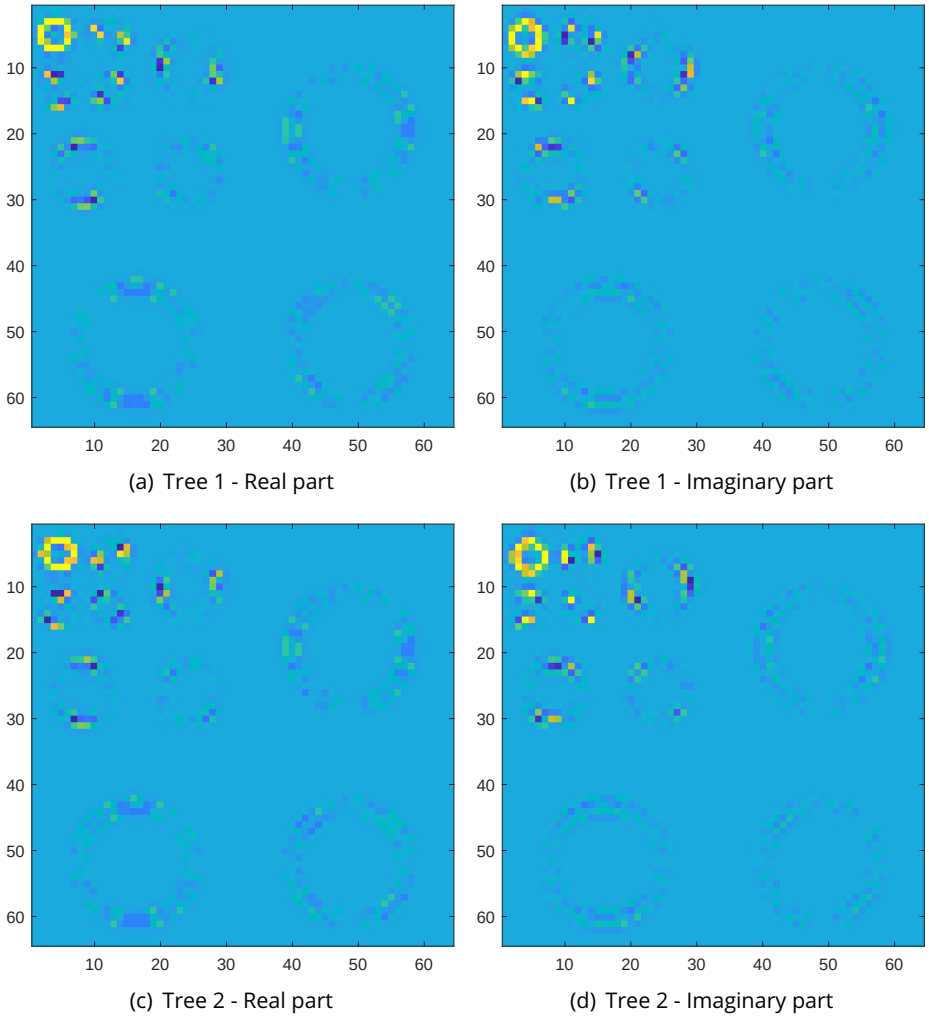

(a) Tree 1 - Real part (b) Tree 1 - Imaginary part

(c) Tree 2 - Real part (d) Tree 2 - Imaginary part

Figure 4.5: Wavelet coefficients obtained by oriented 2-D DT-$\mathbb{C}$WT. Farras filters are used for the first stage and Kingsbury Q-shift after. Decomposition level $L = 3$.

so-called *parent-child relationship*. (Crouse *et al.* 1998).

This secondary property has been widely exploited in the statistical signal processing community (Crouse *et al.* 1998; Romberg *et al.* 2001), generally modeled as a *hidden Markov tree* (HMT).

Fig. 4.6(a) shows the 2-D DWT result with the dependency between wavelet coefficients visualized. This dependency can be modeled as a set of trees. Denote three sub-bands of detail coefficients at level L as $\{HL, LH, HH\}_L$. Each coefficient in $\{HL, LH, HH\}_L$ possesses four *children* coefficients at the same orientation in $\{HL, LH, HH\}_{L-1}$. The wavelet coefficient from the coarser scale of decomposition can be regarded as the *parent* of its *children* coefficients in the next scale. This leads to a hierarchical quadtree structure. More precisely, for a detail coefficient located at (x, y) at the decomposition level L, its four children will be in the next decomposition level $L-1$, located respectively at $(2x-1, 2y-1)$, $(2x-1, 2y)$, $(2x, 2y-1)$ and $(2x, 2y)$, occupying a 2×2 region. The arrows in Fig. 4.6(a) identify the parent-children dependencies.

An example of a wavelet quadtree is given in Fig. 4.6(b). Consider that the node 1 is a coefficient in $\{HL, LH, HH\}_3$ and make it a root node. A quadtree can be constructed based on this root node, where

its four *children* are placed in the second layers. The four *children* coefficients lead to sixteen "grandchildren" of the root node in the third layer. Emphasis should be put on the *parent-child relationship* led by the wavelet quadtree structure. Since dependency relations exist between wavelet coefficients, i.e., if a *parent* coefficient is negligible, then its *children* are also generally negligible. The wavelet coefficients can therefore be divided into different groups, based on which the group sparsity technique can be applied.

Nevertheless, the 2-D DWT suffers from a strong shift-variance, which greatly affects the persistence property of wavelet coefficients. It has been proved in (Choi *et al.* 2000) that the near shift invariance of the oriented DT-$\mathbb{C}$WT leads to better persistence of the magnitudes around the edgy regions, which ensures stronger dependence in inter-scale adjacent coefficients. In other words, the oriented DT-$\mathbb{C}$WT strengthens the *parent-child relationship*, which is the key to implementing group-sparsity-based technique.

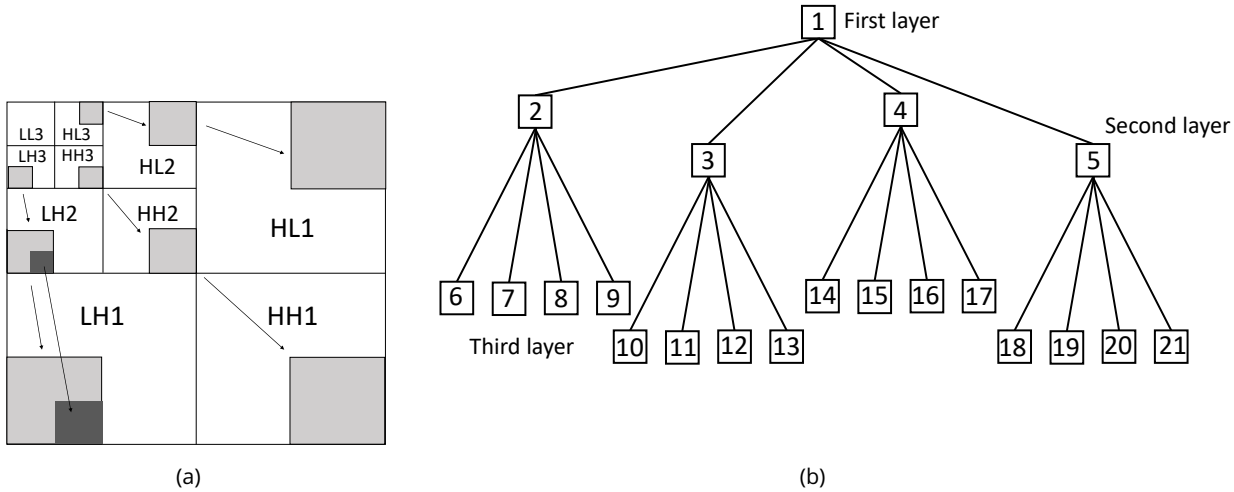

Figure 4.6: (a): Wavelet quadtree structure of transformed 2-D image. Level of decomposition $L = 3$. (b): Example of wavelet quadtree structure.

4.3 Sparsity inducing norms

In the previous section, the DT-$\mathbb{C}$WT and the wavelet quadtree structure are introduced, which are two key points to achieve the group sparsity penalized CSI method. In this section, the sparsity regularization terms that enable the incorporation of prior information into optimization problems are sketched.

4.3.1 Sparsity through single norm

A vector x of dimension M can be considered as *sparse* if most of its elements are zero, or almost zero. For an optimization problem referring to

$$x = \arg\min_{x} \mathcal{F} \tag{4.17}$$

the sparsity can be directly achieved by adding a regularization term that penalizes the number of non-zero elements of the vector, in the form of the vector norm $\|x\|_q$. Thus the combinatorial optimization arises

$$x = \arg\min_{x} \left\{ \mathcal{F} + \|x\|_q \right\} \tag{4.18}$$

To impose sparsity as the prior information into the optimization problem, there are several choices of

q:

- When $q = 0$, the regularization term is the ℓ_0 norm, defined as $\|x\|_0 = \#\{i = 1, \ldots, M | x_i \neq 0\}$, which counts the non-zero elements of the vector. However, solving optimization problems with the non-convex ℓ_0 norm is as difficult as trying out all possible non-zeros supports of coefficients. To avoid this NP-hard problem, a tractable approach to solving the ℓ_0 minimization problem is to replace it with a reasonable and convex approximation.
- When $q = 1$, the regularization term is the ℓ_1 norm, which is a natural approximation of ℓ_0 norm, defined as $\|x\|_1 = \sum_{i=1}^{M} |x_i|$. Unlike ℓ_0 norm, the optimization of ℓ_1 norm is a convex problem and can be solved efficiently (Boyd *et al.* 2004).

4.3.2 Sparsity through mixed norm

In the previous formulation with ℓ_1 norm, every element of the vector is regarded as independent from the others. In some situations, however, the elements of a vector share the same support, or dependency relationships exist between different elements, which allows them to be divided into subgroups. It is then easy to see that the elements within a given group can be selected or deleted simultaneously, benefiting from this prior structure information. A regularization norm exploiting such structural prior information proposed in (Yuan *et al.* 2006) has the following form

$$\|x_g\|_{2,1} = \sum_{i=1}^{s} \|x_{g_i}\|_2 \tag{4.19}$$

g represents the subgroups, x_{g_i} are the sub-vectors of x indexed by g_i, $i = 1, \ldots, s$ where s is the number of subgroups. This is the so-called mixed $\ell_{2,1}$ norm, acting like an ℓ_1 norm on the vector $\|x_{g_i}\|_2$. It should be noted that the mixed $\ell_{2,1}$ norm does not yield sparsity within a group. That is, if most of the elements in a group are non-zero, then they will all be imposed to be non-zero. $\ell_{\infty,1}$ norm is also a popular one to induce group sparsity. In this work, the $\ell_{2,1}$ is used.

4.3.3 Solution to optimization problems with regularization terms

To solve a non-constrained optimization problem where the cost function to minimize is differentiable, a common way is to use the iterative gradient descent method. At each iteration, x is updated according to

$$x^k = x^{k-1} - t_k \nabla \mathcal{F}(x^{k-1}) \tag{4.20}$$

k represents the k-th iteration, t_k is the step size and $\nabla \mathcal{F}(x^{k-1})$ is the gradient of $\mathcal{F}$ at the point $k-1$. However, due to the presence of the regularization norm, the whole cost function becomes non-differentiable, so the existence of the gradient is not always guaranteed.

Subgradient method One possible manner to deal with this kind of optimization problem is to use the subgradient technique (Shor 1985), which allows approximating the gradient of the non-differentiable function at non-derivable points. For a given function $\mathcal{F}$, $\forall y$, g is the subgradient of $\mathcal{F}$ at point x if it satisfies

$$\mathcal{F}(y) \geq \mathcal{F}(x) + g^T(y - x) \tag{4.21}$$

Convex functions always have sub-gradients. Provided that the left-hand derivative of a convex function at point x_0 is

$$a = \lim_{x \to x_0^-} \frac{f(x) - f(x^0)}{x - x^0} \tag{4.22}$$

and the right-hand derivative is

$$b = \lim_{x \to x_0^+} \frac{f(x) - f(x^0)}{x - x^0} \tag{4.23}$$

the subgradient of the convex function can be any value in $[a, b]$. Non-convex functions do not necessarily have sub-gradients even if they are differentiable. However, the convergence rate of the subgradient method is very slow.

Proximal gradient descent method What one adopts in the present work is another well-known approach called the proximal gradient descent method (Rockafellar 1970). Now consider the function can be decomposed into two functions as follows

$$\mathcal{F}(x) = \mathcal{G}(x) + \mathcal{H}(x) \tag{4.24}$$

where $\mathcal{G}$ is convex, differentiable, $\mathcal{H}$ is convex and not necessarily differentiable. For the optimization problem

$$x = \arg\min_x \{\mathcal{G}(x) + \mathcal{H}(x)\} \tag{4.25}$$

x can be updated at iteration k according to

$$x^k = \text{prox}_{t\mathcal{H}(.)}\left(x^{k-1} - t_k \nabla \mathcal{G}\left(x^{k-1}\right)\right) \tag{4.26}$$

wherein t_k is the descent step size at k-th iteration. The *proximal operator* of $\mathcal{H}(.)$ at point x has the following expression and it is a function of $\mathcal{H}$ and t

$$\text{prox}_{t\mathcal{H}(.)}(t) = \arg\min_x \frac{1}{2t}\|x - t\|_2^2 + \mathcal{H}(x) \tag{4.27}$$

The key advantages of the proximal gradient descent method are as follows:

- Proximal operator can be computed analytically for plenty of widely used $\mathcal{H}$ functions. For example, when $\mathcal{H}(x) = \|x\|_1$, the corresponding $\text{prox}_{t\mathcal{H}(.)}(.)$ is the soft-thresholding operator.
- Proximal operator only depends on $\mathcal{H}$, this means that $\mathcal{G}$ can be a complicated function.

4.3.4 Solution to $\ell_{2,1}$ norm penalized optimization problems

When $\mathcal{H}(x) = \|x\|_{2,1}$, this is the so-called sparse group Lasso (Simon *et al.* 2013) —least absolute shrinkage and selection operator— problem, and the solution depends on the grouping methods.

For non-overlapping groups Non-overlapping means that each element belongs to only one group. Fig. 4.7(a) displays an example of non-overlapping groups, where each row of the 2-D matrix represents a subgroup.

To tackle the non-overlapping group Lasso problem where the $\ell_{2,1}$ norm is applied, the proximal gradient descent method is usually employed because the proximal operator of $\ell_{2,1}$ has a closed-form solution (Kowalski 2009) with λ the hyperparameter linked to the regularization term

$$x'_{g_i} = x_{g_i} \times \left(1 - \frac{\lambda}{\|x_{g_i}\|_2}\right)_+, \ \forall i \tag{4.28}$$

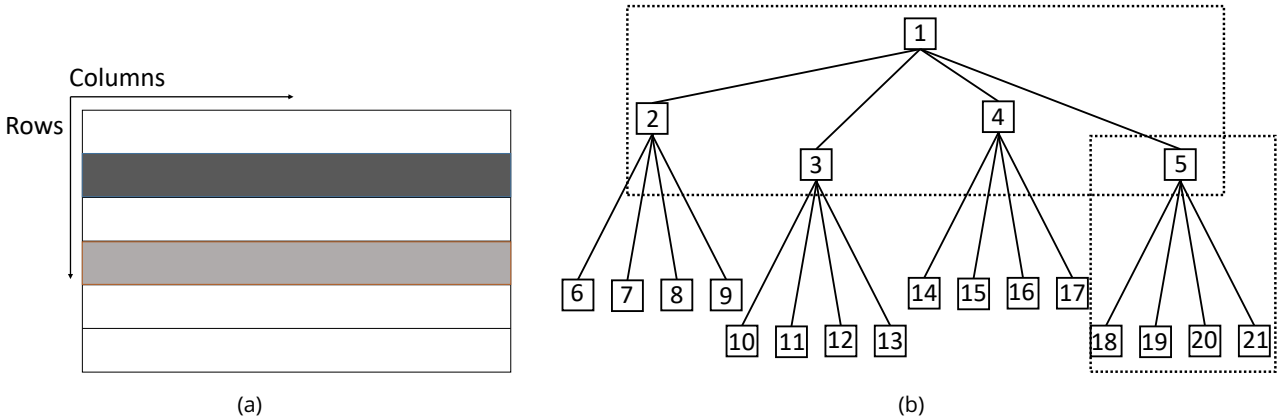

Figure 4.7: (a): Non-overlapping grouping arrangement. (b): Overlapping grouping arrangement.

For overlapping groups In overlapping group cases, an element can appear in different subgroups. For instance, the *parent-child relationship* leads to a hierarchical tree structure, which is a typical overlapping grouping arrangement. Take the example of the wavelet quadtree structure displayed in Fig. 4.7(b), the nodes $\{1, 2, 3, 4, 5\}$ constitute a subgroup, and the nodes $\{5, 18, 19, 20, 21\}$ form another subgroup. Here, the node 5 appears in two subgroups.

For the overlapping group Lasso problem, where an element can appear in different subgroups, the problem becomes more complicated since the standard group Lasso optimization strategies cannot be used directly.

Much attention has been paid to exploiting overlapping situations, especially those with a hierarchical tree structure. In (Liu and Ye 2010), an approach to deal with tree-structured group Lasso problems is offered, in which the Moreau-Yosida regularization is employed, and its analytical solution is given. In (Jenatton *et al.* 2011), the dual approach is used, and the proximal operator of the norm associated with overlapping hierarchical groups proved to be exactly computable, which can be regarded as the composition of elementary proximal operators.

The strategies for overlapping group optimization problems mentioned above are complicated to implement. A smart way to transform the overlapping group Lasso problems into non-overlapping ones is proposed in (Jacob *et al.* 2009; Rao *et al.* 2011; Chen and Huang 2014). The authors propose the so-called replication strategies, which consist in decoupling the overlapping groups from each other by replicating the elements appearing repeatedly. For example, by applying the replication strategy, the two aforementioned subgroups $\{1, 2, 3, 4, 5\}$ and $\{5, 18, 19, 20, 21\}$ are decoupled, and the node 5 is replicated. Then, the groups become $\{1, 2, 3, 4, 5_a\}$ and $\{5_b, 18, 19, 20, 21\}$. The decoupled groups can tackle this problem using the same proximal operator as in the non-overlapping case.

4.4 Group sparsity penalized CSI

In this section, the proposed group sparsity penalized CSI approach is sketched.

4.4.1 $\ell_{2,1}$ norm regularized cost function

Here, the contrast function χ is decomposed by the 2-D oriented DT-$\mathbb{C}$WT. Owing to the two properties of wavelet coefficients: sparsity and persistence, the group sparsity regularization is imposed in the cost function of the CSI method in the wavelet domain.

Take the cost function of CSI in the wavelet domain

$$F^{\mathcal{W}}(\boldsymbol{J}_i, \boldsymbol{\beta}) = \frac{\sum_{i=1}^{N_s} \|\boldsymbol{\rho_i}\|^2}{\sum_{i=1}^{N_s} \|\boldsymbol{\xi}_i\|^2} + \frac{\sum_{i=1}^{N_s} \left\|\mathcal{W}^*\{\boldsymbol{\beta}\}(\boldsymbol{E}_i^{\text{inc}} + \boldsymbol{G}_D\boldsymbol{J}_i) - \boldsymbol{J}_i\right\|^2}{\sum_{i=1}^{N_s} \|\mathcal{W}\{\mathcal{W}^*\{\boldsymbol{\beta}\}\boldsymbol{E}_i^{\text{inc}}\}\|^2} \tag{4.29}$$

Here, $\mathcal{W}\{\boldsymbol{.}\}$ represents the 2-D oriented DT-$\mathbb{C}$WT instead of conventional 2-D DWT, and $\mathcal{W}^*\{\boldsymbol{.}\}$ is the inverse transform. Employing the DT-$\mathbb{C}$WT, the contrast $\boldsymbol{\chi}$ is decomposed in the complex wavelet domain at each iteration. $\boldsymbol{\beta} = \mathcal{W}\{\boldsymbol{\chi}\}$ are the complex wavelet coefficients of the contrast function.

Now, one adds the group sparsity regularization term to the cost function (4.29), i.e., the $\ell_{2,1}$ norm, and the cost function becomes

$$F^{\mathcal{W}}(\boldsymbol{J}_i, \boldsymbol{\beta}) = \frac{\sum_{i=1}^{N_s} \|\boldsymbol{\rho_i}\|^2}{\sum_{i=1}^{N_s} \|\boldsymbol{\xi}_i\|^2} + \frac{\sum_{i=1}^{N_s} \|\mathcal{W}^*\{\boldsymbol{\beta}\}(\boldsymbol{E}_i^{\text{inc}} + \boldsymbol{G}_D\boldsymbol{J}_i) - \boldsymbol{J}_i\|^2}{\sum_{i=1}^{N_s} \|\mathcal{W}\{\mathcal{W}^*\{\boldsymbol{\beta}\}\boldsymbol{E}_i^{\text{inc}}\}\|^2} + \boldsymbol{\Lambda}\|\boldsymbol{\beta}_g\|_{2,1} \tag{4.30}$$

Subgroups can be constituted based on the dependency between *parent* and *children* coefficients. Thus, the group sparsity regularization can be applied to the contrast in the wavelet domain, which promotes the persistence of magnitudes of wavelet coefficients across scales. If most of the coefficients in a subgroup are almost zero or nearly zero, then the whole group will be regularized by the sparsity constraint.

4.4.2 Grouping arrangement

To properly optimize the $\ell_{2,1}$ norm regularized cost function, a key issue is to clarify the grouping arrangement. Three grouping choices are proposed. An example of wavelet quadtree structure is given in Fig. 4.8. Given that the elements surrounded by boxes of the same color belong to the same group, three groups appear:

- $\{1, 5\}$ (in red)
- $\{1, 2, 6\}$ (in blue)
- $\{1, 2, 3, 4, 5\}$ (in yellow)

The three subgroups represent three ways to group the wavelet coefficients.

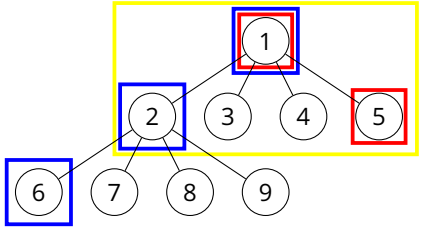

Figure 4.8: Grouping arrangement of wavelet coefficients.

For a wavelet coefficient A, the subgroups can be constituted as follows:

- $\{A,$ *parent* of $A\}$ (in red)
- $\{A,$ all *ancestors* of $A\}$ (in blue)
- $\{A,$ all *children* of $A\}$ (in yellow)

All three grouping choices form overlapping subgroups. Thus, the regularized cost function must be tackled with specific strategies. Herein, one adopts the replication approach proposed in (Chen and Huang 2014). By replicating the crossing elements, the aforementioned subgroups become

- $\{1_a, 5_a\}$ (in red)
- $\{1_b, 2_a, 6\}$ (in blue)
- $\{1_c, 2_b, 3, 4, 5_b\}$ (in yellow)

The nodes $(1_a, 1_b, 1_c)$, $(2_a, 2_b)$, and $(5_a, 5_b)$ are replications of nodes $1, 2$ and 5, respectively. When applying the group sparsity regularization, the replicated elements can be considered as independent from each other.

4.4.3 Optimization of the group sparsity penalized cost function

By replicating the crossing elements in all subgroups, the subgroups are decoupled. Therefore, the optimization of the cost function 4.30 can be treated as a non-overlapping group Lasso problem where the corresponding proximal operator has an analytic expression.

Denote f_{d} as the normalized data error in (4.30) and f_{o} the normalized object error. Enforcing the replication strategy, the previous cost function becomes

$$F^{\mathcal{W}}(\boldsymbol{J}, \boldsymbol{\beta}) = f_{\mathsf{d}}(\boldsymbol{J}) + f_{\mathsf{o}}(\boldsymbol{J}, \boldsymbol{\beta}) + \Lambda_1 \|\boldsymbol{z}_g\|_{2,1} + \frac{\Lambda_2}{2} \|\boldsymbol{z} - G_{\boldsymbol{\beta z}}\boldsymbol{\beta}\|_2^2 \tag{4.31}$$

$\boldsymbol{z}$ is a "flattened" version of $\boldsymbol{\beta}$, where all overlapping groups in $\boldsymbol{\beta}$ become non-overlapping by replicating the crossed elements. $\Lambda_1 = \{\lambda_{1,1}, \lambda_{1,2}, \ldots, \lambda_{1,K}\}$ and $\Lambda_2 = \{\lambda_{2,1}, \lambda_{2,2}, \ldots, \lambda_{2,K}\}$ are two hyperparameter sets with K the total number of iterations. $G_{\boldsymbol{\beta z}}$ is the mapping matrix that yields $\boldsymbol{z}$ from $\boldsymbol{\beta}$ such that

$$\tilde{\boldsymbol{z}} = G_{\boldsymbol{\beta z}}\boldsymbol{\beta} \tag{4.32}$$

Although the elements appearing repeatedly are replicated and become independent from each other, they are essentially the same coefficient and should be consistent. The second regularization term aims to maintain consistency between $\boldsymbol{\beta}$ and its replicated and flattened version $\boldsymbol{z}$.

The analytic solution of $\ell_{2,1}$ norm for non-overlapping group Lasso problems is introduced in equation (4.28). Since there is a second regularization norm in the cost function (4.31), the solution becomes

$$x'_{g_i} = x_{g_i} \times \left(1 - \frac{\frac{\lambda_1}{\lambda_2}}{\|x_{g_i}\|_2}\right)_+, \ \forall i \tag{4.33}$$

The optimization procedure is sketched in Algorithm 3.

Algorithm 3 Group sparsity penalized CSI

Initialize $\boldsymbol{J}$ and $\boldsymbol{\chi}$ by back-propagation
repeat
  Calculate the data error $\boldsymbol{\rho}_{i,k}$ and the object error $\boldsymbol{r}_{i,k}$.
  Calculate the gradient $\boldsymbol{g}_{i,k}^{J}$
  Calculate the search direction $\boldsymbol{\nu}_{i,k}$
  Determine the step size α_k^J
  Update the contrast sources $\boldsymbol{J}_{i,k}$
  Update the total field $\boldsymbol{E}_{i,k}^{\text{tot}}$
  Update the contrast $\boldsymbol{\chi}_k$ by
  $\boldsymbol{\beta}_{k-0.5} = \mathcal{W}\{\frac{\sum_{i=1}^{N_s} \boldsymbol{J}_{i,k}\boldsymbol{E}_{i,k}^{\text{tot}*}}{\sum_{i=1}^{N_s} \|\boldsymbol{E}_{i,k}^{\text{tot}}\|^2}\}$ ($\boldsymbol{\beta}_{k-0.5}$ means the preliminary result in $k-$th iteration)
  Update $\boldsymbol{z}_{g_k} = \left(G_{\boldsymbol{\beta z}}\boldsymbol{\beta}_{k-0.5}\right)_g \times \left(1 - \frac{\lambda_{1,k}/\lambda_{2,k}}{\|(G_{\boldsymbol{\beta z}}\boldsymbol{\beta}_{k-0.5})_g\|_2}\right)_+$
  Update $\boldsymbol{\beta}_k = \boldsymbol{\beta}_{k-0.5} - \nabla_{\boldsymbol{\beta}}\left(\frac{\lambda_{2,k}}{2}\|\boldsymbol{z} - G_{\boldsymbol{\beta z}}\boldsymbol{\beta}_{k-0.5}\|_2^2\right)$
  Update hyperparameters $\lambda_{1,k+1}$ and $\lambda_{2,k+1}$
  Reconstruct the spatial-domain contrast by $\boldsymbol{\chi}_k = \mathcal{W}^*\boldsymbol{\beta}_k$
  Enforce positivity constraint on $\boldsymbol{\chi}_k$
until a stopping criterion is satisfied.

4.5 Implementation details

4.5.1 Wavelet settings

At each iteration, the contrast χ is decomposed by the DT-$\mathbb{C}$WT. The filter bank (FB) of the first stage of the DT-$\mathbb{C}$WT must be different from those of the succeeding stages to make the DT-$\mathbb{C}$WT approximately analytic for every stage. Let us denote l_{max} the maximum length of the decomposition filters and N_x and N_y the row and column dimensions of the image, respectively. The level of decomposition L then should be a positive integer holding that:

$$L \leq \log_2\left(\frac{\min\left(N_x, N_y\right)}{l_{\max}}\right) + 1 \tag{4.34}$$

Hereafter, Farras filters are used for the first stage, and Kingsbury Q-shift 6-tap filters for the following stages. So, here, $N_x = N_y = 64$, $l_{\max} = 10$ (due to the use of the Kingsbury Q-shift 6-tap filters) and according to (4.34) the largest possible decomposition level available is $L = 3$ which will be used in the following. The latter allows a finer description of the reconstructed obstacle thanks to the largest number of detail coefficients to be retrieved.

As seen in Fig. 4.8, three grouping strategies are adopted to introduce the structure information of the wavelet quadtree. Denote the three strategies as CSI-GS-1 (red), CSI-GS-2 (blue), and CSI-GS-3 (yellow). Here, the possible group sizes of three grouping arrangements are discussed. For a wavelet quadtree structure with a level of decomposition L:

- CSI-GS-1: If A belongs to the subbands $\{HL, LH, HH\}_L$, then A has no *parent* coefficient, and there is only one element in the subgroup. Otherwise, the subgroup contains A and the *parent* of A. The group size of CSI-GS-1 is 1 or 2.

Table 4.1: Choice of q for different methods

	CSI-GS-1	CSI-GS-2	CSI-GS-3
$q_{\Re}$	70	80	60
$q_{\Im}$	85	95	68

- CSI-GS-2: If A belongs to the subbands $\{HL, LH, HH\}_L$, as previously analyzed, the corresponding group size is 1. If A belongs to the subbands $\{HL, LH, HH\}_1$, the group size is L. Therefore, the group size of CSI-GS-2 varies according to the level of decomposition, ranging from 1 to L.
- CSI-GS-3: If A belongs to the subbands $\{HL, LH, HH\}_1$, then A have no *children* coefficients and in this case the group size is 1. Otherwise, A and its four *children* are included in the same subgroup. Consequently, the group size of CSI-GS-3 is 1 or 5.

4.5.2 Choice of hyperparameters

In equation (4.31), two hyperparameter sets Λ_1 and Λ_2 have to be determined. Following (Taşkin *et al.* 2017), they are chosen adaptively according to the magnitudes of wavelet coefficients and updated at each iteration.

Let us denote $P_{i\%}(.)$ the i-th percentile of a vector. At k-th iteration, $\lambda_{1,k}$ is set to $P_{q\%}(\boldsymbol{\beta}_k)$ and $\lambda_{2,k}$ is associated with $\lambda_{1,k}$ where the ratio of $\lambda_{2,k}$ to $\lambda_{1,k}$ is set to $P_{q\%}(\|\boldsymbol{z}_g\|_{2,1})$. q, which remains the only hyperparameter to be chosen, is fixed via a "trial-error" scheme according to the applied grouping strategy. Since $\boldsymbol{\chi}$ is a complex-valued function, q is also a complex-valued hyperparameter:

$$q = q_{\Re} + iq_{\Im} \tag{4.35}$$

q has to be *a priori* fixed and the choice is made by running the inversion for a set of $(q_{\Re}, q_{\Im})$ (varying from 50 to 95). In Fig. 4.9 the final error Err (χ) is plotted as a function of $q_{\Re}$ and $q_{\Im}$ and compared to the one of CSI (green line).

The above exhibits that CSI-GS methods outperform the CSI one for a large range of $q_{\Re}$ and that their effectiveness does not depend too much on the chosen value. It can be noticed that the range for $q_{\Re}$ and $q_{\Im}$ is narrower for CSI-GS-2 (Fig 4.9(b)) than for CSI-GS-1 (Fig 4.9(a)) and CSI-GS-3 (Fig 4.9(c)). The choices of $q_{\Re}$ and $q_{\Im}$ for different methods are in Table 4.1 and are drawn as a point in each subfigure of Fig. 4.9.

4.6 Numerical results

In the numerical simulation, the model used is still the "Austria" profile. The settings of the scattering system are the same as in Chapter 3. To remind, the region of interest $\mathcal{D}$ is $l = 2\,\mathrm{m}$ sided. For the direct problem, $\mathcal{D}$ is discretized into 50×50 cells, and for the inverse one, it is discretized into 64×64 cells. The region of interest is contained in free space $\mathcal{C}$. N_s sources and N_r receivers are evenly distributed on an observation circle of radius $r = 3.75\,\mathrm{m}$. The relative permittivity of the embedding medium is $\varepsilon_b = 1$. The collected data are corrupted by Gaussian noise. The frequency of operation is $600\,\mathrm{MHz}$.

In this Chapter, the algorithm is tested on lossy scatterers. The scatterer has constant permittivity and conductivity. $\varepsilon(\boldsymbol{r}) = 2$ and $\sigma(\boldsymbol{r}) = 17\,\mathrm{mS/m}$. Fig. 4.10 shows the relative permittivity and conductivity of the model.

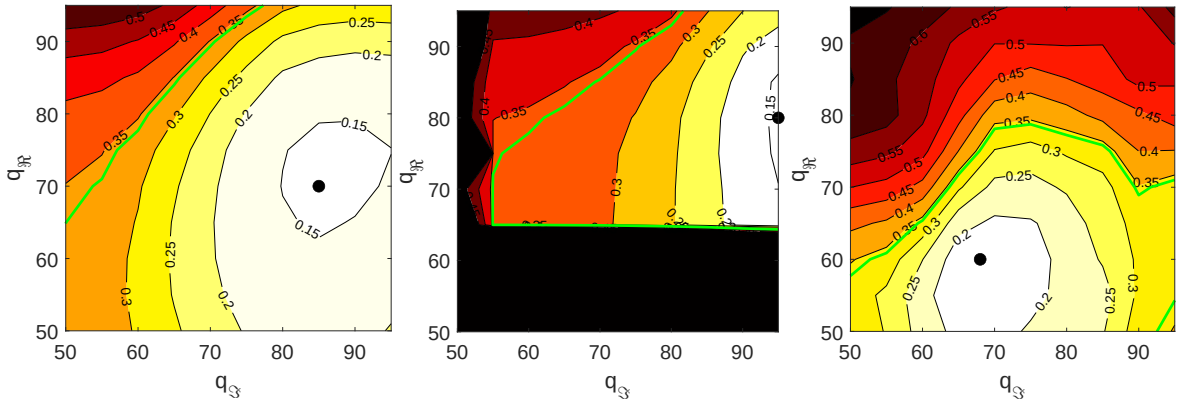

(a) CSI-GS-1 (b) CSI-GS-2 (c) CSI-GS-3

Figure 4.9: Parametric study for the choice of $q_{\Re}$ and $q_{\Im}$. The final error Err (χ) is plotted as a function of $q_{\Re}$ and $q_{\Im}$ and compared to the one of CSI (green line). $N_s \times N_r = 32 \times 32$

(a) Permittivity (b) Conductivity

Figure 4.10: "Austria" model - Relative permittivity $\epsilon(\mathbf{r})$ and conductivity $\sigma(\mathbf{r})$ $(\mathrm{mS/m})$

4.6.1 Results of various combinations of N_r and N_s

To analyze the advantages of the proposed approaches when reduced information is provided, CSI-GS-1, CSI-GS-2, and CSI-GS-3 are tested under three settings of sources and receivers. The results of CSI are also displayed for the sake of comparison. Results are shown in Fig. 4.11.

When there are 32 sources and 32 receivers, the real part of the model retrieved using CSI is roughly reconstructed. The general shape of the disks and rings can be recognized but with obvious discontinuities. As for the imaginary part, only the external boundary of the profile is preserved with also discontinuities, whereas the internal pixels cannot be found.

With the group sparsity-guided regularization, CSI-GS-1, CSI-GS-2, and CSI-GS-3 allow better reconstructions. The model is smoother, and the edges are well preserved. The reconstructed permittivity and conductivity both have relatively smaller values. When the number of sensors is reduced to $N_s \times N_r = 18 \times 26$ and 16×24, more and more discontinuities appear in the results of CSI. Still, the proposed methods are capable of better reconstructing the model.

It should be noted that the results obtained by CSI-GS-3 are not as smooth as with the other two methods. Rectangle artifacts appear in both reconstructed permittivity and conductivity. This is due to the grouping method. The additional group sparsity regularization can be seen as an image restoration step. The pixels are supposed to be restored from their ancestors or children at adjacent scales. The first two grouping methods connect each pixel to its ancestor(s), making it possible to smooth pixels with the same ancestor(s). However, this implicit regularization disappears in the third grouping method as it places each pixel and its

Table 4.2: Relative error with different $N_s \times N_r$ – SNR = 20 dB

$N_s \times N_r$	Error	CSI	CSI-GS-1	CSI-GS-2	CSI-GS-3
32×32	Err(χ)	0.34	**0.14**	**0.14**	0.16
	Err($\Re\{\chi\}$)	0.27	**0.12**	**0.12**	0.15
	Err($\Im\{\chi\}$)	0.61	**0.21**	**0.21**	0.23
18×26	Err(χ)	0.42	**0.15**	0.16	0.18
	Err($\Re\{\chi\}$)	0.35	**0.13**	0.14	0.16
	Err($\Im\{\chi\}$)	0.70	0.23	**0.22**	0.25
16×24	Err(χ)	0.51	**0.17**	0.19	0.20
	Err($\Re\{\chi\}$)	0.47	**0.16**	0.18	0.19
	Err($\Im\{\chi\}$)	0.67	**0.22**	**0.22**	0.24

four children in the same group, and adjacent pixels do not share the same children.

The relative errors of the reconstructed contrast are in Table 4.2. It can be observed from the results that the proposed methods provide a better quality of reconstruction. When the number of sensors is reduced, the relative error obtained by CSI clearly increases, whereas the reconstruction quality remains relatively stable with them.

Fig. 4.12 shows the inversion curves of CSI, CSI-GS-1, CSI-GS-2 and CSI-GS-3, respectively. The data and object errors decrease smoothly for all four methods.

4.6.2 Analysis of robustness

To evaluate the robustness of proposed methods, noises of higher levels are considered with SNR = $15\,\mathrm{dB}$ and $10\,\mathrm{dB}$. Simulations are conducted with CSI and the proposed methods with the same parameter settings. Relative errors are given in Table 4.3 and Table 4.4. The results are displayed in Fig. 4.13 and Fig. 4.14.

When the noise is of $15\,\mathrm{dB}$, the relative error of $\boldsymbol{\chi}$ with CSI, CSI-GS-1, CSI-GS-2, and CSI-GS-3 for the configuration $N_r \times N_s = 32 \times 32$ increases by 21%, 2%, 3% and 2%, compared with a noise of 20 dB. For the configuration $N_r \times N_s = 18 \times 26$, the increase is of 14%, 3%, 3% and 2%. For the configuration $N_r \times N_s = 16 \times 24$, the increase is of 7%, 5%, 6% and 4%.

For a $10\,\mathrm{dB}$ noise, the increase is of 55%, 7%, 13% and 7% for the configuration $N_r \times N_s = 32 \times 32$. For the configuration $N_r \times N_s = 18 \times 26$, the increase is of 52%, 13%, 22% and 11%. For the configuration $N_r \times N_s = 16 \times 24$, the increase is of 21%, 9%, 13% and 8%.

To conclude, the quality of reconstruction degrades if higher and higher noise level for all algorithms. Yet, the proposed methods are much more robust compared with CSI.

4.6.3 Comparison of DT-$\mathbb{C}WT$ and DWT filters

To further illustrate the advantages of the DT-$\mathbb{C}$WT, experiments are conducted with DWT using the proposed methods.

Before that, the Kingsbury Q-shift filters used in our work have been explored. In previous work, the Kingsbury Q-shift 6-tap filters are used in the filter banks of DT-$\mathbb{C}$WT. Here, the 14-tap and 18-tap filters are applied to the proposed methods to compare their performance.

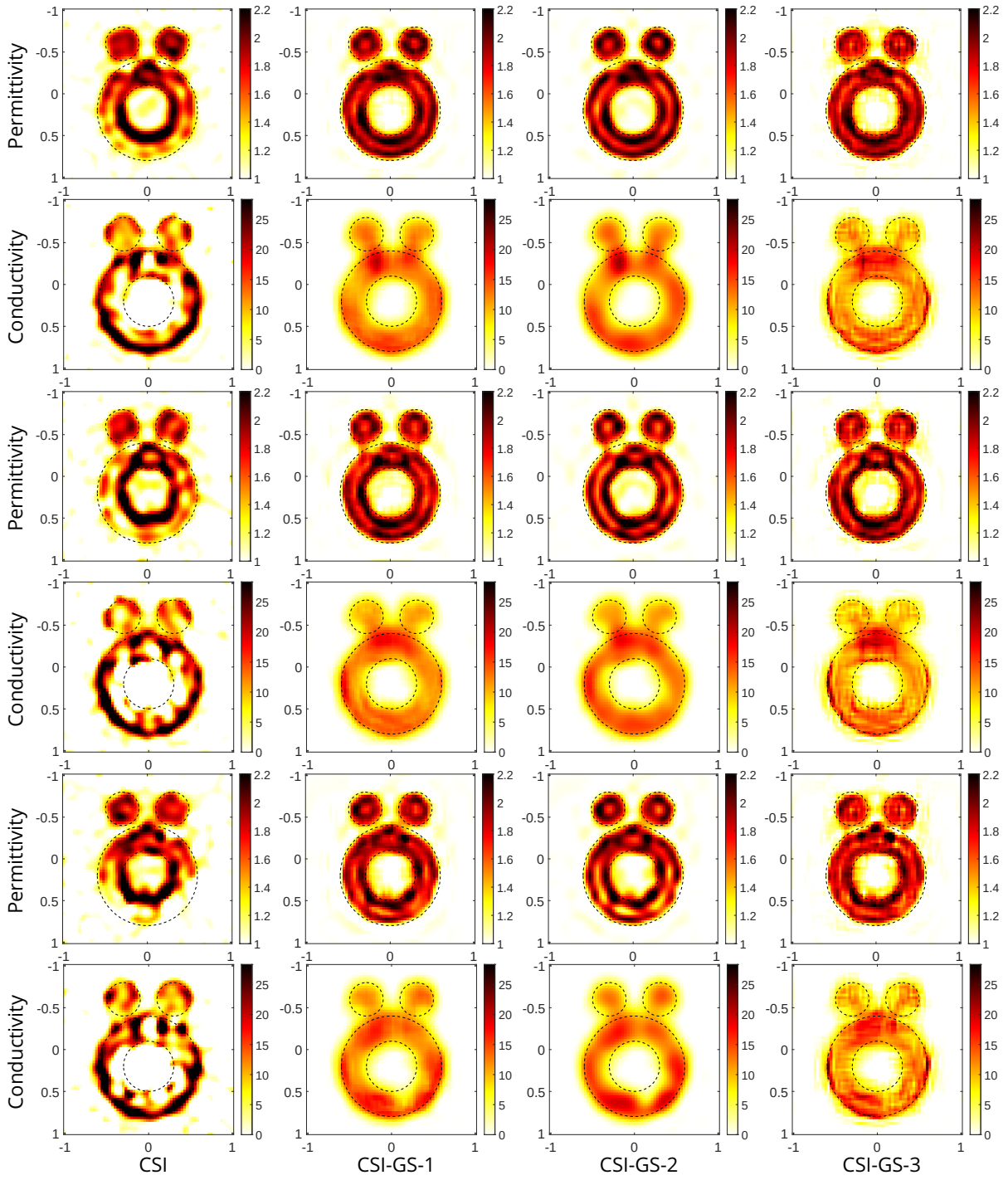

Figure 4.11: Reconstructed $\epsilon(\mathbf{r})$ (row 1, 3, 5) and $\sigma(\mathbf{r})$ (row 2, 4, 6) of "Austria profile" for various combinations of receiver and source numbers: $N_r \times N_s = 32 \times 32$ (row 1, 2), $N_r \times N_s = 18 \times 26$ (row 3, 4), $N_r \times N_s = 16 \times 24$ (row 5, 6). Gaussian noise of $20\,\mathrm{dB}$ is added to the scattered fields.

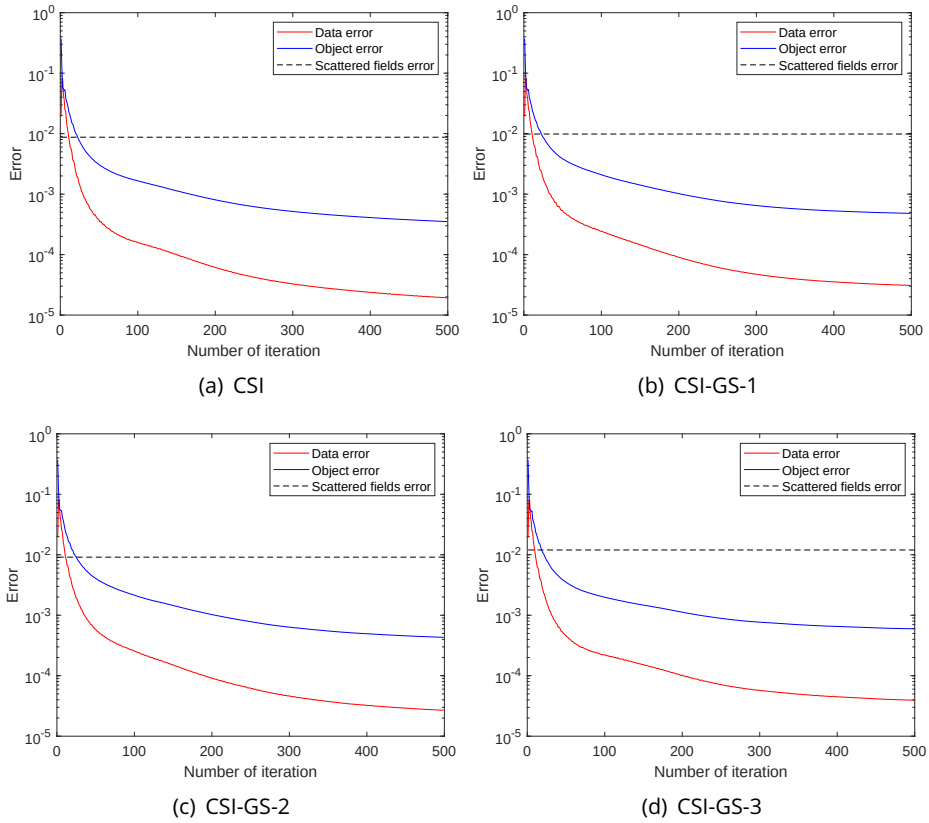

Figure 4.12: Inversion error curves of (a) CSI and (b)-(d) CSI-GS with three grouping arrangements. Gaussian noise of $20\,\mathrm{dB}$ is added to the scattered fields.

Kingsbury Q-shift 14-tap and 18-tap filters Relative errors of reconstructed contrast obtained with Kingsbury Q-shift 14-tap and 18-tap filters are given in Table 4.5 and Table 4.6. There is no noticeable improvement compared to the results obtained by 6-tap filters (Table 4.2).

Various wavelet filters Knowing that a large set of wavelets exists, only some more common ones are used. Relative errors obtained by CSI-GS-1, CSI-GS-2 and CSI-GS-3 using Haar, Daubechies 4 (db4), Daubechies 8 (db8), Coiflets 2 (C2), and Coiflets 4 (C4) are given in Table 4.7, 4.8 and 4.9. It can be observed that the relative errors obtained using DWT with different wavelet bases do not vary much. The results also show that the reconstruction quality obtained with DWT is not as good as that obtained with DT-$\mathbb{C}$WT (Table 4.2).

Illustrative results obtained with db4 wavelet are shown in Fig. 4.15. Suffering from lack of directionality, only details of three basic directions (horizontal, vertical, and diagonal) are well retrieved. Also, the weaker persistence between *parent* and *children* coefficients reduces the retrieval quality.

4.6.4 Comparison of $\ell_{2,1}$ norm and ℓ_1 norm

To enforce sparsity, the most popular regularization term is the ℓ_1 norm. To further demonstrate the benefit of the structure information provided by the $\ell_{2,1}$ norm, simulations are led with ℓ_1-penalized CSI, in which the group sparsity regularization term $\lambda\|\beta_g\|_{2,1}$ in (4.30) is replaced by $\lambda'\|\beta\|_1$.

To tackle the new cost functional with the ℓ_1 norm, lines 11-12 in the algorithm dedicated to the $\ell_{2,1}$ norm

Table 4.3: Relative error with different $N_s \times N_r$ – SNR = 15 dB

$N_s \times N_r$	Error	CSI	CSI-GS-1	CSI-GS-2	CSI-GS-3
32×32	Err(χ)	0.55	**0.16**	0.17	0.18
	Err$(\Re\{\chi\})$	0.47	**0.14**	0.15	0.16
	Err$(\Im\{\chi\})$	0.86	**0.23**	**0.23**	0.27
18×26	Err(χ)	0.56	**0.18**	0.19	0.20
	Err$(\Re\{\chi\})$	0.47	**0.16**	0.18	0.18
	Err$(\Im\{\chi\})$	0.88	**0.26**	**0.26**	0.28
16×24	Err(χ)	0.58	**0.22**	0.25	0.24
	Err$(\Re\{\chi\})$	0.49	**0.20**	0.24	0.22
	Err$(\Im\{\chi\})$	0.92	**0.27**	0.28	0.28

Table 4.4: Relative error with different $N_s \times N_r$ – SNR = 10 dB

$N_s \times N_r$	Error	CSI	CSI-GS-1	CSI-GS-2	CSI-GS-3
32×32	Err(χ)	0.89	**0.21**	0.27	0.23
	Err$(\Re\{\chi\})$	0.76	**0.18**	0.24	0.20
	Err$(\Im\{\chi\})$	1.40	**0.33**	0.35	0.34
18×26	Err(χ)	0.94	**0.28**	0.38	0.29
	Err$(\Re\{\chi\})$	0.79	**0.26**	0.39	**0.26**
	Err$(\Im\{\chi\})$	1.53	**0.36**	**0.36**	0.43
16×24	Err(χ)	0.72	**0.26**	0.32	0.28
	Err$(\Re\{\chi\})$	0.57	**0.24**	0.31	**0.24**
	Err$(\Im\{\chi\})$	1.32	**0.35**	0.36	0.40

Table 4.5: Relative error with Kingsbury Q-shift 14-tap filter – SNR = 20 dB

$N_s \times N_r$	Error	CSI-GS-1	CSI-GS-2	CSI-GS-3
32×32	Err(χ)	**0.14**	**0.14**	0.16
	Err$(\Re\{\chi\})$	0.13	**0.12**	0.14
	Err$(\Im\{\chi\})$	**0.21**	**0.21**	0.23
18×26	Err(χ)	**0.15**	0.16	0.17
	Err$(\Re\{\chi\})$	**0.13**	0.14	0.15
	Err$(\Im\{\chi\})$	0.23	**0.22**	0.25
16×24	Err(χ)	**0.17**	0.19	0.19
	Err$(\Re\{\chi\})$	**0.16**	0.18	0.18
	Err$(\Im\{\chi\})$	**0.22**	**0.22**	0.23

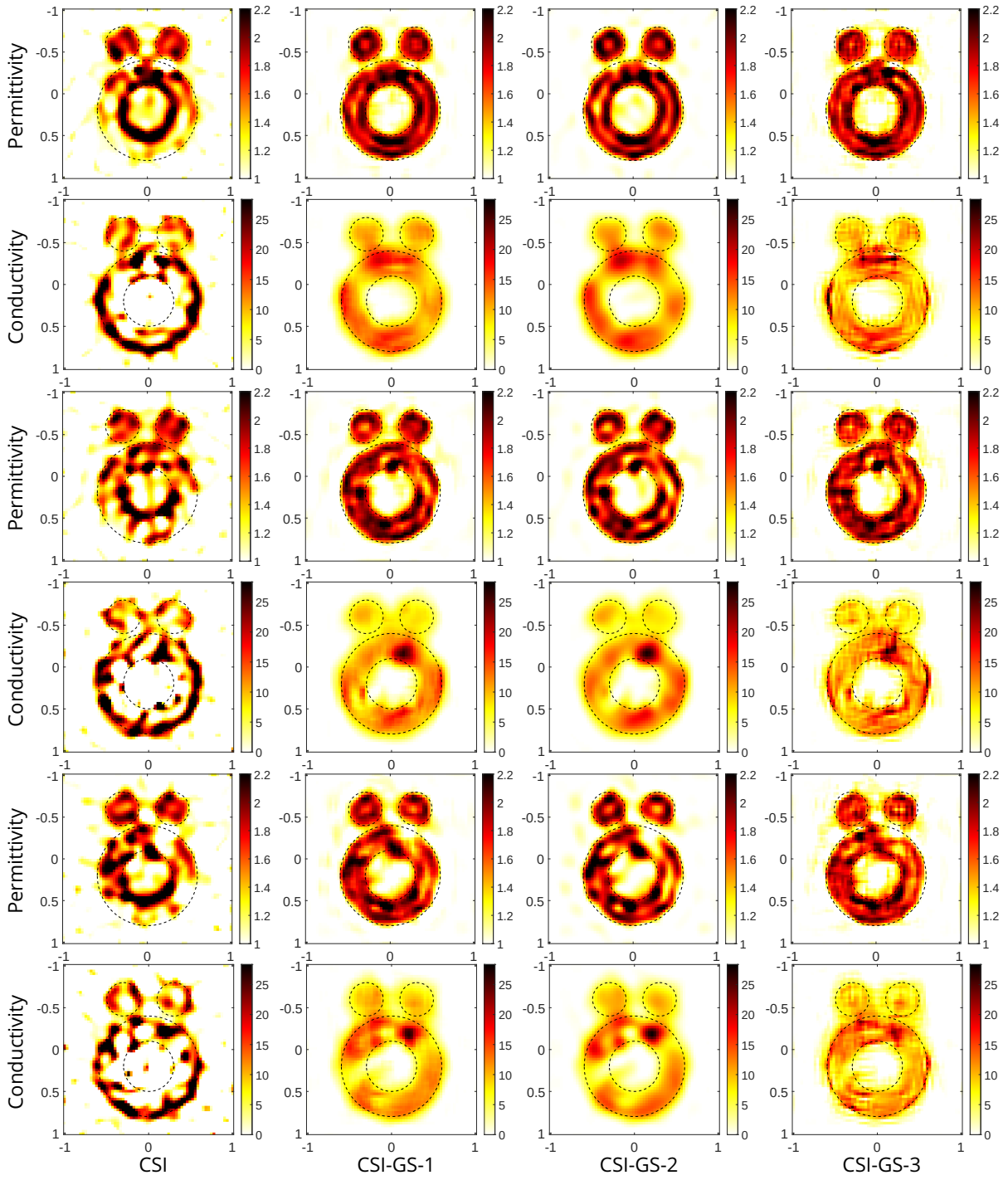

Figure 4.13: Reconstructed $\epsilon(\mathbf{r})$ (row 1, 3, 5) and $\sigma(\mathbf{r})$ (row 2, 4, 6) of "Austria profile" for various combinations of receiver and source numbers: $N_r \times N_s = 32 \times 32$ (row 1, 2), $N_r \times N_s = 18 \times 26$ (row 3, 4), $N_r \times N_s = 16 \times 24$ (row 5, 6). Gaussian noise of $15\,\mathrm{dB}$ is added to the scattered fields.

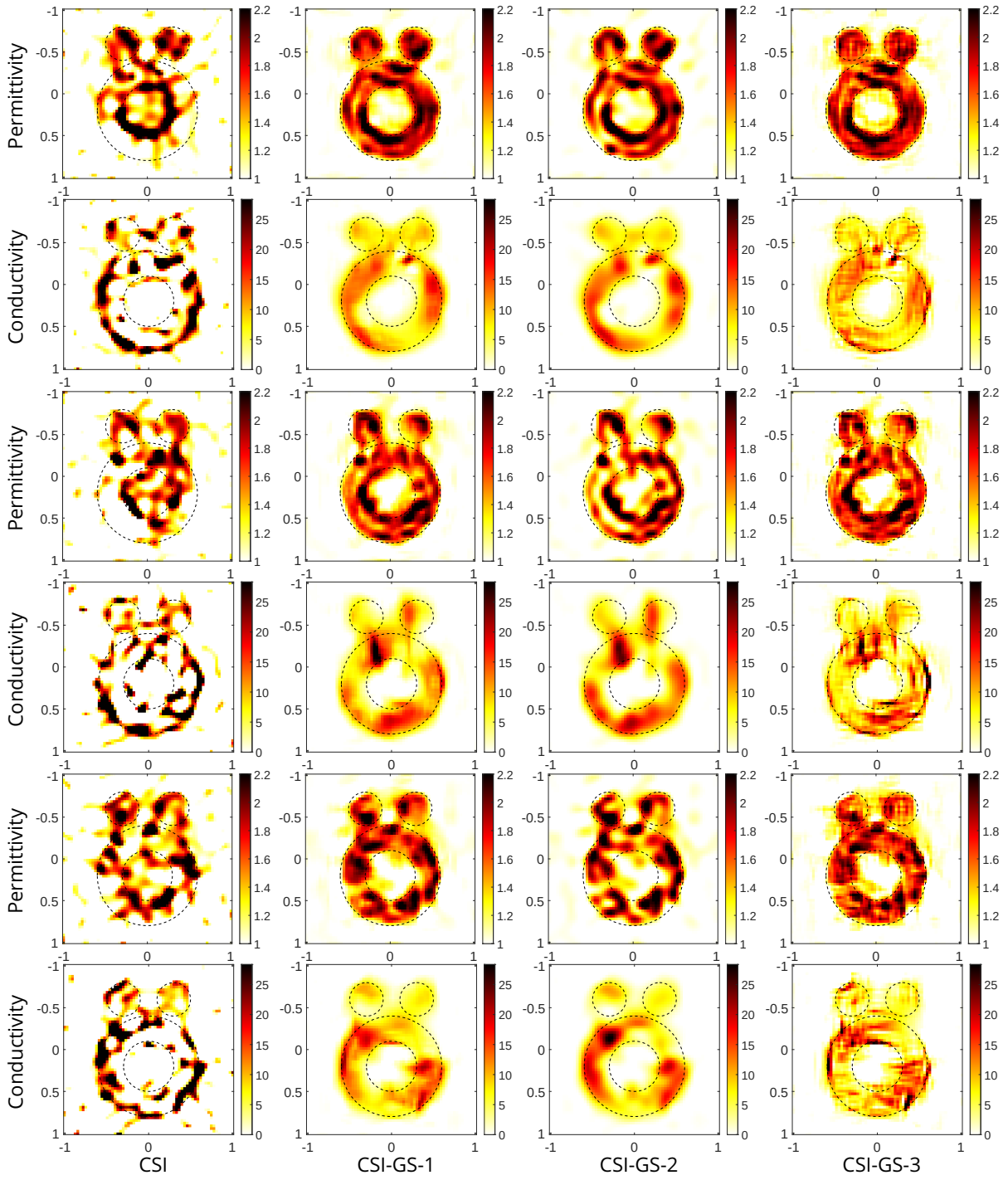

Figure 4.14: Reconstructed $\epsilon(\mathbf{r})$ (row 1, 3, 5) and $\sigma(\mathbf{r})$ (row 2, 4, 6) of "Austria profile" for various combinations of receiver and source numbers: $N_r \times N_s = 32 \times 32$ (row 1, 2), $N_r \times N_s = 18 \times 26$ (row 3, 4), $N_r \times N_s = 16 \times 24$ (row 5, 6). Gaussian noise of $10\,\mathrm{dB}$ is added to the scattered fields.

Table 4.6: Relative error with Kingsbury Q-shift 18-tap filter – SNR = 20 dB

$N_s \times N_r$	Error	CSI-GS-1	CSI-GS-2	CSI-GS-3
32×32	Err(χ)	**0.14**	**0.14**	0.16
	Err$(\Re\{\chi\})$	0.13	**0.12**	0.15
	Err$(\Im\{\chi\})$	**0.21**	**0.21**	0.23
18×26	Err(χ)	**0.16**	0.17	0.18
	Err$(\Re\{\chi\})$	**0.14**	0.16	**0.16**
	Err$(\Im\{\chi\})$	**0.22**	0.23	0.25
16×24	Err(χ)	**0.18**	0.19	0.20
	Err$(\Re\{\chi\})$	**0.17**	0.19	0.19
	Err$(\Im\{\chi\})$	**0.22**	**0.22**	0.23

Table 4.7: Relative error obtained with some common wavelets using CSI-GS-1

$N_s \times N_r$	Error	Haar	db4	db8	C2	C4
32×32	Err(χ)	NA	**0.18**	0.19	**0.18**	0.21
	Err$(\Re\{\chi\})$	NA	0.15	0.16	0.15	0.17
	Err$(\Im\{\chi\})$	NA	0.30	0.34	0.30	0.37
18×26	Err(χ)	0.25	0.22	0.24	**0.21**	0.27
	Err$(\Re\{\chi\})$	0.30	0.18	0.20	0.18	0.22
	Err$(\Im\{\chi\})$	0.30	0.36	0.39	0.33	0.43
16×24	Err(χ)	0.33	**0.25**	0.29	0.28	0.32
	Err$(\Re\{\chi\})$	0.29	0.23	0.27	0.27	0.30
	Err$(\Im\{\chi\})$	0.49	0.32	0.37	0.35	0.39

Table 4.8: Relative error obtained with some common wavelets using CSI-GS-2

$N_s \times N_r$	Error	Haar	D4	D8	C2	C4
32×32	Err(χ)	NA	**0.19**	0.20	0.20	0.22
	Err$(\Re\{\chi\})$	NA	0.16	0.17	0.17	0.19
	Err$(\Im\{\chi\})$	NA	0.31	0.34	0.32	0.36
18×26	Err(χ)	0.30	**0.24**	0.26	0.25	0.29
	Err$(\Re\{\chi\})$	0.24	0.21	0.23	0.23	0.26
	Err$(\Im\{\chi\})$	0.52	0.38	0.38	0.36	0.41
16×24	Err(χ)	0.38	**0.29**	0.33	0.33	0.35
	Err$(\Re\{\chi\})$	0.34	0.27	0.32	0.32	0.35
	Err$(\Im\{\chi\})$	0.53	0.33	0.37	0.35	0.37

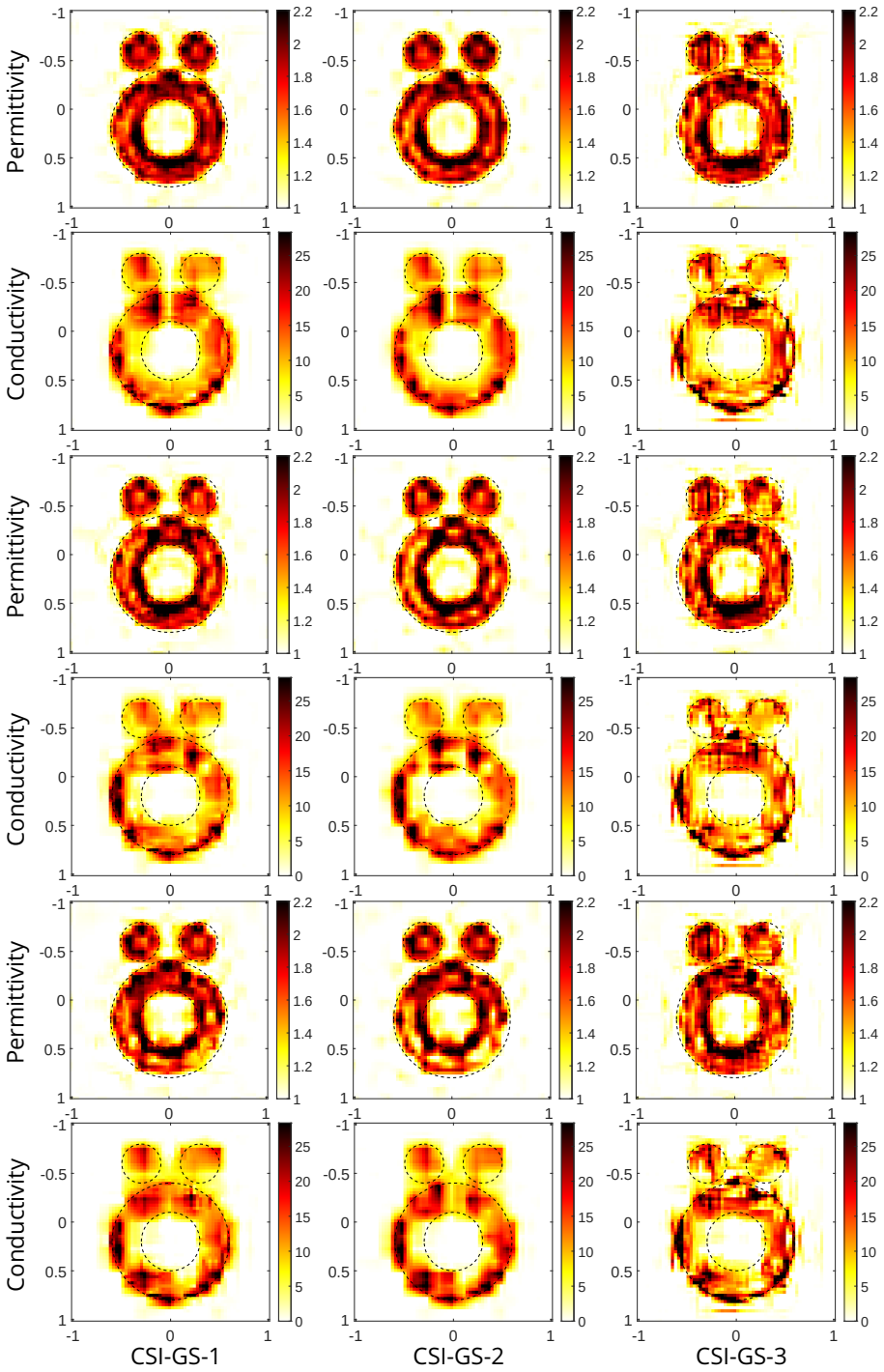

Figure 4.15: Reconstructed $\epsilon(\mathbf{r})$ (row 1, 3, 5) and $\sigma(\mathbf{r})$ (row 2, 4, 6) of "Austria profile" for various combinations of receiver and source numbers: $N_r \times N_s = 32 \times 32$ (row 1, 2), $N_r \times N_s = 18 \times 26$ (row 3, 4), $N_r \times N_s = 16 \times 24$ (row 5, 6). Gaussian noise of $20\,\mathrm{dB}$ is added to the scattered fields. The wavelet basis used is db4.

Table 4.9: Relative error obtained with some common wavelets using CSI-GS-3

$N_s \times N_r$	Error	Haar	D4	D8	C2	C4
32×32	$\text{Err}(\chi)$	NA	0.25	0.23	**0.19**	0.23
	$\text{Err}(\Re\{\chi\})$	NA	0.21	0.18	0.16	0.19
	$\text{Err}(\Im\{\chi\})$	NA	0.42	0.42	0.32	0.40
18×26	$\text{Err}(\chi)$	0.29	0.29	0.26	**0.22**	0.27
	$\text{Err}(\Re\{\chi\})$	0.21	0.24	0.21	0.18	0.22
	$\text{Err}(\Im\{\chi\})$	0.61	0.50	0.47	0.38	0.47
16×24	$\text{Err}(\chi)$	0.37	0.30	0.31	**0.27**	0.30
	$\text{Err}(\Re\{\chi\})$	0.32	0.25	0.27	0.24	0.25
	$\text{Err}(\Im\{\chi\})$	0.59	0.45	0.45	0.40	0.43

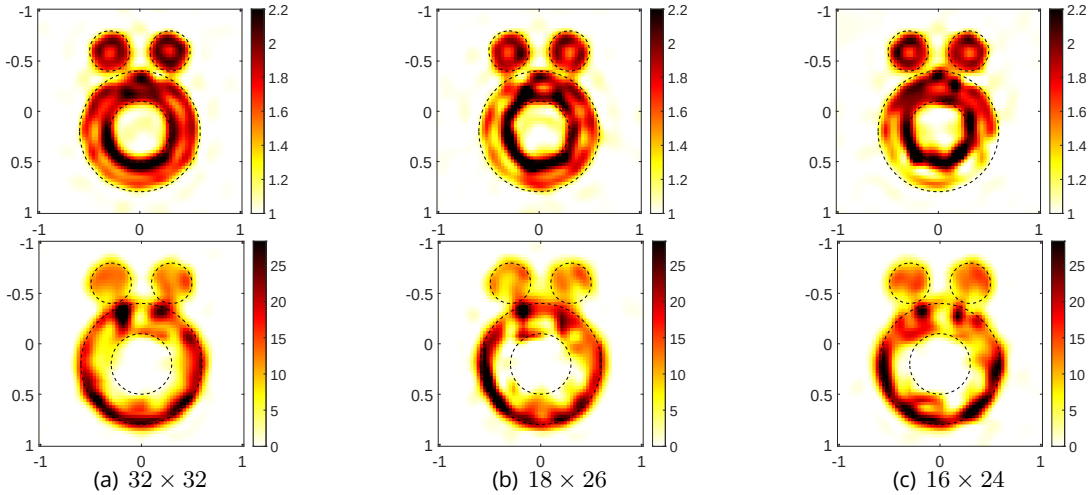

(a) 32×32 (b) 18×26 (c) 16×24

Figure 4.16: Reconstructed $\epsilon(\mathbf{r})$ (top) and $\sigma(\mathbf{r})$ (bottom) with ℓ_1-penalized CSI with different $N_s \times N_r$. The DT-$\mathbb{C}$WT is used.

are replaced by $\beta_k = \mathbb{S}_{\lambda'}\{\beta_{k-0.5}\}$ with $\mathbb{S}$ soft-thresholding operator. The hyperparameter λ' is determined like λ_2. $\lambda_1 = P_{q\%}(\beta)$, and q is chosen in accord with Table 4.1.

The results of ℓ_1-penalized CSI are shown in Fig. 4.16. The permittivity shape can be roughly identified, though obvious discontinuities appear when the number of sensors is reduced. As for the conductivity, only edges are found. The relative error is in Table 4.10. To conclude, the performance of $\ell_{2,1}$ norm is better than that of ℓ_1 norm thanks to the incorporation of structure information provided by the *parent-child relationship* between wavelet coefficients.

As for respective CPU times of the methods, they are illustrated on Model 1, with maximum iteration number of 500, on an Intel Core i5-8365U CPU ($1.60\,\text{GHz}$) with 16 GByte memory, refer to Table 4.11.

4.6.5 Test with circular dataset

The proposed method is further tested on a synthetically generated circular dataset, whose configuration and implementation details are the same as in section 3.4.2. Here, CSI and CSI-GS-1 are further tested using the dataset and the reconstructed results of four samples from the circular dataset are given in Fig. 4.17. The mean and variance of $\text{Err}(\boldsymbol{\chi})$ obtained by CSI and CSI-GS-1 on 250 samples are given in Table 4.12.

Table 4.10: Relative error with ℓ_1-penalized CSI

	32×32	18×26	16×24
$\mathrm{Err}(\chi)$	0.22	0.27	0.35
$\mathrm{Err}(\Re\{\chi\})$	0.18	0.24	0.34
$\mathrm{Err}(\Im\{\chi\})$	0.37	0.43	0.38

Table 4.11: Average CPU time (in s) for one iteration on an Intel Core i5-8365U CPU ($1.60\,\mathrm{GHz}$) with 16 GByte memory.

CSI	CSI+ℓ_1	CSI-GS-1		CSI-GS-2		CSI-GS-3	
		$\mathbb{C}$WT	DWT	$\mathbb{C}$WT	DWT	$\mathbb{C}$WT	DWT
0.24	0.30	0.28	0.28	0.28	0.31	0.30	0.30

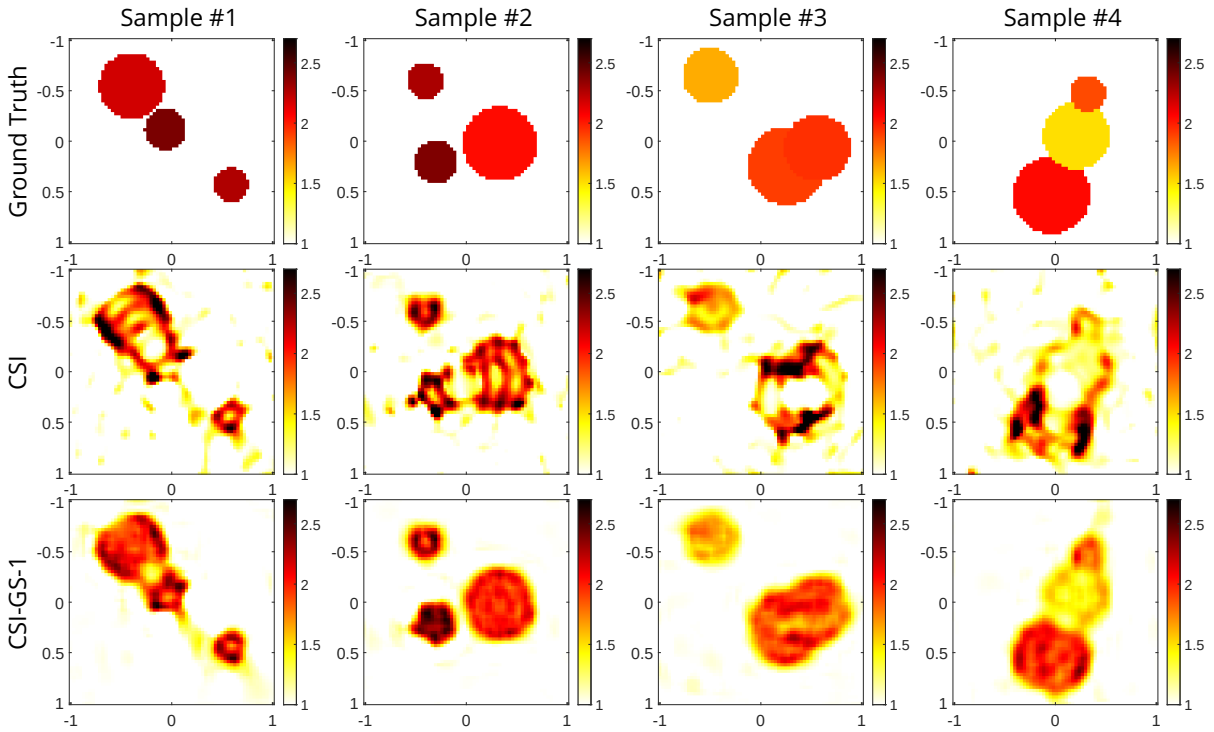

Figure 4.17: Reconstructed $\epsilon(\mathbf{r})$ of 4 samples in circular dataset for $N_s \times N_r = 16 \times 24$. Gaussian noise of $20\,\mathrm{dB}$ is added.

4.7 Conclusion

To conclude on the work discussed in the present chapter, the proposed group sparsity penalized CSI can improve the quality of reconstruction compared to CSI with reduced information. However, it can bring meaningful improvement only if CSI provides a satisfactory result as a good starting point.

Table 4.12: Mean and variance of Err($\boldsymbol{\chi}$) on 250 samples.

	CSI	CSI-GS-1
Mean	0.6996	**0.4978**
Variance	1.9205	**0.9530**

5 Basics of convolutional neural networks

Deep learning, mostly convolutional neural networks (CNN), have achieved great success for tasks as computer vision, e.g., image segmentation (Litjens et al. *2017), object recognition (Liang* et al. *2015). Deep learning is also successful for inverse imaging problems (McCann* et al. *2017; Jin* et al. *2017; Lucas* et al. *2018), like image denoising (Zhang and Salari 2005), restoration (Zhang, Zuo,* et al. *2017), super-resolution (Cui* et al. *2014), with worthy application in MRI-based medical imaging (Aggarwal* et al. *2019) as well.*

Deep-learning-based methodologies have recently been much explored in the ISPs community, which will be further discussed in the next chapter. This chapter introduces some basics of CNN and the unrolled method, based on which we will construct our network structure.

5.1 Introduction

Deep learning (LeCun *et al.* 2015) is a set of learning methods that model data with complex network architectures and nonlinear transformations. In the last decade, several types of neural networks have been developed. The multilayer perceptrons, composed of multiple layers of perceptrons, are the oldest and simplest ones. Recurrent neural networks (RNN) are usually used to process sequential data such as text or time series signals.

Among these different network structures, a Convolutional Neural Network (CNN) is designed to process data with a grid pattern, such as images. Note that the data to be processed by a traditional artificial neural network (ANN) should be in vector form. Grid-like data such as images must be expanded into a one-dimensional vector to be processed by ANN, which brings three limitations. Due to the high dimension of the resulting vector, the ANN tends to struggle with the computational complexity required to deal with image data. Moreover, the spatial information contained in the images is also lost when the images are expanded into vectors. The third limitation is the presence of overfitting phenomena due to a massive number of parameters contained in traditional ANN structures.

CNN can alleviate these problems. CNN acts directly on 2-D matrices or 3-D tensors, with the third channel containing extra information, e.g., three RGB color channels for digital images, real and imaginary parts in our case. Besides, the convolution operation can extract the spatial features from the original images. Furthermore, fewer parameters are produced by CNN than by traditional ANN by replacing the fully-connected layers with convolutional layers. The fewer parameters required to train the network, the less likely the network will overfit, and the predictive performance of the model will be improved.

5.2 CNN layers

5.2.1 Overall structure

CNN is typically composed of three types of layers. These are convolutional, pooling, and fully-connected layers. A CNN architecture can be formed by stacking these layers. The convolutional and pooling layers are used for feature extraction, whereas the fully-connected layer maps the extracted features into the

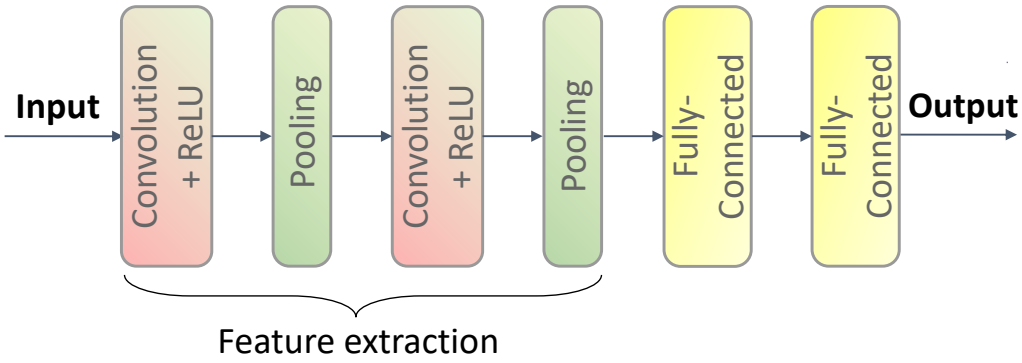

Figure 5.1: A typical CNN architecture

final output.

A simple CNN architecture is illustrated in Fig. 5.1. The convolution operation is usually followed by a nonlinear activation function (usually a rectified linear unit (ReLU)), forming a convolution block together. Pooling layers are used to downsample the feature maps to reduce their dimensionality. The above layers are the core part of CNN and are usually repeated several times to improve the performance of the model. Finally, the fully-connected layers are typically used to interfere with all extracted features and produce the final output. More details on each layer are given below.

5.2.2 Convolutional layer

The convolutional layer is the core part of the CNN structure. Let us recall the definition of the convolution between two functions f and g

$$(f * g)(x) = \sum_t f(t)g(x-t) \tag{5.1}$$

Likewise, the 2-D convolution for images is defined as

$$(K * I)(i,j) = \sum_{m,n} K(m,n)I(i-m, j-n) \tag{5.2}$$

K is the convolution filter, also called the *kernel*. Consider an input sensor I, at each location of the tensor, the convolution calculates an element-wise product between each element of the kernel in the first step. The second step is to sum up, the previous results to obtain the final output value in the corresponding location of the output tensor. Then, the kernel moves by a number s of pixels, s is called the *stride*. In other words, the kernel slides over the whole input tensor.

Zero-padding The above convolution operation does not allow the center of each kernel to overlap the outermost element of the input tensor. Furthermore, each convolution operation reduces the height and width of the feature map. To effectively extract the boundary information of the image and control the dimension of the output feature map, we usually use padding techniques, especially zero-padding, where rows and columns of zeros are added on each side of the input tensor. We can then alter the dimension of the output of convolutional layers.

Suppose the input tensor is of dimension $W_i \times H_i \times C_i$ (W_i and H_i denote the width and height of the 2-D image, respectively. C_i is the number of channels.) If we apply C_o kernels, then the output tensor is of

dimension $W_o \times H_o \times C_o$, the output size after the convolution and padding operation can be calculated by the following formula.

$$W_o = \frac{W_i - k + 2p}{s} + 1 \tag{5.3}$$

$$H_o = \frac{H_i - k + 2p}{s} + 1 \tag{5.4}$$

where k is the kernel size, p represents the amount of zero padding set, and s is the stride.

Stride and kernel size The stride and kernel size are two key parameters to characterize the convolution operation. Define the dimensionality of the region overlapping with the kernel as the *receptive field* size of the neuron.

- Stride The stride of the kernel represents the extraction accuracy of the features. If the stride is small, more features will be extracted, and less information will be lost. Yet, it may result in a higher computational burden because more parameters are left after the convolution operation. In addition, the choice of the stride also affects the spatial size of the output feature maps.
- Kernel size The kernel size represents the size of the receptive field, and it is generally *odd number*$\times$ *odd number* i.e., 1×1, 3×3, 5×5, 7×7, for the following reasons:
  - *Benefit the padding operations* As previously mentioned, we sometimes need the size before and after convolution to remain unchanged. Then, we need to use padding techniques. Following equations (5.3) and (5.4), the input and output sizes are the same given that the padding amplitude is set to $\frac{(k-1)}{2}$ while s is set to 1. It is one possible choice and the most common choice to ensure that the spatial dimension remains unchanged before and after the convolution. If k is a even number, $\frac{(k-1)}{2}$ is not an integer.
  - *Facilitate finding "anchor" point* In CNN, the convolution operation is generally performed based on the position of the kernel. The "anchor" point is used to determine the position of the kernel with respect to the image. If the kernel size is an odd number, the "anchor" point is easy to find, which is naturally the center of the kernel. However, if the convolution kernel is an even number, the "anchor" point is difficult to find.

5.2.3 Nonlinear activation function

The outputs of convolutional layers are then passed through a nonlinear activation function. Generally, nonlinear activation layers are employed after all learnable layers. The main role of the activation function is to provide the neural network with nonlinear modeling capabilities. Convolution is a linear operation, so non-linear elements must be introduced to solve problems that linear models cannot. The neural network has hierarchical nonlinear mapping capability only after adding the activation function.

Activation functions (especially ReLU) can also build sparse matrices, which can remove redundancy in the data and preserve the characteristics of the data as much as possible. The ReLU is a simple thresholding operator

$$\mathsf{ReLU}(\boldsymbol{x}) = \max(\boldsymbol{x}, 0) \tag{5.5}$$

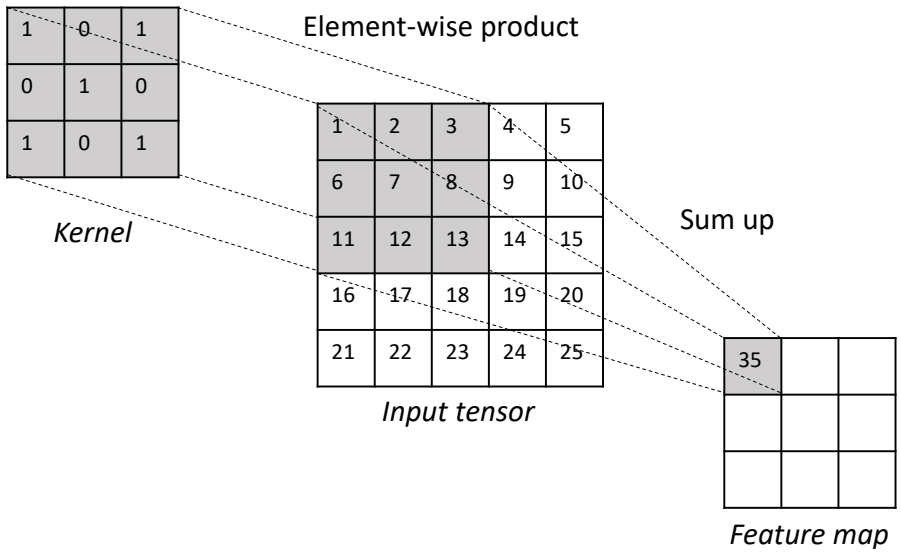

(a)

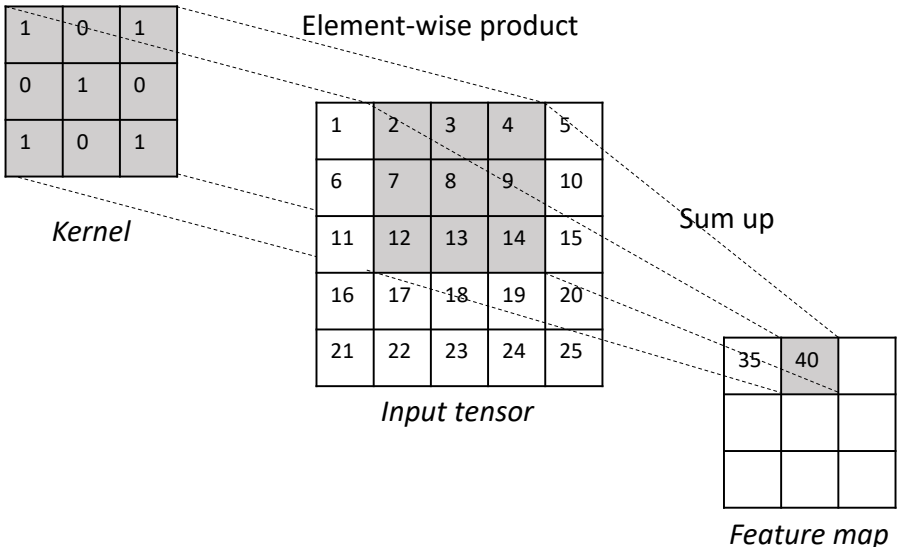

(b)

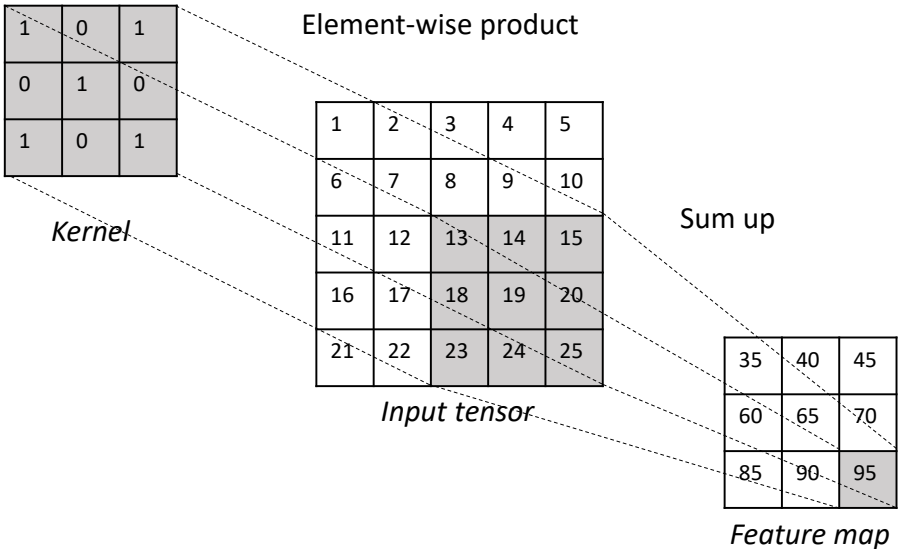

(c)

Figure 5.2: An example of convolution operation with a kernel size of 3×3. The stride s is 1. No zero-padding was added.

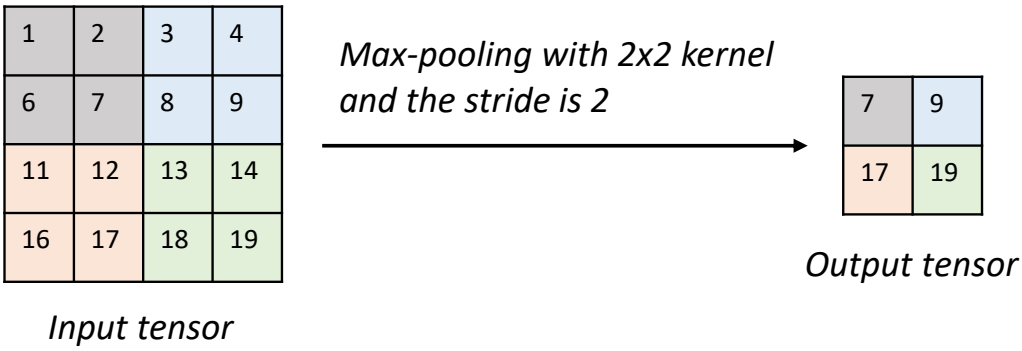

Figure 5.3: An example of max-pooling operation

5.2.4 Pooling layer

The pooling layer is usually placed after the convolution block. Pooling is essentially a down-sampling operation. For a given input feature map, the pooling operation takes the maximum or mean value on a small region. Similarly to the convolutional layer, we should choose a stride value and the small patches on which the pooling acts.

Among the pooling operators, max-pooling is the most commonly used. Fig. 5.3 illustrates an example of a max-pooling operation. The pooling process is similar to the convolution process. As shown in Fig. 5.3, the value in the neighborhood of a feature map is "scanned" with a 2×2 filter with a step size of 2. Here, the maximum value in the neighborhood is taken and output to the next layer. Unlike convolutional layers, the pooling layer has no parameters to update during the training process. It has two main roles:

- To retain the main features while reducing the dimensionality of feature maps to prevent overfitting and reduce the computational burden.
- To make the network less sensitive to small translations of the input tensor.

5.2.5 Fully-connected layer

After several repeated convolutional blocks and pooling layers, a traditional CNN structure generally ends with several fully-connected layers to map the extracted features to the final output. Namely, the neurons of a fully-connected layer are directly connected to the neurons in adjacent layers. This is why the dimension of the input tensor of fully-connected layers should be fixed.

The parameters of the fully connected layer are redundant, thus increasing the computational burden. This also leads to overfitting of the network. Therefore, it is common to replace fully connected layers with global average pooling layers or convolutional layers with kernel size 1×1.

5.2.6 Batch normalization

The training of a neural network is difficult because CNN contains many hidden layers, and the parameters of each layer will change with training. Therefore, the input distribution of the hidden layer will always vary, and each hidden layer will face the problem of covariate shift. This phenomenon is called internal covariate shift, which makes the input of each layer no longer independent and identically distributed. Due to this phenomenon, the data input into the activation function will fall into the saturation region, reducing the learning efficiency and even leading to the vanishing gradient problem.

Batch normalization (BN) (Ioffe *et al.* 2015) can be regarded as a data pre-processing step at every layer

of the network. BN is to normalize the input of each layer by mini-batch into a standard normal distribution with a mean of 0 and a variance of 1, thereby avoiding the vanishing gradient problem and greatly accelerating the convergence rate.

5.3 Training of CNN

In the previous part, different layers of CNN are described. Here, we discuss the training process of CNN by detailing several key concepts: loss function (§ 5.3.1), parameter initialization (§ 5.3.2), and optimizer choice (§ 5.3.3).

5.3.1 Loss function

Training a neural network is basically to find the parameters in the network which minimize the discrepancy between the output of the network and the ground truth in a training dataset. A loss function, also referred to as a cost function, is used to measure the data misfit between estimated results and the true one.

Different loss functions exist for different types of tasks. In ISPs, the CNN is usually used to obtain the contrast function (or contrast sources) from given inputs (scattered fields, pre-initialized contrast sources, etc.). It can be regarded as a regression task. Therefore, the Euclidean loss (or mean squared error (MSE)) is used.

The formula for calculating MSE loss between the output of the network $\hat{\boldsymbol{y}} \in \mathbb{R}^N$ and the ground truth $\boldsymbol{y} \in \mathbb{R}^N$ is as follows:

$$L(\hat{\boldsymbol{y}}, \boldsymbol{y}) = \frac{1}{N} \sum (\hat{\boldsymbol{y}} - \boldsymbol{y})^2 \tag{5.6}$$

The loss function value is calculated through forward propagation, where the input data is fed in the forward direction through the network and gets the output. Once we have the loss function value, this error will back-propagate from the last layer to the first layer based on the chain rule, and the gradient of each learnable parameter in the network can be obtained. These gradients will then be fed back to optimization methods (such as stochastic gradient descent), which are used to update the learnable parameters (kernels in convolutional layers and weights in fully-connected layers).

5.3.2 Parameter initialization

The initialization of the network parameters is essential because an inadequate initialization can result in a low convergence rate or even failure to converge. In this work, Kaiming initialization (He *et al.* 2015) is used, which is a recently proposed initialization method taking into account the non-linearity of activation functions, such as ReLU activations.

5.3.3 Optimization algorithm

The gradient descent method and its variants are commonly used in traditional optimization problems. It is also the usual selection for CNN learning problems. In our work, the Adaptive Moment Estimation (Adam) method is used, which is one of the latest trends in deep learning optimization. Adam has two key benefits: it is more memory efficient than other algorithms and needs less computational power. The algorithm is summarized in Algorithm 4.

During the learning process, the learning rate, which is the step size of the parameter updating, should be pre-defined. It should be adequately chosen to train the network effectively. Learning rate decay is a mod-

Algorithm 4 ADAM optimization method

1: Initialize the biased first moment estimate and biased second raw moment estimate $\mathbf{m}_t = 0$, $\mathbf{v}_t = 0$;
2: Initialize the hyper-parameter $\beta_{1,0} = 0.9$, $\beta_{2,0} = 0.999$, $\delta = 10^{-8}$, β_1, β_2 are exponential decay rates;
3: Update $t = t + 1$; $\mathbf{m}_t = \beta_1 \mathbf{m}_{t-1} + (1 - \beta_1)\mathbf{g}_t$, $\mathbf{g}_t$ is the gradient of loss function with respect to $\mathbf{W}$;
4: Update $\mathbf{v}_t = \beta_2 \mathbf{v}_{t-1} + (1 - \beta_2)\mathbf{g}_t^2$;
5: Compute bias-corrected moment estimates, $\widehat{\mathbf{m}}_t = \mathbf{m}_t/(1 - \beta_{1,t})$, $\widehat{\mathbf{v}}_t = \mathbf{v}_t/(1 - \beta_{2,t})$;
6: Update the parameters $\mathbf{W}_t = \mathbf{W}_{t-1} - \alpha \mathbf{m}_t/(\sqrt{\widehat{\mathbf{v}}_t} + \delta)$, α is exponential decaying step size;
7: $\|\mathbf{W}_t - \mathbf{W}_{t-1}\|^2 < \xi$, stop, otherwise, repeat steps from 3 to 6.

ern training technique that starts the training with a relatively high learning rate and then decreases/decays it slowly. It has been empirically observed to benefit the learning process and improve the generalization ability of the trained network.

Due to the limitation of available GPU memory, the training data is usually divided into mini-batch data. The number of samples in a batch is called batch size, a hyperparameter to be chosen. By employing the mini-batch training, the update of network parameters is not obtained by a single sample but is a weighted result from a batch of data.

The number of epochs, which defines the number of times the training algorithm will run on the entire training dataset, is also a hyperparameter to be pre-defined. It is a critical issue. Too few training epochs will lead to insufficient complexity of the trained network. Therefore, the network can capture the underlying data's features. This is called "underfitting". "Overfitting" is the opposite of "underfitting". Too many epochs lead to a too complex trained model that can capture even the noise in the data, and the training error of the model on the training data set will gradually decrease. However, the model does not work on data sets other than the training set.

The early stopping method is usually employed to address the problem of "overfitting". Early stopping consists in truncating the number of epochs in advance, that is, stopping epochs before the model converges on the training dataset to prevent overfitting. To perform early stopping, we keep a small portion (usually $20\% - 30\%$) of the training dataset as a validation set which is then used for cross-validation purposes. After each training epoch, the trained model will be applied to this validation set to test its performance. When the performance of the model starts to deteriorate in the next epoch, the training will stop because the generalization ability of the model begins to decline at this point. An illustration of the early stopping method is shown in Fig. 5.4.

With the components of CNN introduced above, we can construct and train a neural network. In the next section, the unrolled method is introduced, on which our network is designed.

5.4 Unrolled method

5.4.1 Background

Deep learning has achieved great success in some problems for computer vision tasks. In high-level vision problems such as face recognition and target detection, the performance of deep networks has been far superior to traditional methods. However, in some low-level vision problems, such as inverse imaging problems, data-driven methods cannot completely replace traditional model-driven methods. It is not wise to tackle the inverse problems only with empirically designed deep networks, while wholly abandoning domain knowledge is not an intelligent choice. Therefore, how to integrate domain knowledge into deep

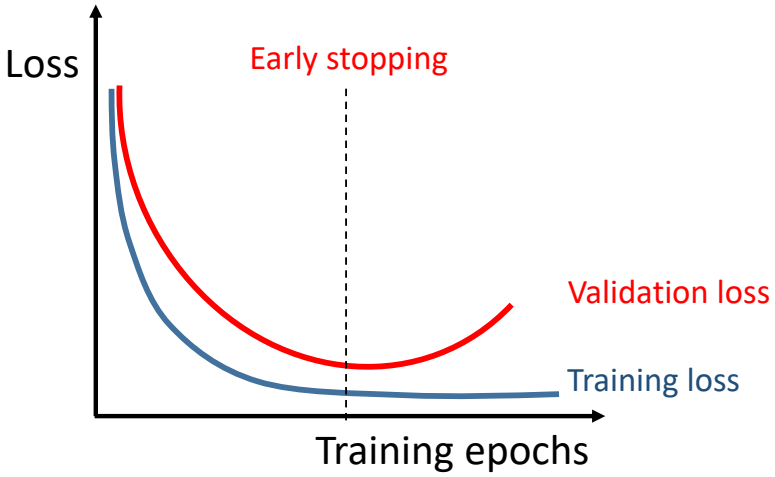

Figure 5.4: An example of early stopping during network training.

networks has become a new research trend in the field of deep learning. Among them, the unrolled method (or unrolling method) (Monga *et al.* 2021) provides effective means to address this issue.

Model-driven methods consist in establishing a mathematical model for the problem based on domain knowledge and then employing optimization tools to obtain the optimal solution of the model. Correspondingly, data-driven methods directly establish a nonlinear mapping relationship between input data and output results, and their performance is often closely related to the quality of training data and the network structure. To sum up, we find that the above two approaches mainly focus on using "domain knowledge" or are based on "data (and experience)", respectively. Then, if we can effectively combine these two different strategies, it will be very promising to design more robust and interpretable deep network models.

Designing an unrolled algorithm consists of two main steps:

- Take a traditional iterative algorithm and unroll it.
- Make some elements of the algorithm learnable.

In the following, we will give some examples of unrolled algorithms for solving inverse imaging problems.

5.4.2 Unrolled method for inverse imaging problems

The general framework and variants of the unrolled method have been much discussed to solve the inverse problems of interest. It replaces the components of iterative optimizers with learnable parameters or networks while integrating the knowledge of the physical model. Unlike the commonly used deep learning schemes that mainly adopt a single network to map the measurements or the approximate reconstructed results to the ground truth, the unrolled method uses a recurrent block architecture where the number of repeated blocks corresponds to the number of iterations.

In (Ongie *et al.* 2020), learning methods for solving different inverse imaging problems are discussed according to whether or not a forward model is known and to what extent it is used in training and testing, and whether or not the learning is supervised or unsupervised. The supervised case where the forward model is fully known is presented here. A general unrolled scheme is provided, based on the proximal gradient descent algorithm, where a trainable CNN replaces the proximal operator. In addition to the proximal operator, other free parameters, such as the step-size of descent, are also transformed into learnable parameters.

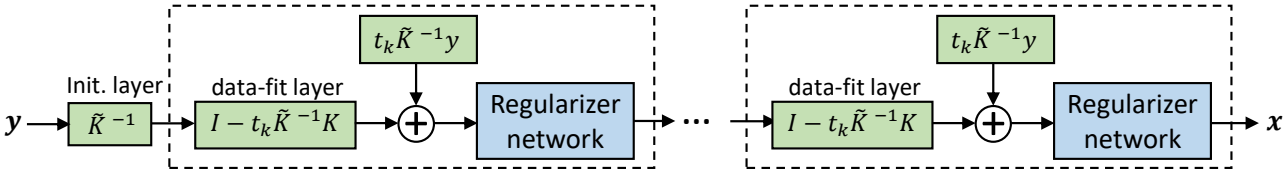

Figure 5.5: Unrolled model derived from the proximal gradient descent algorithm, where the proximal map is replaced with a deep CNN.

Denote $\mathcal{K}$ the forward model and $\tilde{\mathcal{K}}^{-1}$ an approximate inverse of $\mathcal{K}$, and we have

$$\boldsymbol{x} = \tilde{\mathcal{K}}^{-1}(\boldsymbol{y}) \tag{5.7}$$

When applying the learning approach to tackle inverse problems, the goal is to estimate a network that maps measurements $\boldsymbol{y}$ to images $\boldsymbol{x}$. Suppose $\mathcal{K}$ is a fully known linear operator; it can be embedded into the network structure in two ways. First, the incorporation of knowledge of $\mathcal{K}$ can be realized by mapping the measurements back to the image domain using the approximate inverse operator $\tilde{\mathcal{K}}^{-1}$. The result of the previous step is then used as the initialization of the network. In addition to the initialization step, the forward model $\mathcal{K}$ can also be incorporated into multiple layers of an unrolled network.

Consider an optimization problem of the following form

$$\arg\min_{\boldsymbol{x}} \frac{1}{2}\|\mathcal{K}(\boldsymbol{x}) - \boldsymbol{y}\|_2^2 + \mathcal{H}(\boldsymbol{x}) \tag{5.8}$$

where $\mathcal{H}(\boldsymbol{x})$ represents the regularization term. The proximal gradient descent method is commonly used to optimize it. Recall the formulas of proximal algorithm (4.26) and (4.27) introduced in the previous chapter, x can be updated at iteration k according to

$$\boldsymbol{x}^k = \text{prox}_{t\mathcal{H}(.)}\left(\boldsymbol{x}^k - t_k\nabla_{\boldsymbol{x}}\left\{\frac{1}{2}\|\mathcal{K}(\boldsymbol{x}) - \boldsymbol{y}\|_2^2\right\}\right) \tag{5.9}$$

wherein t_k the descent step size at k-th iteration. $\text{prox}_{t\mathcal{H}(.)}(x)$ is the *proximal operator* of $\mathcal{H}(.)$ at point x and it is a function of $\mathcal{H}$ and t

$$\text{prox}_{t\mathcal{H}(.)}(t) = \arg\min_{x} \frac{1}{2t}\|x - t\|_2^2 + \mathcal{H}(x) \tag{5.10}$$

Now, we unroll the above proximal gradient descent steps and take each iterative step as a sub-block for the network. The recurrent network architecture is sketched in Fig. 5.5. An initialization layer is placed at the beginning of the network by applying an approximate inverse operator to map measurements to the image domain. Then, the gradient descent step is performed. At the end of each sub-block, the proximal operator $\text{prox}_{t\mathcal{H}(.)}(.)$ is replaced with a trainable neural network mapping from images to images. The unrolled reconstruction network can be interpreted as learning a proximal operator.

In (Mardani *et al.* 2018) and (Diamond *et al.* 2017), authors both use the residual network to model the proximal map in traditional iterative algorithms. In (Zhang and Ghanem 2018), the architecture is designed based on the Iterative shrinkage-thresholding algorithm (ISTA), which aims at solving sparse linear inverse problems with ℓ_1-norm. Instead of using the traditional sparsifying transform, such as wavelet transform,

two symmetric convolutional blocks are applied to construct a learnable non-linear sparsifying transform and its inverse. In (Jin *et al.* 2017), the relationship between the general CNN structure and the iterative optimization methods is explored. Given a forward model where the forward operator is the convolution, the process of the corresponding proximal gradient descent algorithm can be interpreted as iteratively applying the convolutional filters, adding a bias, and using a point-wise nonlinearity, which has a similar form to the CNN. Based on this connection, modifications have been made to the widely used U-net architecture (Ronneberger *et al.* 2015) to reconstruct X-ray CT image. Likewise, in (Li, Wang, *et al.* 2019), the authors investigate the connection between iterative methods for nonlinear ISPs and the deep neural network (DNN). A complex-valued DNN is designed based on this connection.

6 Unrolled convolutional neural networks for ISPs

In this chapter, an unrolled deep learning scheme for solving full-wave non-linear ISPs is presented. An iterative neural network structure combining the CSI method and the residual network (ResNet) is designed, which is inspired by the so-called unrolled method. In the following, the application of CNN in ISPs is first discussed. Then, the proposed unrolled scheme combined with the CSI method is presented. Thorough numerical tests are carried out to evaluate the performance, stability, robustness, and reliability of the proposed approach.

6.1 Introduction

Recently, CNN have shown great potential in solving ISPs (Massa, Marcantonio, *et al.* 2019; Chen, Wei, *et al.* 2020; Salucci *et al.* 2022). Unlike traditional iterative methods that get the solutions from measurements and the domain knowledge, they benefit from the large data set to learn the unknown solution while the domain knowledge is less involved.

The advantages of applying deep learning tools to solve ISP are twofold. On the one hand, it allows real-time reconstruction whereas traditional iterative methods require computational time. On the other hand, by benefiting from the information contained in large-scale data, deep learning tools can sometimes solve highly non-linear ISPs for which traditional methods fail. However, collecting large-scale datasets may not be straightforward in real-world applications.

Deep learning approaches for solving ISPs can be roughly categorized into three types as follows, as already briefly introduced in Chapter 1.

- The contrast distribution can be directly derived from the measured data, the input of the neural network being the scattered fields, and the output being the contrast (Ran, Qin, *et al.* 2021). However, learning contrasts directly from scattered fields takes unnecessary time to learn known physical processes. Therefore, we need to combine domain knowledge and learning methods.
- Approaches of the second type consist in incorporating physical knowledge into deep learning (Wei *et al.* 2019a; Wei *et al.* 2019b; Liu, Roy, *et al.* 2022). These methods can somewhat reduce the nonlinearity of the relationship between the input and output of the neural network and simplify learning.
- A neural network can be combined also with traditional optimization methods. This third type still employs the traditional iterative approach to solve the ISPs but uses deep learning to complete the optimization procedure (Sanghvi, Kalepu, *et al.* 2020).

To achieve sound retrievals, incorporating domain knowledge into the deep model is of great importance. In addition to initializing the network with approximate results based on physical information as often made, the unrolled method, which has been introduced in the previous chapter, is a promising tool to address this issue, as exemplified in the recent contribution (Liu, Zhou, *et al.* 2022).

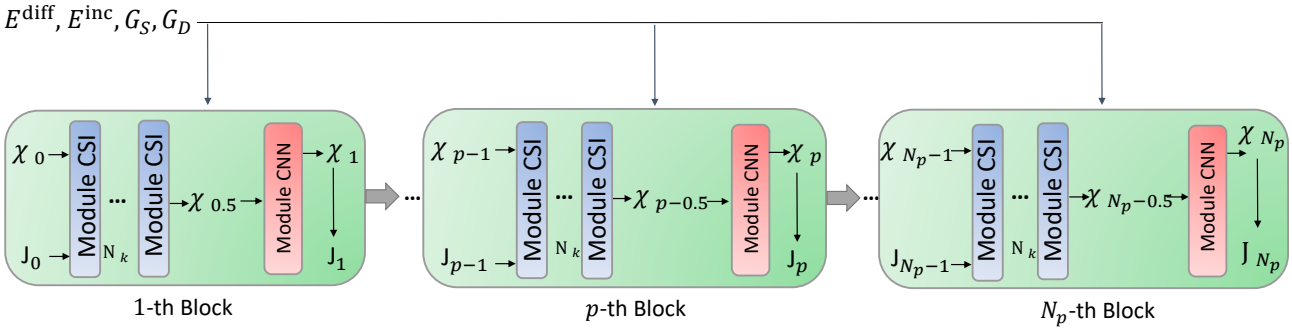

Figure 6.1: CSI-based unrolled neural network structure. $p \in \{1 \dots N_p\}$, N_p number of sub-blocks. $k \in \{1 \dots N_k\}$, N_k number of CSI iterations performed inside each sub-block. $\chi_{p-0.5}$ represents a preliminary result of χ at p-th step.

6.2 Proposed unrolled CNN scheme

In this section, a novel unrolled model which combines updating steps of CSI and a classical CNN structure is detailed. Denote the proposed unrolled network as CSI-Net.

The entire network has a recurrent block architecture that contains a series of sub-blocks. Each includes a set of CSI update steps and a CNN block, which corresponds to an update of contrast and contrast source, as it will be seen.

Then, several strategies are designed to improve the model. Due to the recurrent network structure, a combined loss function is set up, the weight parameters being determined automatically during training. Modifications are also made compared to a general unrolled method to adapt the network to nonlinear inverse problems.

The overall structure of the proposed network is sketched in Fig. 6.1, where each sub-block of the network contains two modules: *Module CSI* and *Module CNN*. In the following, the CSI block is first reviewed as the main brick of *Module CSI*. Then, the network structure adopted for *Module CNN* is introduced. Details of the approach follow.

6.2.1 Module CSI

Module CSI is constructed based on the CSI method, which was detailed in Section 3.1. As shown in Fig. 6.1, each sub-block contains a series of *Module CSI*, and each *Module CSI* contains one single CSI iteration.

In the first sub-block, *Module CSI* aims at providing an immediate initialization of $\boldsymbol{J}$ and $\boldsymbol{\chi}$ for the *Module CNN*. Then, in the following sub-blocks, *Module CSI* further refines the results that come from the precedent *Module CNN*. Note that the step size α^J is not a learnable parameter and it is determined by minimizing both data and state error functions.

6.2.2 Module CNN

In the proposed unrolled schema, the network structure in *Module CNN* is stacked by residual blocks. Residual learning has been proposed in (He *et al.* 2016) to deal with network degradation, which means that adding more layers might degrade the learning performance. The entire network structure of *Module CNN* is illustrated in Fig. 6.2. It thus consists of two residual blocks and two convolutional blocks.

Adding a shortcut between the input $\boldsymbol{x}$ and the output, the network has to learn the residual $\mathcal{H}(\boldsymbol{x})$ between ground truth and input. It should be easier to optimize than the original mapping, and this shortcut ensures that higher layers perform at least as well as lower ones.

The input of *Module CNN* is the contrast $\boldsymbol{\chi}$ obtained by *Module CSI*, which is a tensor of shape

$$[\text{Number of samples} \times \text{Number of channels} \times H \times W]$$

where H and W represent image height and width.

The number of input/output channels is 2 for a complex-valued image by splitting real and imaginary parts into two different channels; for a real-valued image, the second channel is empty.

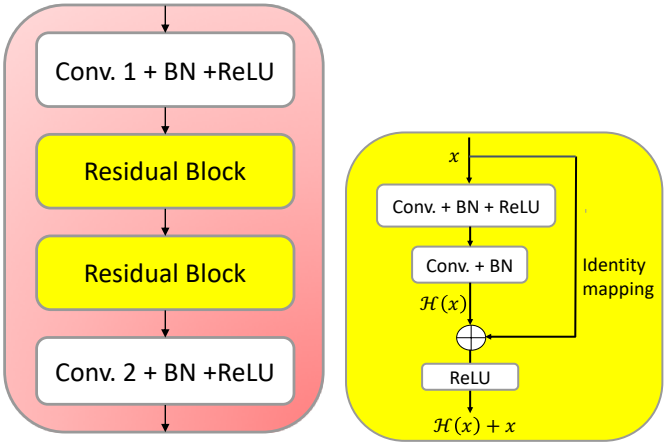

(a) Module CNN (b) Residual sub-block

Figure 6.2: Network structure of *Module CNN* and its residual sub-block.

For all convolutional layers, the kernels used to obtain the feature maps are of size 3×3. Inside the residual block, the number of kernels for each layer is 64. The number of kernels of layers *Conv.*1 and *Conv.*2 in *Module CNN* is 64 and 2, respectively.

To keep the spatial size of feature maps unchanged after each convolution, the stride of the convolution operation is set to 1, and a 1-sized zero-padding is added. Each convolutional layer is followed by batch normalization (BN).

Finally, a ReLU layer is added as the nonlinear activation layer used to overcome the vanishing gradient problem and add the nonlinearity to the model.

6.2.3 CSI-based unrolled CNN framework: CSI-Net

Inputs of CSI-Net As depicted in Fig. 6.1, the network contains a series of sub-blocks. For the first sub-block, the input is the pre-initialized contrast $\boldsymbol{\chi}$ and contrast source $\boldsymbol{J}$, obtained by standard back-propagation.

A closed-form contrast source is obtained as:

$$\boldsymbol{J}_0 = \frac{\|G_S^* \boldsymbol{E}^{\text{diff}}\|^2}{\|G_S G_S^* \boldsymbol{E}^{\text{diff}}\|^2} G_S^* \boldsymbol{E}^{\text{diff}} \tag{6.1}$$

and the corresponding contrast $\boldsymbol{\chi}_0$ derived from $\boldsymbol{J}_0$:

$$\boldsymbol{\chi}_0 = \frac{\sum_{i_s=1}^{N_s} \boldsymbol{J}_{i_s,0} \boldsymbol{E}_{i_s,0}^{\text{tot}*}}{\sum_{i_s=1}^{N_s} \|\boldsymbol{E}_{i_s,0}^{\text{tot}}\|^2} \tag{6.2}$$

Additionally, the inputs include as well auxiliary data $\boldsymbol{E}^{\text{diff}}, \boldsymbol{E}^{\text{inc}}, G_S, G_D$ to perform the CSI iterations.

Forward path Denote N_p the total number of sub-blocks and N_k the total number of CSI iterations performed inside each sub-block. In the p-th sub-block, there are two main steps.

- Firstly, the input passes through a sequence of *Module CSI*. In the commonly used unrolled deep learning framework, the gradient descent update step is performed only once inside each sub-block, where the step size is considered as a free parameter learned during training. In contrast, the step size α^J here is a constant determined at each iteration, thus not a learnable parameter. Moreover, instead of running a single CSI iteration in each sub-block, the CSI iteration is repeated several times. This modification comes from the following considerations: Data in *Module CSI* are not normalized, so the initialization of step size is essential and should respect the correct scale. So it is more convenient to determine the step size by following a traditional optimization. As it cannot be learned, the single iteration step is replaced by multiple iterations to speed up convergence and amplify improvements brought by *Module CSI*. At the end of this step, a preliminary reconstruction $\chi_{p-0.5}$ of the contrast χ is obtained.
- Secondly, the previous result $\chi_{p-0.5}$ is applied as input of *Module CNN*. Note that it should be normalized before being involved in the network. The output of this module is χ_p, which is the final result of the p-th sub-block, and the corresponding contrast source J_p is updated by solving the forward problem.

Loss function Since the proposed model has a cascade architecture, the choice of the loss function is important. The loss scale corresponding to each sub-block's output could significantly differ. To equally train each sub-block, a combined loss function built with the normalized mean square error (MSE) is chosen:

$$L = \sum_{i=1}^{N_p} \frac{\lambda_i L_i}{\sum_{j=1}^{N_p} \lambda_j}, \tag{6.3}$$

with

$$L_i = \sum_{e=1}^{N_e} (\tilde{x}_e^i - x_e)^2, \tag{6.4}$$

$$\lambda_i = \frac{L_0}{L_i} \tag{6.5}$$

where N_e denotes the number of elements in $\tilde{x}^i$, and λ_i is the weighting coefficient of i-th sub-block.

6.2.4 Evaluation's criteria & implementation's details

Evaluation criteria To evaluate the reconstruction quality from different points of view, in addition to the normalized reconstructed contrast error defined in equation (3.30), two more criteria are adopted:

1. Relative error of permittivity over the pixelized domain

$$Err_\varepsilon = \sqrt{\frac{1}{N_x \times N_y} \left[\sum_{i_x}^{N_x} \sum_{i_y}^{N_y} \left| \frac{\tilde{\varepsilon}_{i_x,i_y} - \varepsilon_{i_x,i_y}}{\varepsilon_{i_x,i_y}} \right| \right]} \tag{6.6}$$

2. Structural Similarity Index (Wang *et al.* 2004)

$$\text{SSIM}(\tilde{\chi}, \chi) = \frac{(2\mu_{\tilde{\chi}}\mu_{\chi} + C_1) + (2\sigma_{\tilde{\chi}\chi} + C_2)}{(\mu_{\tilde{\chi}}{}^2 + \mu_{\chi}{}^2 + C_1)(\sigma_{\tilde{\chi}}{}^2 + \sigma_{\chi}{}^2 + C_2)} \tag{6.7}$$

where μ_x and σ_x are the mean and the standard deviation of x, respectively. σ_{xy} is the covariance between x and y. $C_1 = (k_1 L)^2$, $C_2 = (k_2 L)^2$ are to stabilize the division with weak denominator where L the dynamic range of the pixel values. $k_1 = 0.01$ and $k_2 = 0.03$ by default.

To check on the advantage brought by *Module CSI*, one removes all *Module CSI* blocks from CSI-Net, and the model becomes a cascaded residual neural network, denoted as CC-ResNet. For comparison, results of CC-ResNet, the widely used U-net structure (detailed in Appendix B), and the iterative CSI method with positivity constraint are also displayed. For the latter, the number of iterations has been arbitrarily chosen as $N_k^{\text{CSI}} = 150$ and the algorithm is stopped when N_k^{CSI} is reached.

Implementation details Implementation details of the approach, including division of dataset and hyperparameters settings, are as follows. Several datasets are used to train the proposed model, each one comprising 2500 samples. Among the 2500 data pairs, 2000 are employed for training, 300 for validation, and 200 for testing. The Adam optimizer (Kingma *et al.* 2015) is chosen to optimize the loss function. 40 epochs are set in the training process. The size of the mini-batch is 20. The learning rate is set to 0.001, decayed by 0.1 each 10 epoch. N_k and N_p are chosen by compromising between learning performance and computational complexity, here $N_k = 10$ and $N_p = 4$.

Computations are run on a server with NVIDIA RTX A3000 GPU ($6\,\text{GB}$). The networks are implemented with Pytorch (Paszke *et al.* 2019). It takes $0.63\,\text{h}$ for CSI-Net training and $0.03\,\text{h}$ for CC-ResNet and U-net. It takes less than $0.4\,\text{s}$ to get the reconstruction using CSI-Net, and about $4\,\text{s}$ using CSI, U-Net being almost real-time.

6.3 CSI-Net results at single frequency

In this section, numerical experiments are carried out to evaluate the performance of the proposed methods. The details of the scattering system are as follows. The operating frequency is $400\,\text{MHz}$, the region of interest $\mathcal{D}$ is of $2\,\text{m}\times 2\,\text{m}$ size and is discretized into N square cells. For the forward problem, $N = 32 \times 32$. $N_r = 32$ receivers and $N_s = 16$ transmitters are evenly distributed on a circle of radius $r = 3\,\text{m}$ centered at (0, 0) m. The embedding medium is of $\epsilon_b = 1$.

6.3.1 Test with circular dataset

A synthetically generated circular dataset (Wei *et al.* 2019a) is used. Each sample contains disks of random quantities: number (between 1 and 3), relative permittivity (between 1.3 and 2), radius (between $0.15\,\text{m}$ and $0.4\,\text{m}$), and location. The scatterers may overlap. The collected fields used for training are noise-free. Unless specified, the scatterers are lossless.

The trained models are tested with 200 samples. Fig. 6.3 and 6.4 show six representative results obtained by three models and CSI. Results by CSI-Net are smoother, and edges are better preserved, especially when multiple scatterers interplay. In samples #1, #3, and #4, where the scatterers are very close to each other, only rough estimates are obtained by CC-ResNet and U-net. The shape and relative permittivity obtained

Table 6.1: Reconstruction quality of three models and CSI. SNR = $20\,\mathrm{dB}$.

	Model	Sample #1	#2	#3	#4	#5	#6
Err_χ	CC-ResNet	0.172	0.121	0.137	0.113	0.101	0.113
	CSI-Net	**0.027**	**0.028**	**0.021**	**0.027**	**0.017**	**0.014**
	U-net	0.166	0.085	0.108	0.100	0.125	0.093
	CSI	0.057	0.067	0.058	0.063	0.055	0.064
Err_ε	CC-ResNet	0.148	0.073	0.098	0.077	0.081	0.073
	CSI-Net	**0.048**	**0.045**	**0.037**	**0.050**	**0.034**	**0.029**
	U-net	0.149	0.074	0.090	0.072	0.096	0.071
	CSI	0.078	0.069	0.063	0.069	0.067	0.065
SSIM	CC-ResNet	0.340	0.475	0.445	0.425	0.488	0.499
	CSI-Net	**0.710**	**0.726**	**0.693**	**0.682**	**0.704**	**0.720**
	U-net	0.203	0.582	0.6514	0.569	0.531	0.669
	CSI	0.478	0.463	0.430	0.443	0.481	0.394

are not exact, and the boundaries are not clear. In samples #2 and #5, with CC-ResNet and U-net, the reconstruction of the weaker scatterers is influenced by the relatively stronger ones, so only the latter are well retrieved. Sample #6 is challenging since an obstacle is inside one another. CC-ResNet and U-net can retrieve the two large obstacles while the small nested one is missed. With CSI, the reconstructed scatterers exhibit clear boundaries and shapes. Yet, compared to CSI-Net, artifacts show up inside the scatterers obtained by CSI.

Table 6.1 provides the corresponding reconstructed errors and SSIM. For all test samples #$1-$#6, CSI-Net generates the lowest reconstruction errors and highest SSIM. In addition, Err_χ, Err_ε and SSIM of all 200 samples obtained by three trained models are displayed in Fig. 6.5 to provide a global view of the reconstruction performance. CSI-Net ensures the lowest average reconstruction errors but also reduces extreme cases, i.e., decreases the variance of reconstruction errors. Inversion error curves of the CSI method are given in Fig. 6.6.

To check on robustness, further simulations are carried out with Gaussian noises of different SNR (20, 10, and $5\,\mathrm{dB}$) added to the scattered fields. In Fig. 6.7, the mean and variance of results obtained with the real-valued circular dataset are displayed. For the mean error, the growth rate of CSI-Net at 20 and $10\,\mathrm{dB}$ is larger than for the two other approaches, yet CSI-Net always exhibits the smallest mean error, i.e., it is robust to noise contamination. As for the variance change, improvement by the proposed method lies not only in better overall reconstruction quality but also in a strong reduction of poor results, i.e., confidence level increases.

In general, a larger training dataset leads to better neural network training. However, in the real world, collecting datasets may not be straightforward. So, a neural network should perform well with a small amount of data. Here, the models are trained with the real-valued circular dataset, and the numbers of training pairs are 250, 500, 1000, 1500, and 2000, respectively. The mean value and variance of Err_χ are displayed in Fig. 6.8. As the training dataset's size increases, the performance of all models improves. But, for a small dataset, U-net performance strongly degrades while CC-ResNet and CSI-Net remain stable. Moreover, CSI-Net consistently outperforms the other two methods.

Evaluations of reliability can be performed by showing that the training dataset is not particularly tuned to

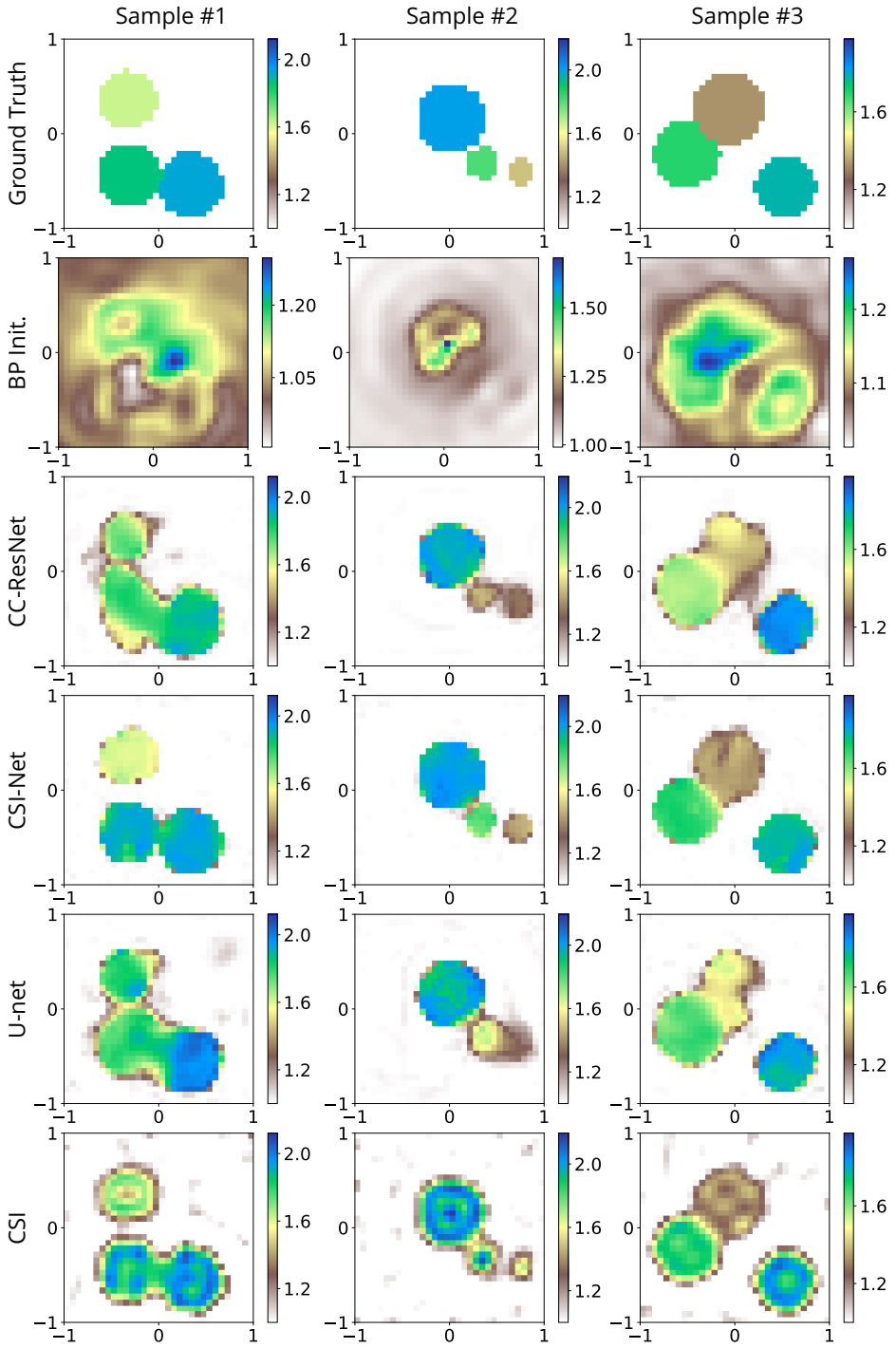

Figure 6.3: Relative permittivity of reconstructed profiles of Samples #1-#3 from the test dataset. The range of relative permittivity is $[1.3, 2]$. Gaussian noise of SNR = $20\,\mathrm{dB}$ is added.

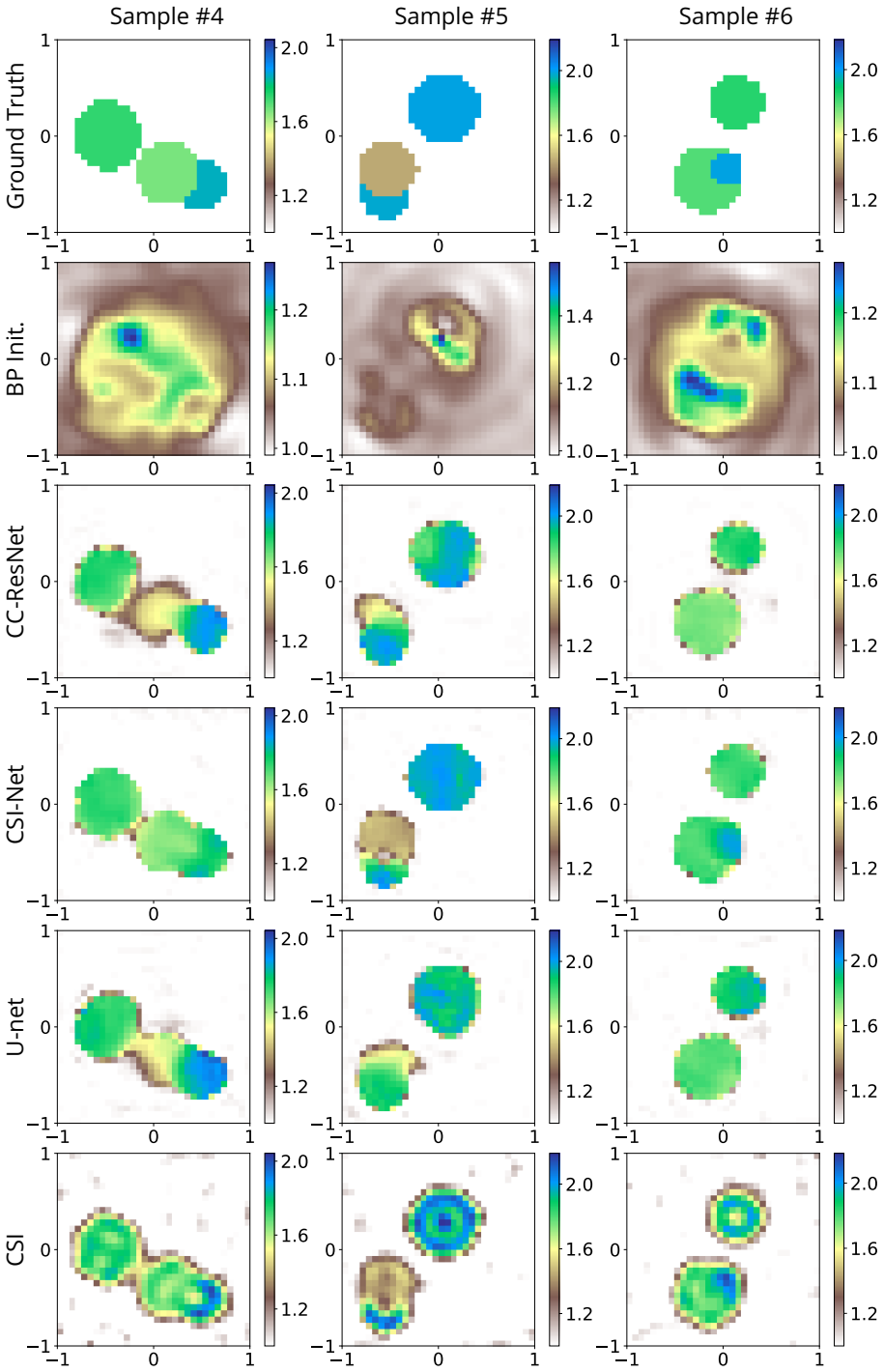

Figure 6.4: Relative permittivity of reconstructed profiles of samples #4-#6 from the test dataset. The range of relative permittivity is $[1.3, 2]$. Gaussian noise of SNR = $20\,\mathrm{dB}$ is added.

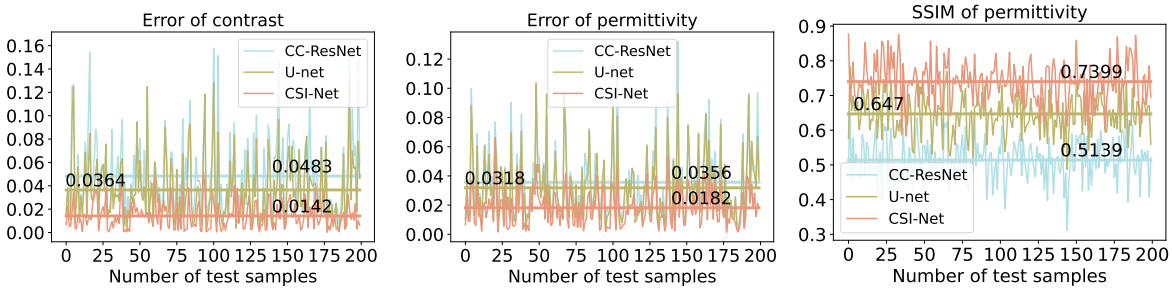

Figure 6.5: Err_χ, Err_ε and SSIM obtained by applying the trained model on 200 test samples. Gaussian noise of SNR = $20\,\mathrm{dB}$ is added to collected fields.

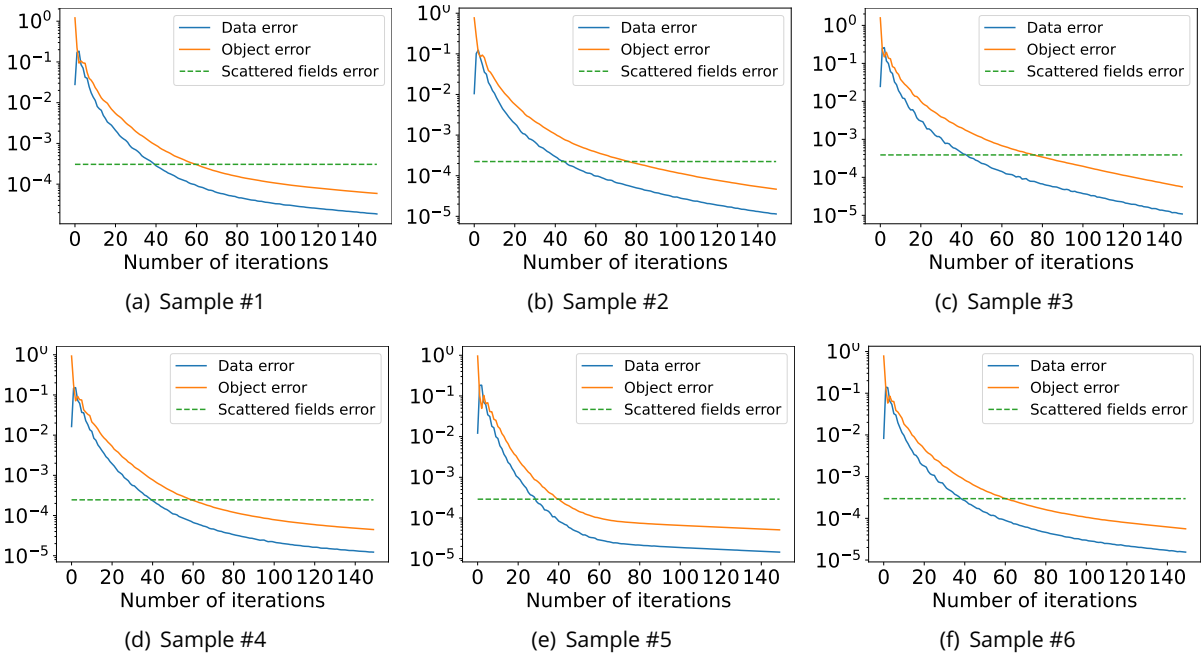

Figure 6.6: Inversion error curves of CSI for samples #1-#6.

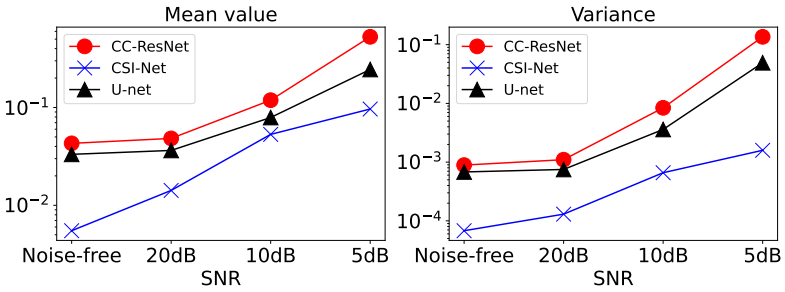

Figure 6.7: Noise stability: mean and variance of Err_χ obtained by CC-ResNet, CSI-Net, and U-net on 200 test samples belonging to the circular database as a function of noise levels.

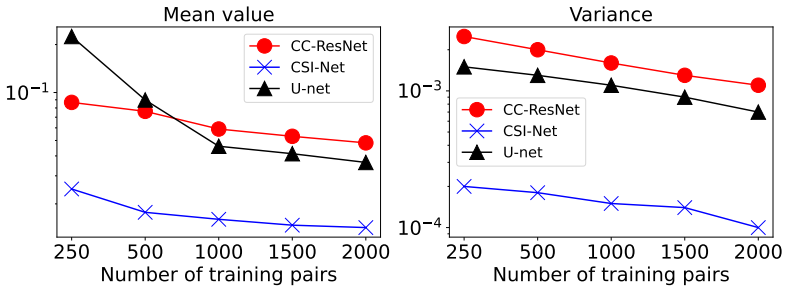

Figure 6.8: Mean and variance of Err_χ obtained by CC-ResNet, CSI-Net and U-net on 200 test samples as a function of the number of training pairs.

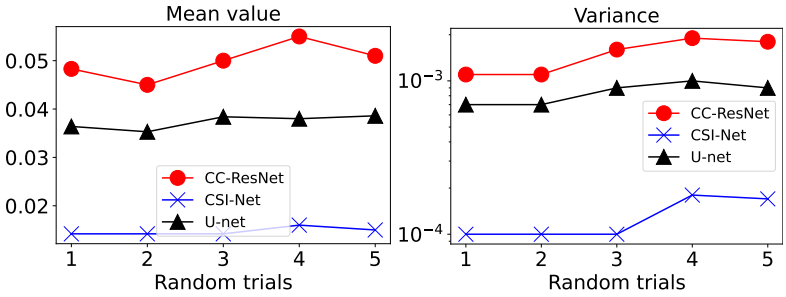

Figure 6.9: Mean and variance of Err_χ obtained by CC-ResNet, CSI-Net, and U-net on 200 test samples using models trained with five randomly chosen datasets of 2000 data pairs.

a proposed network. To this end, a real-valued circular dataset including 5000 samples is used. Five datasets of 2000 data pairs are randomly sampled from the latter as training datasets for the models. Fig. 6.9 illustrates that the performance of the proposed approach remains stable when the dataset changes.

Generalization capability is always an issue, so challenging examples must be considered. The models trained with the circular dataset are now tested on six test samples that are not within the range of the training dataset. The results are in Fig. 6.10 and 6.11. Notice that positivity constraint is enforced in CSI, significantly improving its performance. The number of iterations is set to 200. In particular, samples #7 and #8 are the well-known "Austria" profile with relative permittivity of 1.5 and 2, respectively.

CSI-Net achieves the best reconstruction for most of the samples from #7 to #12. For sample #7, U-net and CC-ResNet only give a rough reconstruction, where the center of the ring is obscured, and the shape is not continuous. For sample #8, where the level of nonlinearity increases, it fails. As for CSI, the retrieved profiles have a smaller size than the true ones. Also, artifacts show up around the edges. For the other samples, U-net and CC-ResNet fail to provide meaningful results and CSI can achieve good results, though with more artifacts than CSI-Net results. The Err_χ of the results are in Table 6.2. They show that CSI-Net has a better generalization capability than U-net and can improve the reconstruction quality of several cases compared to CSI.

6.3.2 Test with MNIST dataset

The proposed model is trained with a different dataset where the scatterers are modeled from the MNIST database (Deng 2012), which contains handwritten digit samples. Digits are transformed to scatterers of random relative permittivity between 2 and 2.5. To increase diversity, a circular/rectangle of random relative permittivity between 2 and 2.5 is added to each sample. The diameters/side lengths are in between $0.3\,\mathrm{m}$ and $0.8\,\mathrm{m}$. The scattering system settings, dataset division, and training hyperparameters are un-

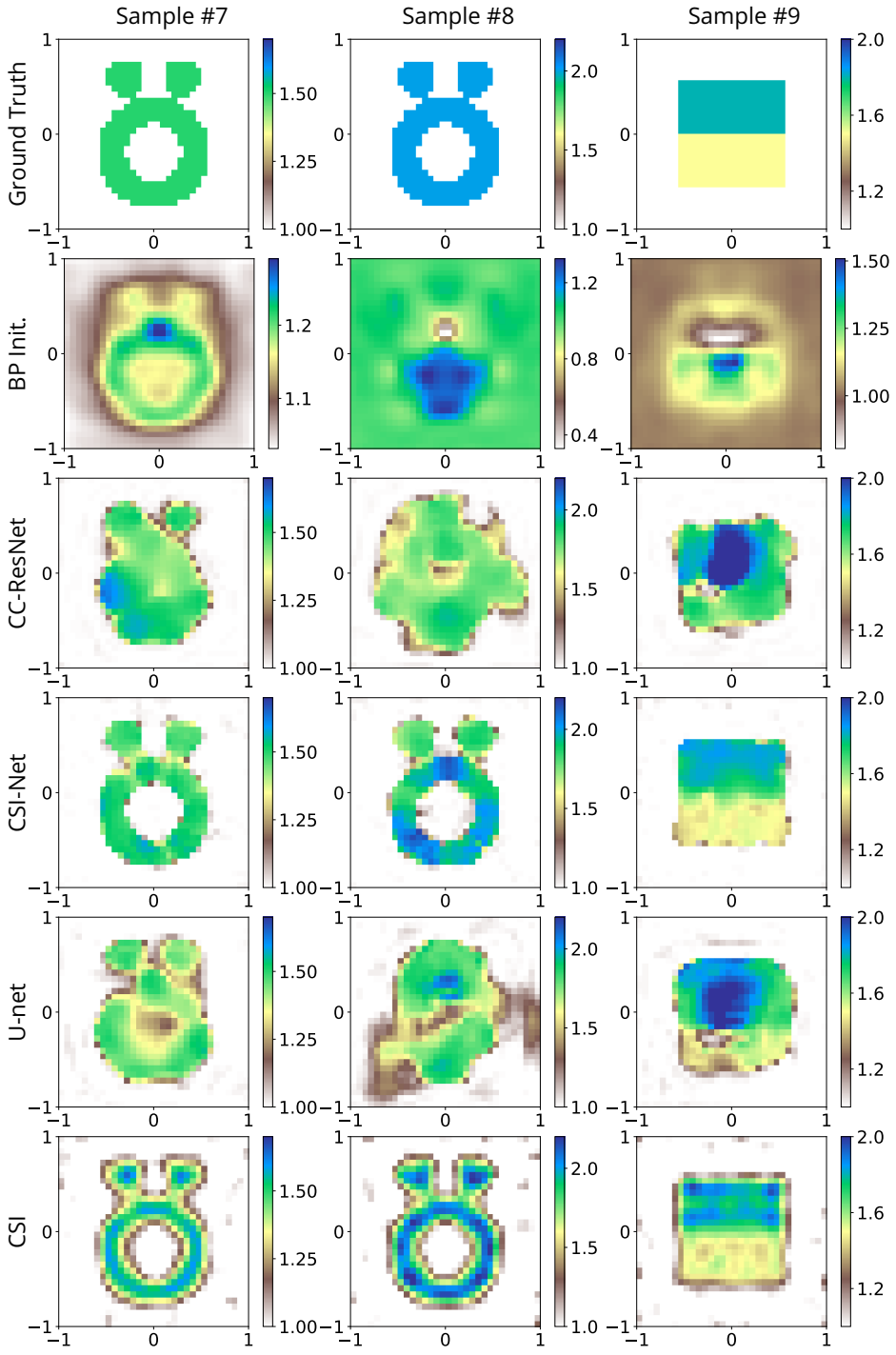

Figure 6.10: Reconstructed relative permittivity of samples #7-#9 obtained by three models and CSI. The models are trained with the circular dataset. The test dataset lies outside the range of training data. $20\,\mathrm{dB}$ Gaussian noise affects the collected scattered fields.

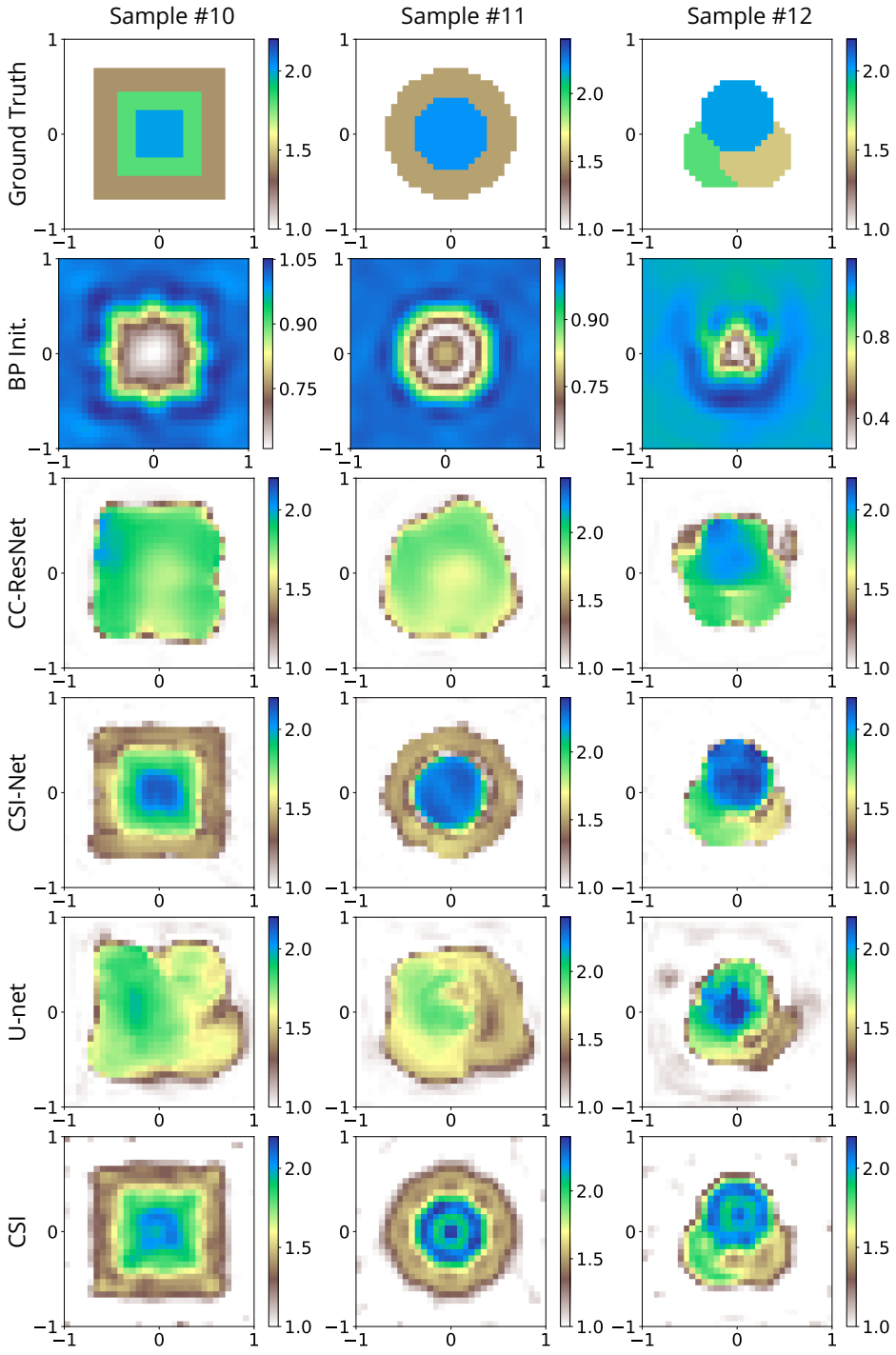

Figure 6.11: Reconstructed relative permittivity of samples #10-#12 obtained by three models and CSI. The models are trained with the circular dataset. The test dataset lies outside the range of training data. $20\,\mathrm{dB}$ Gaussian noise affects the collected scattered fields.

Table 6.2: Err_χ of Test samples #7-#12. SNR = $20\,\mathrm{dB}$

Model	Sample #7	#8	#9	#10	#11	#12
CC-ResNet	0.368	0.596	0.191	0.277	0.282	0.176
CSI-Net	**0.038**	0.095	**0.023**	**0.024**	**0.029**	0.052
U-net	0.236	0.477	0.157	0.182	0.235	0.101
CSI	0.098	**0.093**	0.036	**0.024**	0.031	**0.034**

Table 6.3: Err_χ of Test samples #13-#18, and 200 test samples. SNR = $20\,\mathrm{dB}$

Model	Sample #13	#14	#15	#16	#17	#18	Mean	Variance
CSI-Net	**0.073**	**0.064**	**0.096**	**0.059**	**0.105**	**0.218**	**0.047**	**0.0004**
U-net	0.249	0.197	0.219	0.162	0.146	0.244	0.097	0.0014

changed.

The trained models are tested on 200 samples within the same range of the training dataset. As shown in Fig. 6.12, samples #13-#16 are four representative samples among the test dataset, and #17-#18 are "Austria" profiles with relative permittivities of 2.5 and 3, respectively. Due to strong nonlinearity, CSI fails to reconstruct all samples, so its results are not displayed. CC-ResNet is not included since all of its results are worse than CSI-Net. U-net can roughly reconstruct the profiles, however, most details are missing. In comparison, CSI-Net achieves better reconstructions for all test samples.

The Err_χ of these test samples obtained by different methods are presented in Table 6.3. Note that its last two columns give the mean value and the variance of Err_χ across all 200 test samples. We can conclude from above results that CSI-Net works better than other methods for the cases where the nonlinearity increases.

6.3.3 Test with lossy scatterers

All previous results are on lossless scatterers. The proposed model is now trained with a complex-valued circular dataset to represent lossy scatterers. The training dataset shares the same key parameters as the real-valued one except for the relative permittivity value. Real parts of relative permittivities are between 1.3 and 2.4; imaginary parts vary from 0 to 1.2. The trained model is tested on the "Austria" profile, and the results are in Fig. 6.13. Both CSI-Net and CSI exhibit satisfactory results. On the contrary, U-net fails to reconstruct the ring for both real and imaginary parts. Corresponding Err_χ are in Table 6.4. The last two rows give the mean error and variance over 200 test samples.

Table 6.4: Mean and variance of Err_χ over 200 test samples. SNR = $20\,\mathrm{dB}$.

Model	CSI-Net	U-net	CSI
"Austria"	**0.131**	0.269	0.157
Mean	**0.021**	0.040	\
Variance	**0.0004**	0.0011	\

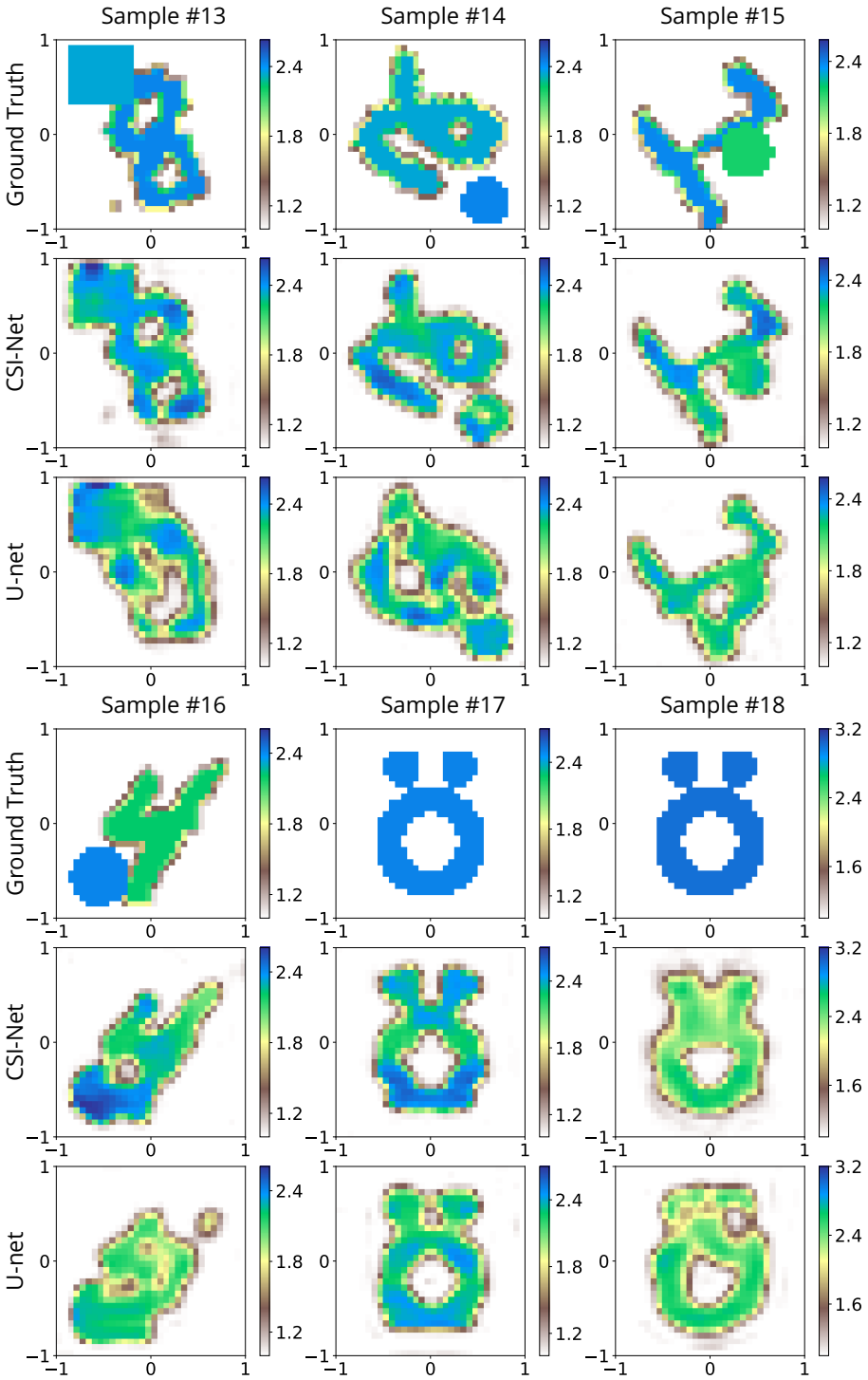

Figure 6.12: Reconstructed relative permittivity obtained by CSI-Net, U-net (CSI and CC-ResNet have been omitted since failing to yield proper reconstruction). The models are trained with the MNIST dataset. The test dataset is outside the range of training data. $20\,\mathrm{dB}$ Gaussian noise affects the collected scattered fields.

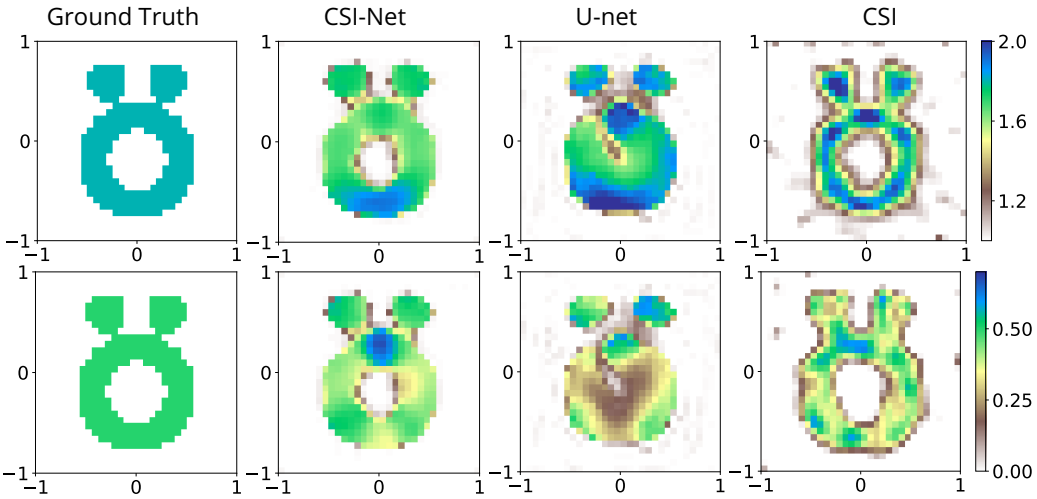

Figure 6.13: Reconstructed relative permittivity obtained by models trained with a complex-valued circular dataset. $\Re\{\varepsilon\}$ (top) of ground truth is 1.8 and $\Im\{\varepsilon\}$ (bottom) is 0.5. 20 dB Gaussian noise affects the collected scattered fields.

6.4 Extension of CSI-Net to multi-frequency data

The frequency hopping approach (Chew and Lin 1995) (Bucci *et al.* 2000) is a popular technique to improve reconstruction performance reached with the monochromatic data.

Using multi-frequency data has the following advantages:

- First of all, even if the problem is still ill-posed, another type of relation is treated, which improves the accuracy of the reconstruction.
- Second, the use of multi-frequency data reduces ill-conditioning (i.e., improves local stability) of the reconstruction process.
- Third, robustness against false solutions is improved.

In this section, we apply the frequency-hopping technique to improve CSI-Net. The recurrent network structure of CSI-Net makes it naturally suitable for applying the frequency hopping technique. For different sub-blocks, we input data of different frequencies. First, a reliable starting guess can be obtained with low-frequency data. Next, the results are used for the following inversion steps performed at higher frequencies. Denote CSI-Net in the multi-frequency scheme as CSI-Net-MF.

Take a CSI-Net that contains 4 sub-blocks (exactly the same structure as that in previous sections), for each sub-block, we input the data at a fixed frequency. Here, we use data obtained at 4 frequencies: $100\,\mathrm{MHz}$, $200\,\mathrm{MHz}$, $400\,\mathrm{MHz}$, and $600\,\mathrm{MHz}$.

To evaluate the performance of the CSI-Net-MF, we apply it to a more complicated dataset that contains profiles of higher nonlinearity. The error of permittivity Err_ε is used here to quantitatively evaluate the reconstruction quality. A synthetically generated lossless circular dataset is used. Each sample contains disks of random quantities: number ($1 \sim 3$), relative permittivity ($2.5 \sim 3.5$), radius ($0.15\,\mathrm{m} \sim 0.4\,\mathrm{m}$), and location. The scatterers may overlap. The collected fields used for training are noise-free. The dataset comprises 2500 samples. Among them, 2000 are employed for training, 300 for validation, and 200 for testing. Hyperparameters settings are the same as in previous sections.

Illustrative results are shown in Fig. 6.14. These profiles have higher relative permittivity, resulting in stronger nonlinearity of the inverse problem and more difficult object reconstruction. Due to the use of

multi-frequency data, we can observe that the CSI-Net-MF outperforms CSI-Net in the monochromatic case. Relative permittivity errors of six samples and the mean value over 200 test samples shown in Table 6.5 confirm it.

Table 6.5: $\mathrm{Err}_{\varepsilon}$ of Test samples #1-#6, and 200 test samples. SNR = $20\,\mathrm{dB}$

Model	Sample #1	#2	#3	#4	#5	#6	Mean
CSI-Net-MF	**0.102**	**0.101**	**0.118**	**0.118**	**0.071**	**0.062**	**0.0551**
CSI-Net	0.201	0.208	0.220	0.613	0.236	0.232	0.134

6.5 Conclusion

To conclude, the proposed CSI-Net can combine the advantages of traditional iterative algorithms and learning approaches. It has a good generalization ability. Moreover, it can improve the confidence level of the results by integrating the domain knowledge into the learning process. The results obtained by the proposed model are more reliable that a black box network. Last but not least, due to the recurrent network structure of the proposed model, it is naturally suitable to be extended to an multi-frequency scheme.

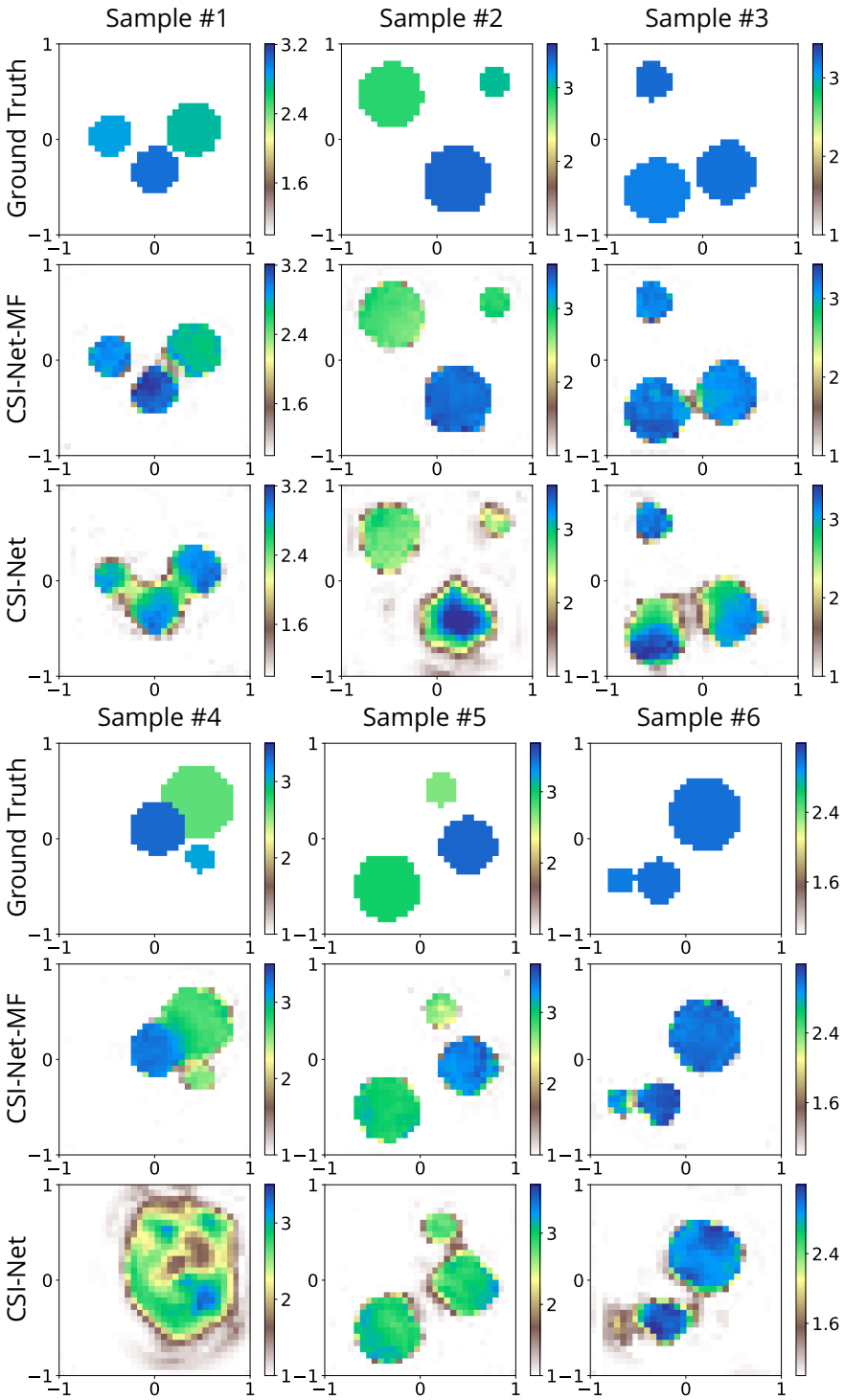

Figure 6.14: Reconstructed relative permittivity obtained by CSI-Net-MF and CSI-Net. $20\,\mathrm{dB}$ Gaussian noise affects the collected scattered fields.

7 Conclusion and perspectives

7.1 Conclusion

In this thesis, two-dimensional full-wave nonlinear electromagnetic inverse scattering problems (ISPs) are investigated. The aim is the retrieval of the characteristics of an unknown scatterer or set of scatterers illuminated by given incident fields from the knowledge of the fields it or they scatter. The proposed methods can mainly be classified into two parts: the traditional optimization methods and the learning-based method. For traditional methods, the discrete wavelet transform and mixed sparse regularization are combined with the contrast source inversion (CSI) method, while the learning-based method consists in combining convolutional neural networks (CNN) and the CSI method through a so-called unrolled scheme.

In the first part, the CSI method is combined with the conventional 2-D discrete wavelet transform. One attractive property of the wavelet transform is that it can provide a multiresolution representation for a given signal. By transforming the contrast function into the wavelet domain with a given wavelet basis, wavelet coefficients of different levels can be obtained, which correspond to different frequency resolutions. Wavelet coefficients can be divided into two parts: approximation coefficients and detail coefficients. Approximation coefficients contain low-frequency components and thus are more robust to noise. A multiscale wavelet-based CSI is proposed, combining the multiresolution property and the characteristics of approximation wavelet coefficients. Simulations are carried out on different configurations and with diverse wavelet bases to compare the performance of CSI and of the proposed method.

In addition to the multiresolution property of the wavelet coefficients, the sparsity of wavelet detail coefficients also attracts considerable attention. So, to alleviate the ill-posedness of the ISPs, a sparsity penalization is added to the cost function of the CSI method, and a group sparsity penalized CSI method is proposed. Instead of employing the widely-used ℓ_1 norm to impose the sparsity constraint, here, a mixed norm $\ell_{2,1}$ norm is used to impose the so-called group sparsity.

The conventional discrete wavelet transform used in the first method is replaced with the dual-tree complex wavelet transform, which makes it possible to represent the contrast function in a sparse manner and yields the structure information of the contrast. When solving the optimization problem with group sparsity regularization, three grouping strategies are investigated to build overlapping sub-groups, while the replication approach and proximal gradient descent algorithm are used to minimize the cost function. Numerical simulations are carried out on different configurations, and comparisons are conducted to exhibit the pros and cons of the proposed methodology.

In the second part, the deep learning technique is applied to solve ISPs. Deep learning has achieved great success in dealing with computer vision tasks but has not produced a profound impact on the solutions of such ISPS yet. In our work, CNN is combined with the CSI method, and an unrolled network structure is designed. The domain knowledge is incorporated in an effective manner into the learning process by embedding CSI iterations into the network structure. Furthermore, due to the iterative architecture of the

network, the proposed model can be easily extended to the multi-frequency scheme. Thorough numerical tests are carried out to evaluate the performance of our model, and the stability, robustness, and reliability of the proposed approach are also analyzed. Comparisons with the widely used U-net structure and CSI illustrate the advantage of the proposed method.

To summarize, one has developed and investigated both traditional optimization methods and learning-based methods for solving 2-D full wavelet ISPs. The multi-scale wavelet-based CSI and group sparsity penalized CSI methods show their advantages when tackling problems with insufficient collected data. As for the learning-based method, it enables real-time reconstruction and it benefits from the information contained in large-scale data. By combining CSI and CNN, the reliability of the model is improved, something which is still a matter of concern for learning-based methods.

7.2 Perspectives

In this thesis, several methods including traditional optimization approaches and learning approaches have been investigated. However, further explorations appear of good interest.

Traditional optimization methods

- In the multi-scale wavelet-based CSI method, the inversion starts from the finest decomposition level to the coarsest decomposition level. That is, several successive inversion steps are required throughout the optimization process. The present work sets a fixed number of iterations for each inversion step. The optimization involves only a few coefficients for the first inversion steps, so fewer iterations are required to converge. Therefore, the number of iterations needed for each inversion step is different. Further research should be done to define more flexible stopping criteria to eliminate unnecessary iterations.

  Haar and Daubechies' wavelet family are chosen to decompose the unknown object in the present work. However, the optimal choice of the wavelet basis depends on different problems. More research can be carried out to deduce which wavelet basis function can be the most suitable for specific application areas.
- In the group sparsity penalized CSI method, three grouping strategies are proposed to form different sub-groups of wavelet coefficients, based on which group sparsity penalization is applied. Instead of using pre-defined group arrangements, the hidden Markov tree (HMT) model can be employed to dynamically detect the wavelet support at iteration (Deka *et al.* 2018).

  This method focuses on the structural information contained in the wavelet detail coefficients. Images with more detail information should benefit better from this approach. Therefore, it would make sense to apply this approach to other models, such as breast models in biomedical imaging.
- Multi-scale wavelet-based CSI method and group sparsity penalized CSI method concentrate on approximation wavelet coefficients and detail wavelet coefficients, respectively. The combination of the two approaches is of good interest.

Learning method

- As for what concerns the CSI-Net, the step size of the CSI algorithm is not a learnable parameter. Therefore, several CSI iterations are embedded into each sub-block to speed up the convergence.

Making the step size a learnable parameter is a path ahead, since it makes it possible to simplify the network structure.

- As emphasized already, incorporating physical information into the deep learning model is of great importance. Physical information can be integrated into the model not only through pre-initialized inputs and network structures but also through modifications to the loss function. The loss function used in the current work can be further modified by adding data misfitting terms obtained from domain knowledge, as proposed in (Liu, Roy, *et al.* 2022).

Other potential work

- All proposed methods are still limited to 2-D configurations and in the standard scalar TM polarization case. Investigations of vector 3-D cases where mathematical modeling is more complicated, and nonlinearity and ill-posedness become more severe, should be carried out.
- The proposed methods are only tested on simulation data. More tests should be carried out on experimental data at first in laboratory-controlled situations.

A Orthogonal Daubechies coefficients

(a) Coefficients of the scaling functions for D2-10

D2(Haar)	D4	D6	D8	D10	D12
1	0.683 012 7	0.470 467 21	0.325 803 43	0.226 418 98	0.157 742 43
1	1.183 012 7	1.141 116 92	1.010 945 72	0.853 943 54	0.699 503 81
	0.316 987 3	0.650 365	0.892 200 14	1.024 326 94	1.062 263 76
	−0.183 012 7	−0.190 934 42	−0.039 575 03	0.195 766 96	0.445 831 32
		−0.120 832 21	−0.264 507 17	−0.342 656 71	−0.319 986 60
		0.049 817 5	0.043 616 3	−0.045 601 13	−0.183 518 06
			0.046 503 6	0.109 702 65	0.137 888 09
			−0.014 986 99	−0.008 826 80	0.038 923 21
				−0.017 791 87	−0.044 663 75
				$4.717\,427\,93 \times 10^{-3}$	$7.832\,511\,52 \times 10^{-4}$
					$6.756\,062\,36 \times 10^{-3}$
					$-1.523\,533\,81 \times 10^{-3}$

(b) Coefficients of the scaling functions for D12-20

D14	D16	D18	D20
0.110 099 43	0.076 955 62	0.053 850 35	0.037 717 16
0.560 791 28	0.442 467 25	0.344 834 30	0.266 122 18
1.031 148 49	0.955 486 15	0.855 349 06	0.745 575 07
0.664 372 48	0.827 816 53	0.929 545 71	0.973 628 11
−0.203 513 82	−0.022 385 74	0.188 369 55	0.397 637 74
−0.316 835 01	−0.401 658 63	−0.414 751 76	−0.353 336 20
0.100 846 7	$6.681\,940\,92 \times 10^{-4}$	−0.136 953 55	−0.277 109 88
0.114 003 45	0.182 076 36	0.210 068 34	0.180 127 45
−0.053 782 45	−0.024 563 90	0.043 452 675	0.131 602 99
−0.023 439 94	−0.062 350 21	−0.095 647 26	−0.100 966 57
0.017 749 79	0.019 772 16	$3.548\,928\,13 \times 10^{-4}$	−0.041 659 25
$6.075\,149\,95 \times 10^{-4}$	0.012 368 84	0.031 624 17	0.046 969 81
$-2.547\,904\,72 \times 10^{-3}$	$-6.887\,719\,26 \times 10^{-3}$	$-6.679\,620\,23 \times 10^{-3}$	$5.100\,436\,97 \times 10^{-3}$
$5.002\,268\,53 \times 10^{-4}$	$-5.540\,045\,49 \times 10^{-4}$	$-6.054\,960\,58 \times 10^{-3}$	−0.015 179 00
	$9.552\,297\,11 \times 10^{-4}$	$2.612\,967\,28 \times 10^{-3}$	$1.973\,325\,36 \times 10^{-3}$
	$-1.661\,372\,61 \times 10^{-4}$	$3.258\,146\,71 \times 10^{-4}$	$2.817\,686\,59 \times 10^{-3}$
		$-3.563\,297\,59 \times 10^{-4}$	$-9.699\,478\,40 \times 10^{-4}$
		$5.564\,551\,4 \times 10^{-5}$	$-1.647\,090\,06 \times 10^{-4}$
			$1.323\,543\,67 \times 10^{-4}$
			$-1.875\,841 \times 10^{-5}$

Table A.1

B U-net structure

The U-net structure, originally designed for medical image segmentation, is widely used for ISPs (as in (Wei *et al.* 2019a; Liu, Roy, *et al.* 2022) among many). For comparison, a U-net structure adapted to our work is proposed, and the results are displayed. Details of U-net can be found in (Ronneberger *et al.* 2015). Fig. B.1 shows the network structure in the present work.

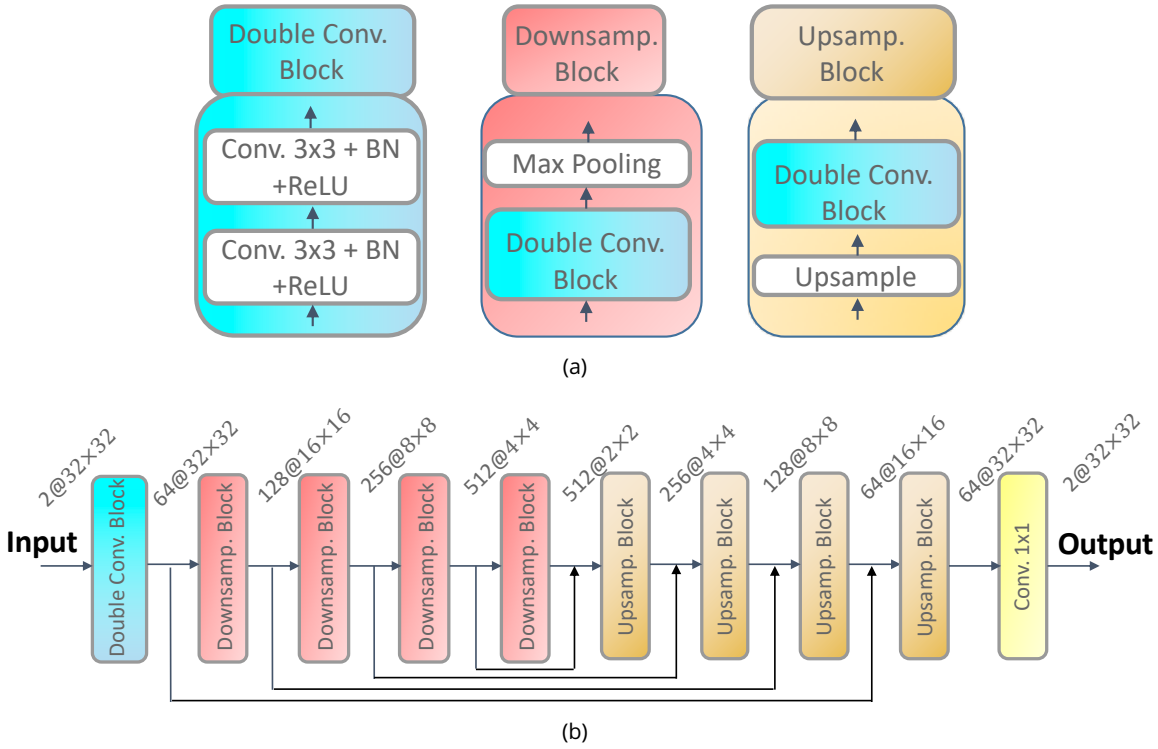

Figure B.1: The U-net structure used in our work. The dimension of the feature maps passing through each layer is noted as $[\text{Number of channels}@H \times W]$.

C List of publications

- Articles dans des revues internationales à comité de lecture

  1. Y. Zhang, M. Lambert, A. Fraysse, and D. Lesselier (2021). "Group Sparsity Penalized Contrast Source Solution Method for 2-D Non-linear Inverse Scattering". *IEEE Open J. Antennas Propag.* 3, pp. 48–58. doi: 10.1109/OJAP.2021.3133450
  2. Y. Zhang, M. Lambert, A. Fraysse, and D. Lesselier (2022). "Unrolled Convolutional Neural Network for Full-Wave Inverse Scattering". *IEEE Trans. Antennas Propag.(Early Access)*, pp. 1–9. doi: 10.1109/TAP.2022.3216999

- Articles dans des conférences internationales à comité de lecture avec actes

  1. Y. Zhang, A. Fraysse, M. Lambert, and D. Lesselier (2021a). "A Wavelet-based Contrast Source Inversion Method". *IEEE 19th International Symposium on Antenna Technology and Applied Electromagnetics (ANTEM)*. Winnipeg, Canada, pp. 1–2. doi: 10.1109/ANTEM51107.2021.9518522
  2. Y. Zhang, A. Fraysse, M. Lambert, and D. Lesselier (2021b). "Use of Sparsity in Nonlinear Electromagnetic Imaging". *XXXIV General Assembly and Scientific Symposium (GASS) of the International Union of Radio Science*. Rome, Italie

Bibliography

Abdelnour, A. and I. Selesnick (2004). "Symmetric Nearly Orthogonal and Orthogonal Nearly Symmetric Wavelets". English (US). *Arab J Sci Eng* 29.2 C, pp. 3–16 (cit. on p. 28).

Aggarwal, H. K., M. P. Mani, and M. Jacob (2019). "Modl: Model-based Deep Learning Architecture for Inverse Problems". *IEEE Trans. Med. Imaging* 38.2, pp. 394–405. doi: 10.1109/TMI.2018.2865356 (cit. on p. 51).

Alexopoulos, N. G., C. A. Kyriazidou, and H. F. Contopanagos (2007). "Effective Parameters for Metamorphic Materials and Metamaterials through a Resonant Inverse Scattering Approach". *IEEE Trans. Microwave Theory Tech.* 55.2, pp. 254–267. doi: 10.1109/TMTT.2006.890074 (cit. on pp. x, 1).

Anselmi, N., M. Salucci, G. Oliveri, and A. Massa (2015). "Wavelet-based Compressive Imaging of Sparse Targets". *IEEE Trans. Antennas Propagat.* 63.11, pp. 4889–4900. doi: 10.1109/TAP.2015.2444423 (cit. on p. 25).

Azghani, M., P. Kosmas, and F. Marvasti (2015). "Microwave Medical Imaging Based on Sparsity and an Iterative Method with Adaptive Thresholding". *IEEE Trans. Med. Imaging* 34.2, pp. 357–365. doi: 10.1109/TMI.2014.2352113 (cit. on p. 24).

Azghani, M. and F. Marvasti (2013). "Iterative Algorithms for Random Sampling and Compressed Sensing Recovery". *Proceedings of the 10th International Conference on Sampling Theory and Applications*, pp. 182–185 (cit. on p. 24).

Bach, F., R. Jenatton, J. Mairal, and G. Obozinski (2012). "Optimization with Sparsity-inducing Penalties". *Foundations and Trends in Machine Learning* 4.1, pp. 1–106. doi: 10.1561/2200000015 (cit. on p. 3).

Baraniuk, R. G. (1999). "Optimal tree approximation with wavelets". *Wavelet Applications in Signal and Image Processing VII*. Ed. by M. A. Unser, A. Aldroubi, and A. F. Laine. Vol. 3813. International Society for Optics and Photonics. SPIE, pp. 196–207. doi: 10.1117/12.366780 (cit. on p. 25).

Beck, A. and M. Teboulle (2009). "A Fast Iterative Shrinkage-thresholding Algorithm for Linear Inverse Problems". *SIAM J. Imaging Sci.* 2.1, pp. 183–202. doi: 10.1137/080716542. eprint: https://doi.org/10.1137/080716542 (cit. on p. 24).

Berg, P. M. van den, A. L. van Broekhoven, and A. Abubakar (1999). "Extended Contrast Source Inversion". *Inverse Prob.* 15.5, pp. 1325–1344. doi: 10.1088/0266-5611/15/5/315 (cit. on p. 24).

Bevacqua, M. T., L. Crocco, L. D. Donato, and T. Isernia (2017). "Non-linear Inverse Scattering Via Sparsity Regularized Contrast Source Inversion". *IEEE Trans. Comput. Imaging* 3.2, pp. 296–304. doi: 10.1109/TCI.2017.2675708 (cit. on p. 25).

Boyd, S., S. P. Boyd, and L. Vandenberghe (2004). *Convex Optimization*. Cambridge University Press (cit. on p. 32).

Bracewell, R. N. and R. N. Bracewell (1986). *The Fourier Transform and Its Applications*. Vol. 31999. McGraw-Hill New York (cit. on p. 13).

Bucci, O. M., L. Crocco, T. Isernia, and V. Pascazio (2000). "Inverse Scattering Problems with Multifrequency Data: Reconstruction Capabilities and Solution Strategies". *IEEE Trans. Geosci. Remote Sensing* 38.4, pp. 1749–1756 (cit. on p. 75).

Busch, P., T. Heinonen, and P. Lahti (2007). "Heisenberg's Uncertainty Principle". *Phys. Rep.* 452.6, pp. 155–176 (cit. on p. 13).

Buzug, T. M. (2011). "Computed Tomography". *Springer Handbook of Medical technology*. Springer, pp. 311–342 (cit. on pp. x, 1).

Campisi, P. and K. Egiazarian (2017). *Blind Image Deconvolution: Theory and Applications*. CRC press (cit. on pp. x, 1).

Chen, C. and J. Huang (2014). "The Benefit of Tree Sparsity in Accelerated MRI". *Med. Image Anal.* 18.6. Sparse Methods for Signal Reconstruction and Medical Image Analysis, pp. 834–842. doi: 10.1016/j.media.2013.12.004 (cit. on pp. 34, 36).
Chen, X. (2010). "Subspace-based Optimization Method for Solving Inverse-scattering Problems". *IEEE Trans. Geosci. Remote Sensing* 48.1, pp. 42–49. doi: 10.1109/TGRS.2009.2025122 (cit. on p. 4).
Chen, X. (2018). *Computational Methods for Electromagnetic Inverse Scattering*. Wiley-IEEE Press, Singapore. doi: 10.1002/9781119311997.fmatter (cit. on pp. x, 1).
Chen, X., Z. Wei, M. Li, and P. Rocca (2020). "A Review of Deep-learning Approaches for Inverse Scattering Problems (invited Review)". *Prog. Electromagn. Res.* 167, pp. 67–81. doi: 10.2528/PIER20030705 (cit. on p. 61).
Chew, W. and Y. Wang (1990). "Reconstruction of Two-dimensional Permittivity Distribution Using the Distorted Born Iterative Method". *IEEE Trans. Med. Imaging* 9.2, pp. 218–225. doi: 10.1109/42.56334 (cit. on p. 4).
Chew, W. C. and J. Lin (1995). "A Frequency-hopping Approach for Microwave Imaging of Large Inhomogeneous Bodies". *IEEE Microw. Guided Wave Lett.* 5.12, pp. 439–441 (cit. on p. 75).
Choi, H., J. Romberg, R. Baraniuk, and N. Kingsbury (2000). "Hidden Markov Tree Modeling of Complex Wavelet Transforms". *2000 IEEE International Conference on Acoustics, Speech, and Signal Processing. Proceedings*. Vol. 1, 133–136 vol.1. doi: 10.1109/ICASSP.2000.861889 (cit. on p. 31).
Chui, C. (1992). *An Introduction to Wavelets*. Vol. 1. doi: 10.2307/2153134 (cit. on p. 14).
Crouse, M., R. Nowak, and R. Baraniuk (1998). "Wavelet-based Statistical Signal Processing Using Hidden Markov Models". *IEEE Trans. Signal Processing* 46.4, pp. 886–902. doi: 10.1109/78.668544 (cit. on p. 30).
Cui, Z., H. Chang, S. Shan, B. Zhong, and X. Chen (2014). "Deep Network Cascade for Image Super-resolution". *Computer Vision – ECCV 2014*. Ed. by D. Fleet, T. Pajdla, B. Schiele, and T. Tuytelaars. Cham: Springer International Publishing, pp. 49–64 (cit. on pp. 3, 51).
Curry, H. B. (1944). "The Method of Steepest Descent for Non-linear Minimization Problems". *Q Appl Math* 2.3, pp. 258–261 (cit. on p. 2).
Dai, Y.-H. and Y. Yuan (1999). "A Nonlinear Conjugate Gradient Method with a Strong Global Convergence Property". *SIAM J. Optim.* 10.1, pp. 177–182 (cit. on p. 2).
Davidson, D. B. (2005). "Computational Electromagnetics for RF and Microwave Engineering" (cit. on p. 8).
Deka, B., S. Datta, and S. Handique (2018). "Wavelet Tree Support Detection for Compressed Sensing MRI Reconstruction". *IEEE Signal Processing Lett.* 25.5, pp. 730–734. doi: 10.1109/LSP.2018.2824251 (cit. on pp. xvii, 79).
Deng, L. (2012). "The MNIST Database of Handwritten Digit Images for Machine Learning Research". *IEEE Signal Processing Mag.* 29.6, pp. 141–142 (cit. on p. 70).
Desmal, A. and H. Bağcı (2014). "Shrinkage-thresholding Enhanced Born Iterative Method for Solving 2D Inverse Electromagnetic Scattering Problem". *IEEE Trans. Antennas Propagat.* 62.7, pp. 3878–3884. doi: 10.1109/TAP.2014.2321144 (cit. on p. 24).
Devaney, A. J. (1981). "Inverse-scattering Theory within the Rytov Approximation". *Opt Lett* 6.8, pp. 374–376. doi: 10.1364/OL.6.000374 (cit. on p. 3).
Devaney, A. J. (1982). "Inversion Formula for Inverse Scattering within the Born Approximation". *Opt Lett* 7.3, pp. 111–112. doi: 10.1364/OL.7.000111 (cit. on p. 4).
Diamond, S., V. Sitzmann, F. Heide, and G. Wetzstein (2017). "Unrolled Optimization with Deep Priors". *ArXiv* abs/1705.08041 (cit. on p. 59).

Donoho, D. L. (2006). “For Most Large Underdetermined Systems of Linear Equations the Minimal ℓ_1–norm Solution Is Also the Sparsest Solution”. *Commun. Pure Appl. Math.* 59.6, pp. 797–829. doi: 10.1002/cpa.20132. eprint: https://onlinelibrary.wiley.com/doi/pdf/10.1002/cpa.20132 (cit. on p. 3).

Engl, H. W., M. Hanke, and A. Neubauer (2000). *Regularization of Inverse Problems*. Vol. 375. Mathematics and Its Applications. Springer Netherlands (cit. on p. 2).

Goodfellow, I., J. Pouget-Abadie, M. Mirza, B. Xu, D. Warde-Farley, S. Ozair, A. Courville, and Y. Bengio (2014). “Generative Adversarial Nets”. *Advances in Neural Information Processing Systems*. Ed. by Z. Ghahramani, M. Welling, C. Cortes, N. Lawrence, and K. Q. Weinberger. Vol. 27. Curran Associates, Inc. (cit. on p. 4).

Hartley, H. O. (1961). “The Modified Gauss-Newton Method for the Fitting of Non-linear Regression Functions by Least Squares”. *Technometrics* 3.2, pp. 269–280 (cit. on p. 2).

He, K., X. Zhang, S. Ren, and J. Sun (2015). “Delving Deep into Rectifiers: Surpassing Human-level Performance on Imagenet Classification”. *Proceedings of the IEEE International Conference on Computer Vision*, pp. 1026–1034 (cit. on p. 56).

He, K., X. Zhang, S. Ren, and J. Sun (2016). “Deep Residual Learning for Image Recognition”. *2016 IEEE Conference on Computer Vision and Pattern Recognition (CVPR)*, pp. 770–778. doi: 10.1109/CVPR.2016.90 (cit. on p. 62).

Horn, R. A. and C. R. Johnson (1985). “Norms for Vectors and Matrices”. *Matrix Analysis*. Cambridge University Press, pp. 257–342. doi: 10.1017/CBO9780511810817.007 (cit. on p. 3).

Ida, N. and N. Meyendorf (2019). *Handbook of Advanced Nondestructive Evaluation*. Springer Cham, Switzerland. doi: 10.1007/978-3-319-26553-7 (cit. on pp. x, 1).

Ioffe, S. and C. Szegedy (2015). “Batch Normalization: Accelerating Deep Network Training by Reducing Internal Covariate Shift”. *International conference on machine learning*. PMLR, pp. 448–456 (cit. on p. 55).

Jacob, L., G. Obozinski, and J.-P. Vert (2009). “Group Lasso with Overlap and Graph Lasso”. *Proceedings of the 26th Annual International Conference on Machine Learning*. ICML ’09. Montreal, Quebec, Canada: Association for Computing Machinery, pp. 433–440. doi: 10.1145/1553374.1553431 (cit. on p. 34).

Jenatton, R., J. Mairal, G. Obozinski, and F. Bach (2011). “Proximal Methods for Hierarchical Sparse Coding”. *J. Mach. Learn. Res.* 12, pp. 2297–2334 (cit. on p. 34).

Jin, K. H., M. T. McCann, E. Froustey, and M. Unser (2017). “Deep Convolutional Neural Network for Inverse Problems in Imaging”. *IEEE Trans. Image Processing* 26.9, pp. 4509–4522. doi: 10.1109/TIP.2017.2713099 (cit. on pp. 3, 51, 60).

Kingma, D. P. and J. Ba (2015). “Adam: A Method for Stochastic Optimization”. *Proceedings of the International Conference on Learning Representations (ICLR)*. San Diego, CA, USA. doi: 10.48550/arXiv.1412.6980 (cit. on p. 65).

Kingsbury, N. (2000). “A Dual-tree Complex Wavelet Transform with Improved Orthogonality and Symmetry Properties”. *Proceedings 2000 International Conference on Image Processing*. Vol. 2. Vancouver, BC, Canada, pp. 375–378. doi: 10.1109/ICIP.2000.899397 (cit. on p. 28).

Kleinman, R. and P. den Berg (1992). “A Modified Gradient Method for Two- Dimensional Problems in Tomography”. *J Comput Appl Math* 42.1, pp. 17–35. doi: 10.1016/0377-0427(92)90160-Y (cit. on p. 11).

Kowalski, M. (2009). “Sparse Regression Using Mixed Norms”. *Appl Comput Harmon A* 27.3, pp. 303–324. doi: 10.1016/j.acha.2009.05.006 (cit. on pp. 3, 25, 34).

LeCun, Y., Y. Bengio, and G. Hinton (2015). “Deep Learning”. *Nature* 521, pp. 436–44. doi: 10.1038/nature14539 (cit. on p. 51).

Li, L., L. G. Wang, F. L. Teixeira, C. Liu, A. Nehorai, and T. J. Cui (2019). “Deepnis: Deep Neural Network for Nonlinear Electromagnetic Inverse Scattering”. *IEEE Trans. Antennas Propagat.* 67.3, pp. 1819–1825. doi: 10.1109/TAP.2018.2885437 (cit. on p. 60).

Li, M., O. Semerci, and A. Abubakar (2013). “A Contrast Source Inversion Method in the Wavelet Domain”. *Inverse Prob.* 29, p. 025015. doi: 10.1088/0266-5611/29/2/025015 (cit. on p. 16).

Liang, M. and X. Hu (2015). “Recurrent Convolutional Neural Network for Object Recognition”. *2015 IEEE Conference on Computer Vision and Pattern Recognition (CVPR)*. Boston, MA, pp. 3367–3375. doi: 10.1109/CVPR.2015.7298958 (cit. on p. 51).

Litjens, G., T. Kooi, B. E. Bejnordi, A. A. A. Setio, F. Ciompi, M. Ghafoorian, J. A. van der Laak, B. van Ginneken, and C. I. Sánchez (2017). “A Survey on Deep Learning in Medical Image Analysis”. *Med. Image Anal.* 42, pp. 60–88. doi: 10.1016/j.media.2017.07.005 (cit. on p. 51).

Liu, J., H. Zhou, T. Ouyang, Q. Liu, and Y. Wang (2022). “Physical Model-inspired Deep Unrolling Network for Solving Nonlinear Inverse Scattering Problems”. *IEEE Trans. Antennas Propagat.* 70.2, pp. 1236–1249. doi: 10.1109/TAP.2021.3111281 (cit. on p. 61).

Liu, J. and P. Moulin (2001). “Information-theoretic Analysis of Interscale and Intrascale Dependencies between Image Wavelet Coefficients”. *IEEE Trans. Image Processing* 10.11, pp. 1647–1658. doi: 10.1109/83.967393 (cit. on p. 25).

Liu, J. and J. Ye (2010). “Moreau-Yosida Regularization for Grouped Tree Structure Learning”. *Advances in Neural Information Processing Systems*. Ed. by J. Lafferty, C. Williams, J. Shawe-Taylor, R. Zemel, and A. Culotta. Vol. 23. Curran Associates, Inc. (cit. on p. 34).

Liu, Z., M. Roy, D. K. Prasad, and K. Agarwal (2022). “Physics-guided Loss Functions Improve Deep Learning Performance in Inverse Scattering”. *IEEE Trans. Comput. Imaging* 8, pp. 236–245. doi: 10.1109/TCI.2022.3158865 (cit. on pp. xvii, 4, 61, 80, 82).

Lobel, P., L. Blanc-Féraud, C. Pichot, and M. Barlaud (1997). “A New Regularization Scheme for Inverse Scattering”. *Inverse Prob.* 13.2, pp. 403–410. doi: 10.1088/0266-5611/13/2/013 (cit. on p. 24).

Lucas, A., M. Iliadis, R. Molina, and A. K. Katsaggelos (2018). “Using Deep Neural Networks for Inverse Problems in Imaging: Beyond Analytical Methods”. *IEEE Signal Processing Mag.* 35.1, pp. 20–36. doi: 10.1109/MSP.2017.2760358 (cit. on pp. 3, 51).

Mallat, S. (2008). *A Wavelet Tour of Signal Processing, Third Edition: The Sparse Way*. 3rd. USA: Academic Press, Inc. (cit. on pp. xi, 5, 29).

Mardani, M., Q. Sun, S. Vasawanala, V. Papyan, H. Monajemi, J. Pauly, and D. Donoho (2018). “Neural Proximal Gradient Descent for Compressive Imaging”. *Proceedings of the 32nd International Conference on Neural Information Processing Systems*. NIPS’18. Montréal, Canada: Curran Associates Inc., pp. 9596–9606 (cit. on p. 59).

Massa, A., D. Marcantonio, X. Chen, M. Li, and M. Salucci (2019). “DNNs As Applied to Electromagnetics, Antennas, and Propagation—a Review”. *IEEE Antennas Wireless Propagat. Lett.* 18.11, pp. 2225–2229. doi: 10.1109/LAWP.2019.2916369 (cit. on p. 61).

Massa, A., P. Rocca, and G. Oliveri (2015). “Compressive Sensing in Electromagnetics - a Review”. *IEEE Antennas Propagat. Mag.* 57.1, pp. 224–238. doi: 10.1109/MAP.2015.2397092 (cit. on p. 25).

McCann, M. T., K. H. Jin, and M. Unser (2017). “Convolutional Neural Networks for Inverse Problems in Imaging: A Review”. *IEEE Signal Processing Mag.* 34.6, pp. 85–95. doi: 10.1109/MSP.2017.2739299 (cit. on p. 51).

Monga, V., Y. Li, and Y. C. Eldar (2021). “Algorithm Unrolling: Interpretable, Efficient Deep Learning for Signal and Image Processing”. *IEEE Signal Processing Mag.* 38.2, pp. 18–44. doi: 10.1109/MSP.2020.3016905 (cit. on p. 58).

Nason, G. P. and B. W. Silverman (1995). “The Stationary Wavelet Transform and Some Statistical Applications”. *Wavelets and Statistics*. Ed. by A. Antoniadis and G. Oppenheim. New York, NY: Springer New York, pp. 281–299. doi: 10.1007/978-1-4612-2544-7_17 (cit. on p. 25).

Nikolova, N. K. (2011). "Microwave Imaging for Breast Cancer". *IEEE Microwave* 12.7, pp. 78–94. doi: 10.1109/MMM.2011.942702 (cit. on pp. x, 1).

Oliveri, G., M. Salucci, N. Anselmi, and A. Massa (2017). "Compressive Sensing As Applied to Inverse Problems for Imaging: Theory, Applications, Current Trends, and Open Challenges." *IEEE Antennas Propagat. Mag.* 59.5, pp. 34–46. doi: 10.1109/MAP.2017.2731204 (cit. on p. 25).

Ongie, G., A. Jalal, C. A. Metzler, R. G. Baraniuk, A. G. Dimakis, and R. Willett (2020). "Deep Learning Techniques for Inverse Problems in Imaging". *IEEE Journal on Selected Areas in Information Theory* 1.1, pp. 39–56. doi: 10.1109/JSAIT.2020.2991563 (cit. on pp. 3, 58).

Pastorino, M. (2007). "Stochastic Optimization Methods Applied to Microwave Imaging: A Review". *IEEE Trans. Antennas Propagat.* 55.3, pp. 538–548. doi: 10.1109/TAP.2007.891568 (cit. on pp. 2, 4).

Pastorino, M. and A. Randazzo (2018). *Microwave Imaging Methods and Applications*. Artech House (cit. on pp. x, 1).

Paszke, A., S. Gross, F. Massa, A. Lerer, J. Bradbury, G. Chanan, T. Killeen, Z. Lin, N. Gimelshein, L. Antiga, A. Desmaison, A. Köpf, E. Z. Yang, Z. DeVito, M. Raison, A. Tejani, S. Chilamkurthy, B. Steiner, L. Fang, J. Bai, and S. Chintala (2019). "Pytorch: An Imperative Style, High-performance Deep Learning Library". *Advances in Neural Information Processing Systems 32: Annual Conference on Neural Information Processing Systems 2019, NeurIPS 2019, December 8-14, 2019, Vancouver, BC, Canada*. Ed. by H. M. Wallach, H. Larochelle, A. Beygelzimer, F. d'Alché-Buc, E. B. Fox, and R. Garnett, pp. 8024–8035 (cit. on p. 65).

Qin, Y. (Sep 2021). "Early Breast Anomalies Detection with Microwave and Ultrasound Modalities". PhD thesis. Université Paris-Saclay (cit. on pp. x, 1).

Qin, Y., T. Rodet, M. Lambert, and D. Lesselier (2021). "Joint Inversion of Electromagnetic and Acoustic Data with Edge-preserving Regularization for Breast Imaging". *IEEE Trans. Comput. Imaging* 7, pp. 349–360. doi: 10.1109/TCI.2021.3067158 (cit. on p. 24).

Qing, A., C. K. Lee, and L. Jen (2001). "Electromagnetic Inverse Scattering of Two-dimensional Perfectly Conducting Objects by Real-coded Genetic Algorithm". *IEEE Trans. Geosci. Remote Sensing* 39.3, pp. 665–676. doi: 10.1109/36.911123 (cit. on pp. 2, 4).

Ran, P., S. Chen, M. Serhir, and D. Lesselier (2021). "Imaging of Subwavelength Microstructures by Time Reversal and Neural Networks, from Synthetic to Laboratory-controlled Data". *IEEE Trans. Antennas Propagat.* 69.12, pp. 8753–8762. doi: 10.1109/TAP.2021.3083741 (cit. on p. 4).

Ran, P., Y. Qin, D. Lesselier, and M. Serhir (2021). "Subwavelength Microstructure Probing by Binary- Specialized Methods: Contrast Source and Convolutional Neural Networks". *IEEE Trans. Antennas Propagat.* 69.2, pp. 1030–1039. doi: 10.1109/TAP.2020.3016175 (cit. on pp. 4, 61).

Rao, N. S., R. D. Nowak, S. J. Wright, and N. G. Kingsbury (2011). "Convex Approaches to Model Wavelet Sparsity Patterns". *2011 18th IEEE International Conference on Image Processing*. Brussels, Belgium, pp. 1917–1920. doi: 10.1109/ICIP.2011.6115845 (cit. on p. 34).

Richmond, J. (1965). "Scattering by a dielectric cylinder of arbitrary cross section shape". *IEEE Trans. Antennas Propag.* 13.3, pp. 334–341. doi: 10.1109/TAP.1965.1138427 (cit. on p. 10).

Rockafellar, R. T. (1970). *Convex Analysis*. Princeton Mathematical Series. Princeton, N. J.: Princeton University Press (cit. on p. 33).

Romberg, J., H. Choi, and R. Baraniuk (2001). "Bayesian Tree-structured Image Modeling Using Wavelet-domain Hidden Markov Models". *IEEE Trans. Image Processing* 10.7, pp. 1056–1068. doi: 10.1109/83.931100 (cit. on p. 30).

Ronneberger, O., P. Fischer, and T. Brox (2015). "U-net: Convolutional Networks for Biomedical Image Segmentation". *Medical Image Computing and Computer-Assisted Intervention – MICCAI 2015*. Ed. by N. Navab,

J. Hornegger, W. M. Wells, and A. F. Frangi. Cham: Springer International Publishing, pp. 234–241 (cit. on pp. 60, 82).
Rudin, L. I., S. Osher, and E. Fatemi (1992). "Nonlinear Total Variation Based Noise Removal Algorithms". *Phys. D Nonlinear Phenom.* 60.1, pp. 259–268. doi: 10.1016/0167-2789(92)90242-F (cit. on p. 3).
Salucci, M., M. Arrebola, T. Shan, and M. Li (2022). "Artificial Intelligence: New Frontiers in Real Time Inverse Scattering and Electromagnetic Imaging". *IEEE Trans. Antennas Propagat.*, pp. 1–1. doi: 10.1109/TAP.2022.3177556 (cit. on p. 61).
Sanghvi, Y., H. Bisht, U. K. Khankhoje, V. M. Gadre, and S. V. Kulkarni (2020). "Iteratively Reweighted $\ell_1 - \ell_2$ Norm Minimization Using Wavelets in Inverse Scattering". *J. Opt. Soc. Am. A* 37.4, pp. 680–687. doi: 10.1364/JOSAA.381365 (cit. on p. 24).
Sanghvi, Y., Y. Kalepu, and U. K. Khankhoje (2020). "Embedding Deep Learning in Inverse Scattering Problems". *IEEE Trans. Comput. Imaging* 6, pp. 46–56. doi: 10.1109/TCI.2019.2915580 (cit. on pp. 4, 61).
Selesnick, I., R. Baraniuk, and N. Kingsbury (2005). "The Dual-tree Complex Wavelet Transform". *IEEE Signal Processing Mag.* 22.6, pp. 123–151. doi: 10.1109/MSP.2005.1550194 (cit. on pp. 25, 26).
Shor, N. Z. (1985). *Minimization Methods for Non-Differentiable Functions*. Springer Series in Computational Mathematics. Transl. from the Russian, Kiev, Naukova Dumka, 1979. Berlin: Springer. doi: 10.1007/978-3-642-82118-9 (cit. on p. 32).
Simon, N., J. Friedman, T. Hastie, and R. Tibshirani (2013). "A sparse-group lasso". *J. Comput. Graph. Stat.* 22.2, pp. 231–245 (cit. on p. 33).
Song, R., Y. Huang, K. Xu, X. Ye, C. Li, and X. Chen (2021). "Electromagnetic Inverse Scattering with Perceptual Generative Adversarial Networks". *IEEE Trans. Comput. Imaging* 7, pp. 689–699. doi: 10.1109/TCI.2021.3093793 (cit. on p. 4).
Taşkin, U. and Ö. Özdemir (2017). "Sparsity Regularized Nonlinear Inversion for Microwave Imaging". *IEEE Geosci. Remote. S.* 14.12, pp. 2220–2224. doi: 10.1109/LGRS.2017.2757087 (cit. on pp. 24, 38).
Tibshirani, R. (1996). "Regression Shrinkage and Selection Via the Lasso". *J. R. Stat. Soc., B: Stat. Methodol.* 58.1, pp. 267–288 (cit. on p. 3).
Tikhonov, A. N. (1963). "Solution of Incorrectly Formulated Problems and the Regularization Method". *Soviet Mathematics Doklady* 4, pp. 1035–1038 (cit. on p. 24).
Tikhonov, A. N., A. Goncharsky, V. Stepanov, and A. G. Yagola (1995). *Numerical Methods for the Solution of Ill-posed Problems*. Vol. 328. Springer Science & Business Media (cit. on p. 2).
Tomassi, D., D. Milone, and J. D. Nelson (2015). "Wavelet Shrinkage Using Adaptive Structured Sparsity Constraints". *Signal Process* 106, pp. 73–87. doi: 10.1016/j.sigpro.2014.07.001 (cit. on p. 25).
Tsang, L., J. A. Kong, and K.-H. Ding (2004). *Scattering of Electromagnetic Waves: Theories and Applications*. John Wiley & Sons (cit. on p. 6).
Tsang, L., J. A. Kong, and R. T. Shin (1985). *Theory of Microwave Remote Sensing*. Wiley (cit. on pp. x, 1).
Van den Berg, P. M. and A. Abubakar (2001). "Contrast Source Inversion Method: State of Art". *Prog. Electromagn. Res.* 34, pp. 189–218 (cit. on pp. 4, 12).
Van Leeuwen, J. (1991). *Handbook of Theoretical Computer Science (vol. A) Algorithms and Complexity*. Mit Press (cit. on p. 3).
Varotsos, C. and V. Krapivin (2020). *Microwave Remote Sensing Tools in Environmental Science*. Springer Cham, Switzerland. doi: 10.1007/978-3-030-45767-9 (cit. on pp. x, 1).
Wang, Z., A. C. Bovik, H. R. Sheikh, and E. P. Simoncelli (2004). "Image quality assessment: from error visibility to structural similarity". *IEEE Trans. Image Process.* 13.4, pp. 600–612 (cit. on p. 65).

Wei, Z. and X. Chen (2019a). “Deep-learning Schemes for Full-wave Nonlinear Inverse Scattering Problems”. *IEEE Trans. Geosci. Remote Sensing* 57.4, pp. 1849–1860. doi: 10.1109/TGRS.2018.2869221 (cit. on pp. 4, 20, 61, 65, 82).

Wei, Z. and X. Chen (2019b). “Physics-inspired Convolutional Neural Network for Solving Full-wave Inverse Scattering Problems”. *IEEE Trans. Antennas Propagat.* 67.9, pp. 6138–6148. doi: 10.1109/TAP.2019.2922779 (cit. on pp. 4, 61).

Winters, D. W., B. D. Van Veen, and S. C. Hagness (2010). “A Sparsity Regularization Approach to the Electromagnetic Inverse Scattering Problem”. *IEEE Trans. Antennas Propagat.* 58.1, pp. 145–154. doi: 10.1109/TAP.2009.2035997 (cit. on p. 24).

Ye, X., Y. Bai, R. Song, K. Xu, and J. An (2020). “An Inhomogeneous Background Imaging Method Based on Generative Adversarial Network”. *IEEE Trans. Microwave Theory Tech.* 68.11, pp. 4684–4693. doi: 10.1109/TMTT.2020.3015495 (cit. on p. 4).

Yuan, M. and Y. Lin (2006). “Model Selection and Estimation in Regression with Grouped Variables”. *J. R. Stat. Soc. B* 68.1, pp. 49–67 (cit. on p. 32).

Zaimaga, H., A. Fraysse, and M. Lambert (2017). “Sparse Reconstruction Algorithms for Nonlinear Microwave Imaging”. *2017 25th European Signal Processing Conference (EUSIPCO)*. Kos, Greece, pp. 713–717. doi: 10.23919/EUSIPCO.2017.8081300 (cit. on p. 25).

Zaimaga, H. and M. Lambert (2016). “Sparsity-enforced Microwave Inverse Scattering Using Soft Shrinkage Thresholding”. *2016 24th European Signal Processing Conference (EUSIPCO)*. Budapest, Hungary, pp. 350–354. doi: 10.1109/EUSIPCO.2016.7760268 (cit. on p. 24).

Zhang, J. and B. Ghanem (2018). “ISTA-net: Interpretable Optimization-inspired Deep Network for Image Compressive Sensing”. *2018 IEEE/CVF Conference on Computer Vision and Pattern Recognition*. Salt Lake City, UT, USA, pp. 1828–1837. doi: 10.1109/CVPR.2018.00196 (cit. on p. 59).

Zhang, K., W. Zuo, S. Gu, and L. Zhang (2017). “Learning Deep CNN Denoiser Prior for Image Restoration”. *2017 IEEE Conference on Computer Vision and Pattern Recognition (CVPR)*. Honolulu, HI, USA, pp. 2808–2817. doi: 10.1109/CVPR.2017.300 (cit. on pp. 3, 51).

Zhang, S. and E. Salari (2005). “Image Denoising Using a Neural Network Based Non-linear Filter in Wavelet Domain”. *Proceedings. (ICASSP ’05). IEEE International Conference on Acoustics, Speech, and Signal Processing, 2005.* Vol. 2. Philadelphia, PA, USA, ii/989–ii/992 Vol. 2. doi: 10.1109/ICASSP.2005.1415573 (cit. on pp. 3, 51).

Zhang, Y., A. Fraysse, M. Lambert, and D. Lesselier (2021a). “A Wavelet-based Contrast Source Inversion Method”. *IEEE 19th International Symposium on Antenna Technology and Applied Electromagnetics (ANTEM)*. Winnipeg, Canada, pp. 1–2. doi: 10.1109/ANTEM51107.2021.9518522 (cit. on p. 83).

Zhang, Y., A. Fraysse, M. Lambert, and D. Lesselier (2021b). “Use of Sparsity in Nonlinear Electromagnetic Imaging”. *XXXIV General Assembly and Scientific Symposium (GASS) of the International Union of Radio Science*. Rome, Italie (cit. on p. 83).

Zhang, Y., M. Lambert, A. Fraysse, and D. Lesselier (2021). “Group Sparsity Penalized Contrast Source Solution Method for 2-D Non-linear Inverse Scattering”. *IEEE Open J. Antennas Propag.* 3, pp. 48–58. doi: 10.1109/OJAP.2021.3133450 (cit. on p. 83).

Zhang, Y., M. Lambert, A. Fraysse, and D. Lesselier (2022). “Unrolled Convolutional Neural Network for Full-Wave Inverse Scattering”. *IEEE Trans. Antennas Propag.(Early Access)*, pp. 1–9. doi: 10.1109/TAP.2022.3216999 (cit. on p. 83).

Zou, H. and T. Hastie (2005). “Regularization and Variable Selection Via the Elastic Net”. *J Roy Stat Soc B* 67.2, pp. 301–320 (cit. on p. 24).

Zoughi, R. (2000). *Microwave Non-destructive Testing and Evaluation*. Springer, Dordrecht (cit. on pp. x, 1).

université PARIS-SACLAY

ÉCOLE DOCTORALE
Physique et ingénierie : Electrons, Photons, Sciences du vivant (EOBE)

Titre : Imagerie électromagnétique non linéaire : d'algorithmes basés sur les ondelettes préservant la parcimonie à l'apprentissage en profondeur
Mots clés : inversion de source de contraste, transformée d'ondelettes complexes à double arborescence, parcimonie de groupe, apprentissage profond, méthode déroulée

Résumé : Ce travail traite de l'imagerie électromagnétique mal-posée non-linéaire à partir de données en régime harmonique dans une expérience de diffraction bidimensionnelle, en mettant l'accent sur deux approches dans le cadre de l'inversion de source de contraste (CSI). La première approche est un CSI pénalisé par la parcimonie de groupe dans le domaine des ondelettes, la seconde est un schéma d'apprentissage profond dit déroulé. Dans la première approche, une dépendance existe entre les coefficients d'ondelettes à différentes échelles, appelée relation parent-enfant, ce qui donne une structure d'arbre quaternaire d'ondelettes, de sorte que les coefficients d'ondelettes sont parcimonieux tant au niveau des pixels qu'au niveau des groupes. L'accent est mis sur l'utilisation de la transformée en ondelettes complexe (CWT) à double arborescence en vue d'obtenir correctement la représentation parcimonieuse par groupe recherchée. Une norme l2,1 ajoutée à la fonction coût standard applique la parcimonie de groupe aux coefficients d'ondelettes du contraste. La stratégie de réplication est combinée avec la méthode proximale afin de résoudre le problème pénalisé de groupes qui se chevauchent. La seconde approche est inspirée de la méthode déroulée. En intégrant les itérations CSI dans le modèle d'apprentissage profond, la connaissance du domaine est intégrée au processus d'apprentissage. Dans les deux cas, des tests numériques approfondis sont effectués afin d'évaluer les performances, la stabilité, la robustesse et la fiabilité, en menant des comparaisons avec des solutions considérées plus standard (comme CSI, la transformée en ondelettes discrète ou DWT, et U-net), et celles-ci illustrent l'avantage des deux approches proposées en de nombreux aspects.

Title: Non-linear electromagnetic imaging: from sparsity-preserving wavelet-based algorithms to deep learning
Keywords: contrast source inversion, dual-tree complex wavelet transform, group sparsity, deep learning, unrolled method

Abstract: This work deals with nonlinear ill-posed electromagnetic imaging from time-harmonic data within a two-dimensional scattering experiment, the focus being on two approaches in the framework of the contrast-source inversion (CSI). The first approach is a group sparsity penalized CSI in the wavelet domain, the second is an unrolled deep learning scheme. In the first approach, dependency exists between wavelet coefficients at different scales, referred to as parent-child relationship, which yields a wavelet quadtree structure so that wavelet coefficients are both pixel-wise and group-wise sparse. Emphasis is on the dual-tree complex wavelet transform (CWT) to achieve this result. A ‘2;1 norm added to the standard cost function is to enforce group sparsity onto the wavelet coefficients of the spatially-varying contrast. The replication strategy is combined with the proximal method to solve the overlapping group penalized problem. The second approach is inspired by the unrolled method. By embedding the CSI iterations into the deep learning model, the domain knowledge is incorporated into the learning process. In both cases, thorough numerical tests are carried out to evaluate performance, stability, robustness, and reliability with comparisons with more standard solutions (like CSI, discrete wavelet transform (DWT) and U-net), which exhibit the advantage of the proposed approaches under many aspects.